

3 The Sun as a Star

Giulio Del Zanna · Helen Mason

DAMTP, Centre for Mathematical Sciences, University of
Cambridge, Cambridge, UK

1	<i>Introduction</i>	90
2	<i>Historic Perspective</i>	93
3	<i>Observing the Solar Atmosphere from Space</i>	98
3.1	Early Space Missions	98
3.2	Yohkoh	101
3.3	Ulysses	102
3.4	The Solar and Heliospheric Observatory – SoHO	103
3.5	Transition Region and Coronal Explorer (TRACE)	108
3.6	Ramaty High-Energy Solar Spectroscopic Imager (RHESSI)	108
3.7	CORONAS Missions	108
3.8	Hinode	110
3.9	STEREO	113
3.10	Solar Dynamics Observatory (SDO)	114
3.11	Imaging Versus Spectroscopic Instruments	115
4	<i>The Lower Solar Atmosphere</i>	115
4.1	The Photosphere and the Sun’s Magnetic Field	115
4.2	The Chromosphere	118
4.3	The Transition Region	122
5	<i>The Interior of the Sun</i>	125
5.1	The Standard Model and the Solar Neutrinos	125
5.2	Solar Oscillations	126
5.3	Some Results from Helioseismology Inversions	130
5.4	Abundances and Helioseismic Models	133
5.5	Local Helioseismology	134
5.6	The Solar Dynamo	135
6	<i>Radiation from the Solar Corona: Atomic Processes and Plasma Diagnostics</i> ...	135
6.1	Line Flux and Intensity	137
6.2	Differential Emission Measure and Emission Measure	138
6.3	Atomic Processes Affecting the Ion Excitation	138
6.4	Atomic Processes Affecting the Ion State	140
6.5	Coronal Model Approximation: Two-Level Ion	141
6.6	Emission Measure Approximations	142

6.7	A Word of Warning: Problems with Emission Measures	145
6.8	Electron Density Determination	145
6.9	Spectroscopic Filling Factors	147
6.10	Electron Temperature Determination	148
6.11	Continuum	149
6.12	Line Widths, Ion Temperatures, and Doppler Motions	150
6.13	The CHIANTI Atomic Package	150
6.14	Benchmarking the Atomic Data	152
7	<i>Chemical Abundances</i>	152
7.1	Photospheric Abundances	153
7.2	Coronal Abundances	153
7.3	Abundances from In Situ Measurements	155
7.4	Depletion, Enhancement or Both?	155
7.5	Helium, Neon, and Argon	156
7.6	Modeling	158
7.7	Stellar and Galactic Abundances	158
8	<i>The Solar Corona</i>	159
8.1	Solar Features as Seen in X-rays and EUV	159
8.2	Solar Active Regions	160
8.2.1	Active Regions Observed with SoHO CDS	161
8.2.2	Active Regions Observed with Hinode EIS	162
8.3	Coronal Heating	162
8.3.1	Coronal Heating in Loops	165
8.3.2	Hydrostatic Models and the RTV Scaling Laws	165
8.3.3	Hydrodynamic Models of Active Region Loops	166
8.3.4	Microflares and Nanoflares	169
9	<i>Solar Flares and Coronal Mass Ejections</i>	170
9.1	Solar Flares	170
9.2	Coronal Mass Ejections (CMEs)	174
9.3	Theoretical Concepts of CME Initiation	176
9.4	Flares on Other Stars	178
10	<i>Solar Wind</i>	182
10.1	The Heliosphere	185
10.2	Physical Characteristics of the Solar Wind and Models	185
10.3	The Sources of the Solar Wind	187
10.4	Ulysses	188
11	<i>Solar Irradiance</i>	189
11.1	Introduction	189
11.2	Total Solar Irradiance, TSI, and Surface Temperature	190
11.3	Irradiance in the UV	195
11.3.1	Irradiance in the EUV and X-rays	196

12	<i>Future Prospects</i>	199
12.1	Solar Orbiter	200
12.2	Solar Probe+	200
	<i>References</i>	201

Abstract: In this chapter we provide an overview of various observational and theoretical aspects about the Sun, paying more attention to global ones, i.e., to those where the Sun is considered as a star, so they can be more or less directly related to those studied for other stars. The emphasis is on the processes by which energy is transferred to the solar atmosphere and then flows from the Sun in the form of radiation and particles. The chapter starts with an historical introduction, and then discusses various subjects, starting with a brief description of the photosphere, the chromosphere, and the transition region of the Sun. The interior of the Sun is then introduced, with the standard model and solar neutrinos, and with the observations and theory of solar oscillations. We present some important results from helioseismology, and briefly discuss the problematics involved with the production and regeneration of the solar magnetic fields during a solar cycle.


We then discuss the atomic processes which lead to the formation of the optically thin radiation that is emitted from the X-rays to the UV from the solar corona. In particular, the spectroscopic diagnostic techniques which are used to determine the physical parameters of a stellar corona are discussed in some depth.

We describe some of the in situ and remote-sensing measurements and modeling that have been used to obtain the solar chemical abundances, and how they compare with stellar and galactic abundances. We then introduce the main features of the solar corona, together with observations and modeling of flares and coronal mass ejections. We conclude by describing two subjects of relevance for the entire solar system and in particular for our planet, the solar wind and the solar irradiance.

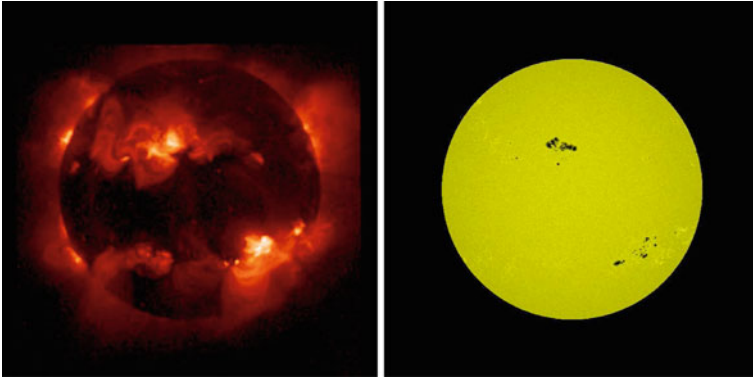
For each subject, we provide a brief historical overview, and then refer the reader to standard textbooks and recent literature. Our knowledge of the Sun as a star has progressed significantly over the last century, however a clear understanding of the physical processes at work in the interior of the Sun, in its atmosphere, and in the solar wind is still incomplete, and further challenges lie ahead. We should be able to understand our Sun, before we can attempt a complete description of other stars and astrophysical objects.

Keywords: Atomic processes; Helioseismology; Solar corona; Sun

1 Introduction

The Sun is a typical middle-aged, low-mass star, but it is the only star which can be studied in great detail, due to its proximity. Viewed in white light, and at low resolution, the Sun might appear as a featureless disk, except for the occasional presence of a few sunspots. However, when viewed at ultraviolet (UV) or X-ray wavelengths, the hot corona provides a spectacular display, as shown in  Fig. 3-1.

With the advent of space-borne instrumentation over the past few decades, some fantastic images and movies have been obtained, together with new insights into the nature of the solar atmosphere. Extreme ultraviolet (EUV) and X-ray observations of the solar atmosphere from the most recent solar missions, such as the Yohkoh, SoHO, TRACE, Stereo, Hinode and SDO satellites, have revealed complex and dynamic structures, which are clearly governed by the Sun's magnetic field. The energy channeled by and stored in solar magnetic fields is released in the solar atmosphere in the form of thermal and kinetic energy, both on small and large scales.



■ Fig. 3-1

The Sun in X-rays (*lhs*) and white light (*rhs*) (Courtesy: *Yohkoh*)

This energy release can be observed in a number of interesting and dramatic phenomena, ranging from small brightenings and jets to huge solar flares and coronal mass ejections (CMEs), seen as intense emission in a broad wavelength range: from X-rays down to radio frequencies.

Stimulated by these recent observations, research in solar physics, both observational and theoretical, has progressed at a rapid pace. Major progress has been made in recent years on some fundamental issues: the main dynamo responsible for the magnetic field and sunspots is believed to be based in the tachocline (the thin layer just below the convective zone); magnetic fields emerge through the photosphere over a wide range of scales and create many small regions of opposite polarity magnetic flux in the quiet Sun (forming what is termed *the magnetic carpet*); the corona has a highly complex topology and may well be heated by the coronal tectonics mechanism; magnetic flux emergence into the solar atmosphere can trigger large-scale explosive events (solar flares and coronal mass ejections); the solar wind can be highly variable, with an as yet unknown acceleration mechanism. Significant advances have been made in theory and modeling but further work is needed. For example, it is only in the last few years that the process of magnetic reconnection (by which magnetic field lines change connectivity and energy can be released) has been studied in 3D. It turns out that 3D reconnection is completely different from 2D reconnection. New insights have been provided concerning the impact of the Sun on the heliosphere and near-Earth environment, using in situ measurements from SoHO, Cluster and Ulysses.

The Sun is a yellow dwarf star with a mass of 2×10^{30} kg, a diameter of 1,392,000 km (just over 109 times the diameter of the Earth) and is 149.6 million km from the Earth (termed an Astronomical Unit, 1 AU). The Sun is 4.5 billion years old, almost half way through its life cycle. It will eventually grow into a red giant. The color of a star is determined by the surface temperature, most stars being between 3,000 K (red) and 40,000 K (blue). The Sun appears yellow because it has a surface temperature of around 6,000 K, but the temperature of the core is 15 million K. The nearest star to the Sun, Proxima Centauri, is 4 light-years away (63,240 AU). Sirius, often called *the Dog star*, is the brightest star in the sky. It is a blue star with a surface temperature of 10,000 K and is 9 light-years away. It has a very faint and dense companion, a white dwarf known as Sirius B, which has the mass of the Sun, but is only the size of the Earth. The first spatially resolved image which astronomers were able to obtain of another star was

of Betelgeuse, which is a red supergiant in the far-off constellation of Orion. Its mass is about ten times that of the Sun, but it is 50,000 times brighter than the Sun. If it were in the same position as the Sun, it would extend almost out to the orbit of Jupiter. When the Sun is about 7 billion years old it will slowly start to change and will become bigger and cooler. By the time it is 10 billion years old it will have changed into a red giant and its atmosphere will stretch out to near where the Earth is today. The Sun is just one star in a spiral galaxy, the Milky Way, which is 75,000 light years across and contains 100 billion stars.

The Sun provides a unique physical laboratory with extreme conditions. The level of detail which we can now observe is almost overwhelming, from the visible to the X-rays. It is indeed a challenge to understand and model the underlying physical processes. Studies of the Sun have helped to deepen our understanding of processes in other stars. Interdisciplinary research in the *solar-stellar connection* reveals insights into properties as diverse as astrophysical dynamo action, starspots, flares, prominences, and variations in elemental abundances. Stellar coronae seem to be a general phenomena rather than an exceptional occurrence. It has become clear that all late-type stars share the same basic coronal characteristics: the presence of thermal plasma at several million degrees, magnetic confinement, the presence of flares, etc. The basic plasma physics governing coronae is also probably very similar in all of these stars. Otherwise similar stars may have very different levels of stellar activity, UV and X-ray luminosity, and starspots. This is believed to be due to very different rotation speeds which probably determine how effectively the stellar magnetic dynamo generates magnetic fields. One might then expect that differences between the coronae of late-type stars are just due to rather different regimes of the dynamo at work inside the stars, while the basic plasma phenomena occurring in the outer magnetized coronal plasma are probably very similar. EUV and X-ray spectroscopic observations, such as those from EUVE, FUSE, XMM, and Chandra have progressed our knowledge of stellar atmospheres enormously.

Listed below are some of the key questions confronting us in solar research in the modern era, which also relate to other stars and their stellar systems.

- How are magnetic fields generated and transported in the interior of the Sun?
- What causes the solar activity cycle?
- How is the solar corona heated?
- What is the source of and acceleration mechanism for the coronal mass ejections and the solar wind?
- How does the Sun interact with the Earth's environment?
- What is the relationship between solar radiation and the Earth's climate?

In this chapter it is impossible to cover or do justice to the whole spectrum of solar research. We have therefore chosen to focus primarily on what has been learnt from recent observations of the Sun and measurements of the solar wind. We relate these studies to theoretical models where possible, but have left out much of the detailed theoretical work, for example MHD, dynamo, convection and helioseismology models, which could in themselves comprise a whole book, or indeed several volumes! Instead, we refer the reader to standard texts in these subjects. In this chapter we present a historical perspective and the latest solar observations, techniques, interpretation of these observations linked to theoretical models, concepts and possibilities for future directions in solar research, in the context of the Sun as a star. The emphasis is on the processes by which energy is transferred to the solar atmosphere and then flows from the Sun in the form of radiation and particles. In particular, the spectroscopic diagnostic techniques which

are used to determine the physical parameters of the solar atmosphere are discussed in depth. They provide a powerful tool for probing the nature of the solar atmosphere. Similar techniques are now also being applied to the study of other stars and astrophysical objects.

Several excellent books on the Sun have been written in recent years which feature the latest solar observations and theories (Aschwanden 2006; Foukal 2004; Golub and Pasachoff 2010; Phillips 1992; Phillips et al. 2008; Priest and Forbes 2000; Thomas and Weiss 2008). Earlier books, such as Athay (1976), Jordan (1981), Priest (1982), Zirin (1988), Mariska (1992), and Stix (2002) are timeless. These are highly recommended for further study.

2 Historic Perspective

Chinese astronomers reported seeing sunspots several thousand years ago. They did not have telescopes, but when looking through fog or the smoke from forest fires, they noticed that the Sun had very small, dark dots on it. However, it was not until the invention of the telescope that it was possible to study sunspots in detail. The first telescopic observations of sunspots were made by Galileo and Harriot in 1610. However, Harriot never published his observations of sunspots so his work was not known about until after his death. Galileo noted that sunspots appeared, disappeared, and changed their shapes so he deduced that they could not possibly be planets just passing in front of the Sun. He also noted that the sunspots moved (the Sun's rotation is around 25 days in the equatorial region, but slower toward the polar regions). Galileo was not the first to use a telescope, but he was one of the first to carry out extensive observations of the skies (day and nighttime) with his telescope.

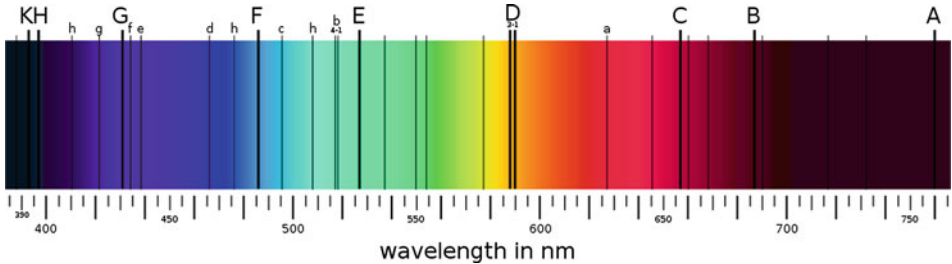
In 1843, Samuel Schwabe discovered a periodic variation in the average number of sunspots seen on the disk of the Sun from year to year. By studying these and other observations, Rudolf Wolf was able to reconstruct the solar cycle back to 1745, eventually pushing these reconstructions back to the earliest observations of sunspots by Galileo and his contemporaries. Cycles as short as 9 years and as long as 14 years have been observed, but the average is 11 years. During the solar minimum, the Sun can go for long periods without any sunspots. During solar maximum, the Sun is very active, with many active regions (and corresponding sunspots) producing solar flares and coronal mass ejections (CMEs). The solar activity cycle can have consequences for the Earth's environment, space weather, and the climate. For example, the period between 1645 and 1715, a time during which very few sunspots were observed coincides with the Little Ice Age. This epoch is now known as the Maunder minimum. However, it should be stressed that recent (during the last three decades) global warming cannot be attributed to changes in the solar cycle.

Sir Isaac Newton was fascinated by the nature of light. It was known that when white light shone through a prism, the colors of the rainbow were produced. However, it was thought that the nature of light was changed within the prism. Newton took another prism and isolated one color. This remained unchanged when passing back through the second prism. His work was published by the Royal Society *Opticks: or a Treatise of the Reflexions, Refractions, Inflexions and Colors of Light*. His interests lay in many fields of science and mathematics, including astronomy, and he built the first reflecting telescope, which used mirrors instead of lenses. Hence he removed the aberrations of colors which were problematic with refracting telescopes. Wollaston in 1802 commented on the *gaps* in the visible spectrum. Thereafter spectroscopic techniques

developed rapidly. In 1811, Fraunhofer produced a spectrum of the Sun, using a spectrograph with a slit, showing an array of dark absorption lines (see [▶ Fig. 3-2](#)). The Fraunhofer spectrum is formed by the continuous spectrum of the photosphere, with a characteristic temperature of 6,000 K, superimposed by absorption lines.

The second half of the nineteenth century saw rapid advances in observations of the solar corona during eclipses. Pietro Angelo Secchi SJ (1818–1878) was an Italian astronomer who made fundamental contributions to astrophysics and solar physics. His photographs of the solar corona taken during the eclipse of 1860 in Spain, together with those of Warren de la Rue, provided the first proof that prominences are real effects of the solar atmosphere. [▶ Figure 3-3](#) shows the corona in visible light during a total solar eclipse. Because the corona is a million times fainter than the solar disk, we can observe it from the Earth only during a total solar eclipse, or by using a coronagraph which simulates an eclipse by occulting the bright solar disk. The most striking physical property of the corona is its extent, with streamers stretching out for great distances.

We now know that the emission from the solar corona is diverse. The dominant contributions are the so-called K- (Kontinuierlich), F- (Fraunhofer), and E- (Emission) corona. The F-corona is photospheric light reflected by dust particles which are present close to the Sun. The reflection largely keeps the photospheric emission unmodified. The K-corona is photospheric light scattered by coronal electrons. The scattering polarizes the light and broadens the Fraunhofer lines so much that they become undetectable.



■ Fig. 3-2

The Fraunhofer spectrum

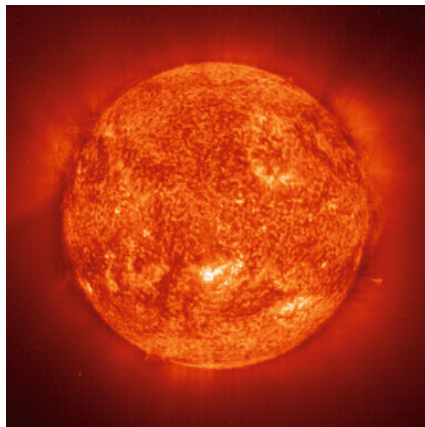


■ Fig. 3-3

White light image of the solar corona during a total solar eclipse (Courtesy of A. Sterling)

Spectroscopy techniques were used to analyze the solar atmosphere during eclipses. Janssen was the first to apply slit spectroscopy during the 1868 eclipse in India, and to observe the chromosphere and solar prominences in emission in the red $H\alpha$ (line C in the Fraunhofer spectrum) line. At the 1868 eclipse, as the photosphere was covered, Young attempted to observe the *flash spectrum* of the chromosphere. He eventually succeeded in observing it at the 1870 eclipse in Spain. Young (1870) realized that these emission lines corresponded to the dark absorption lines seen in the spectrum from the solar disk. The dark Fraunhofer lines in the photospheric spectrum are in fact due to absorption by chromospheric material. Lockyer was the person who actually coined the name chromosphere (color-sphere). Both Janssen and Lockyer discovered a bright yellow line due to an unknown element. This line was close to the sodium doublet (named D_1, D_2), so the new line was named D_3 . Because it was found only on the Sun, the element was named *helium* by Lockyer after the Greek name *Helios* for the Sun. Only later, in 1895, was helium identified on Earth. We now know that helium is the most abundant element after hydrogen, and that helium also produces the strongest emission lines in the extreme-ultraviolet. An image of the Sun in helium emission is shown in [▶ Fig. 3-4](#).

The 1868 eclipse was also particularly important because the first of the coronal lines, the green one (5303 \AA), was observed by Rayet observing in Siam (now Thailand). The following year, in 1869, at the US eclipse, Harkness and Young also observed the green coronal emission line, although they incorrectly identified it with a nearby chromospheric line (5317 \AA). It was only during the 1898 eclipse that these two lines were separated by Lockyer. The observation of the green coronal emission line provided a weight of evidence that the corona (as seen during an eclipse) was a characteristic of the Sun rather than the Moon. However, the coronal *green line* and other coronal visible emission lines provided astronomers with a major puzzle. This presented the single most outstanding problem in astrophysics for 50 years. The wavelength of the green line, 1474 (on Kirchhoff's scale, 5303 \AA) did not match the emission spectrum from any known element. This presented a serious challenge to the new science of spectroscopy. In addition, the corona extended much further (by a factor of 100) from the solar disk than seemed



■ Fig. 3-4

The Sun in the helium $\text{Ly}\alpha$ emission (304 \AA) as observed on August 11, 1999, from SoHO EIT (Courtesy of the SoHO consortium)

possible. The name *coronium* was assigned to the unknown element responsible for the coronal green line. Lyot (1939) used his coronagraph to study the coronal spectrum and found that the green line was very wide (0.9 Å). A major advance came in 1939 through the meticulous laboratory work of Edlen, who following a suggestion by Grotrian, assigned the strange coronal lines to highly ionized stages of iron, calcium and nickel (Edlén 1942). The green line is due to the forbidden transition in the ground configuration of Fe XIV (Fe^{+13}), that is iron with 13 electrons stripped from its outer shells. The *red line* is due to Fe X and the *yellow line* to Ca XV. The identifications of these coronal lines became one of the great triumphs in astrophysics. Temperatures in excess of 1 MK are needed to produce these ion stages, which also explained the large extent of coronal emission.

How energy was produced in stars posed another major puzzle for astronomers. In the nineteenth century, Lord Kelvin thought that the Sun might be powered by gravity. He suggested that if the Sun were collapsing and gradually getting smaller, the gravitational potential energy might be transferred into the heat and light the Sun emits. From the size and mass of the Sun, Kelvin calculated that the Sun could not be more than 25 million years old. The problem with Kelvin's theory was that scientists had already shown that the Earth was at least 400 million years old (we now know it to be a lot older than that). It hardly seemed likely that the Earth could be a lot older than the Sun. Bethe finally solved the mystery of the Sun's energy in the 1930s, but he based his ideas on the work Einstein had done many years before, when he proposed his famous formula $E = mc^2$, where E is energy, m is mass, and c is the speed of light. Bethe suggested that if the Sun could change just a small amount of its mass into energy, there would be enough energy to power the Sun for billions of years. He suggested that a way of doing this was to convert hydrogen to helium. Bethe won a Nobel Prize in 1954 for his *discovery concerning the energy production in stars*. Actually, Bethe's work was also based on pioneering work by a famous English astronomer, Eddington who said in 1926 "It is not too much to hope that in the not too distant future we shall be able to understand so simple a thing as a star".

At its core, the Sun is dense and hot enough (15 MK) to allow thermonuclear reactions to occur and to convert hydrogen into helium. The energy generated at the core is transferred by radiation out to about 0.7 of the solar radius. From this point, the energy is transported to the photosphere through convection. Through the combined actions of convection and differential rotation, the Sun operates as an alpha-omega dynamo where the magnetic field is constantly generated and sustained. The global solar magnetic field, driven by the regenerative dynamo, oscillates between the poloidal and toroidal components every 11 years, creating what is known as the solar cycle. The solar tachocline, at the bottom of the convection zone, is now known to play a key role in the dynamo process (Hughes et al. 2007).

The structure of the solar atmosphere can be crudely divided into different layers of gas and plasma threaded by magnetic fields. When viewed in white light the Sun appears to have a sharp edge, suggesting the existence of a solar surface. However, the Sun is a gas (plasma) and this apparent surface arises because the opacity of the solar plasma rises rapidly with temperature. The thin layer over which this rapid change from transparent to opaque takes place is termed the photosphere and has a characteristic temperature of 6,000 K. In fact, the base of the photosphere depends on the wavelength of the radiation. A common but somewhat arbitrary definition is where the optical depth is unity for radiation of wavelength 5,000 Å (Phillips et al. 2008).

Lying above the photosphere, the chromosphere has a typical thickness of 2,000 km and temperatures up to around 20,000 K (see [Fig. 3-5](#)). The photosphere and lower chromosphere are largely made up of neutral H atoms. In the upper chromosphere, the H atoms begin to be ionized, and large numbers of free protons and electrons may be found together with the

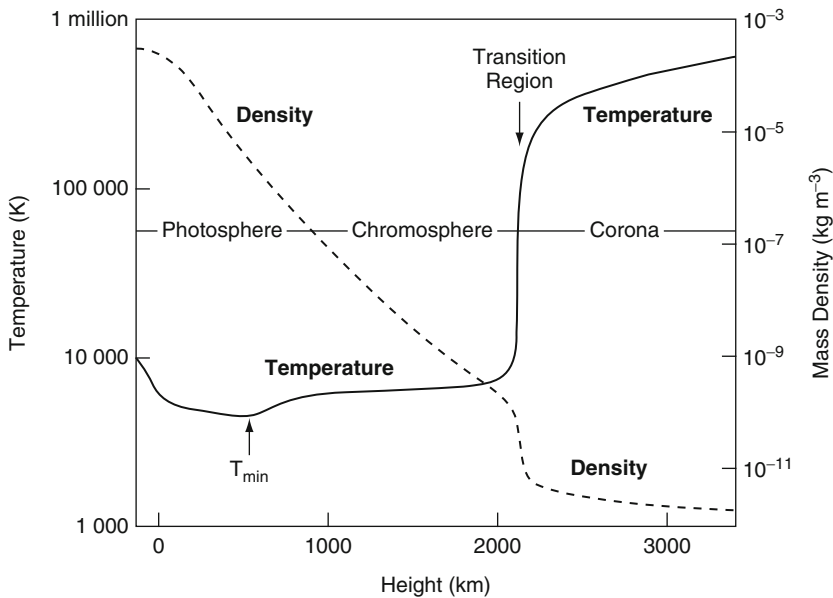
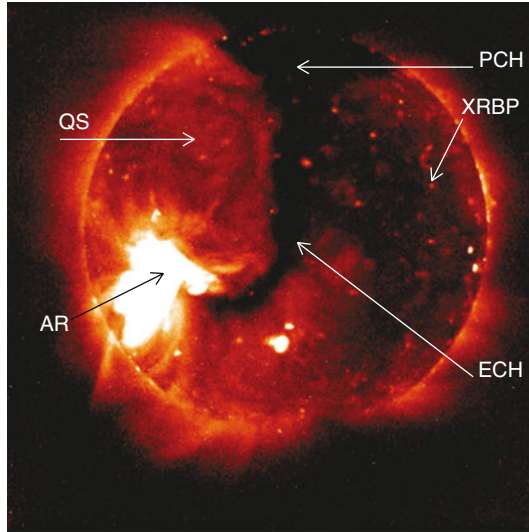


Fig. 3-5
Layers of the solar atmosphere

neutral H and He atoms. The transition region (TR) is a very thin region above the chromosphere, in which the temperature drastically increases to about 1 MK. The corona is the very hot, extended outer layer of the solar atmosphere. At these high temperatures, the coronal plasma emits radiation strongly in the EUV and X-rays. The unexpected and extraordinarily high temperature of the corona has been one of the main focuses for solar research over the past seven decades. The heating mechanism for the solar corona remains a hotly debated topic. A great deal of progress has been made in this regard, but a full explanation still eludes us.

The resolution of the coronal heating problem is likely to involve a mechanism by which magnetic energy can be dissipated as heat, such as reconnection. The appearance of the solar corona reflects the geometry and strength of the magnetic fields that are produced and emerge continuously from below the photosphere. A magnetic field of strength B exerts a pressure $B^2/8\pi$ on the plasma, which adds to the gas pressure P . The ratio of the gas pressure P to the magnetic pressure is known as the plasma β . While in the photosphere the pressure of the thermal gas dictates the behavior of the magnetic field lines, the opposite is true in the solar corona. Due to the low density, the gas pressure is significantly smaller, so that $\beta \ll 1$, i.e., the magnetic field dominates the dynamics of the tenuous coronal plasma.

As seen in X-ray emission (► Fig. 3-6) the corona is made up of three main structures: active regions (ARs), displaying intense X-ray emission; quiet regions, or the quiet Sun (QS), displaying faint, diffuse emission; and coronal holes (CHs) from which practically no coronal emission is detected. CHs are regions where the magnetic field is principally of one polarity. They are often found at the solar poles, but can also appear in other regions. The QS has a mixed-polarity magnetic field and is peppered with small bright points. A characteristic of ARs is the presence of hot loop arches (typically 1–4 MK) mirroring the magnetic field configuration and



■ Fig. 3-6

Image of the solar corona recorded by Yohkoh's Soft X-ray Telescope (SXT) on August 27, 1996, when the "Elephant's Trunk" equatorial coronal hole (Del Zanna and Bromage 1999) passed the meridian. QS quiet Sun regions, AR active region, ECH equatorial coronal hole, PCH polar coronal hole, XRBP X-ray bright point

extending up to 10^5 km from the photosphere, joining regions with opposite magnetic field polarity. One example is shown in [Fig. 3-7](#). Sunspots, dark regions of intense magnetic field, are frequently observed (in white light) in mature ARs (see [Fig. 3-8](#)). The most tantalizing aspects of the atmospheric activity such as solar flares, erupting filaments, and coronal mass ejections (CMEs) are often associated with ARs which have a strong magnetic field concentration. These highly energetic manifestations of the solar activity play an important role in understanding, and ultimately predicting, space weather.

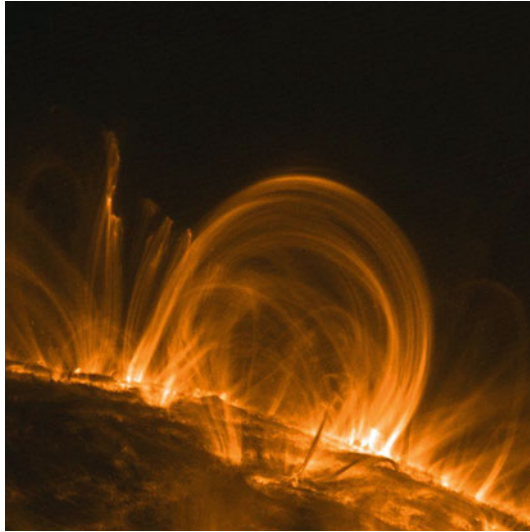
3 Observing the Solar Atmosphere from Space

The solar corona emits radiation over a very broad range of wavelengths, but because it is so hot, the UV and X-ray emission is very strong. Observing the Sun in spectral regions outside the visible, infrared, and radio wavelength ranges is only possible above the Earth's atmosphere.

3.1 Early Space Missions

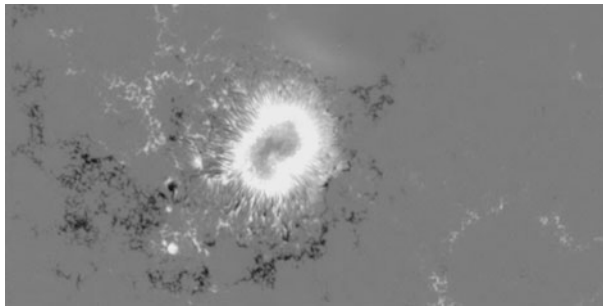
The 1970s saw a rapid development in techniques for high spatial resolution imaging of the X-ray corona. A number of rockets observing the corona with spectrometers in the X-rays and EUV were launched.

In May 1973, the first NASA space station, Skylab (see [Fig. 3-9](#)), was launched. The Apollo Telescope Mount (ATM) on Skylab carried several state-of-the-art solar instruments, both



■ Fig. 3-7

Image of coronal loops observed at the solar limb in the EUV by the Transition Region and Coronal Explorer (Courtesy of the TRACE consortium)



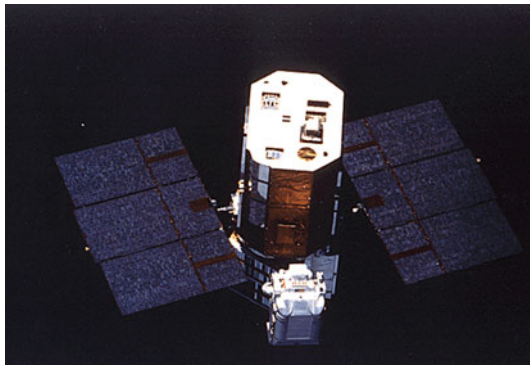
■ Fig. 3-8

Hinode/SOT image of the magnetic field of a sunspot. The signal is proportional to the line-of-sight magnetic field density in the photosphere

imaging and spectroscopic, observing from the UV to the X-rays. Naval Research Laboratory's S082A instrument (often affectionately called the “overlap-ogram”) on the ATM had an exceptionally good spatial resolution (better than $2''$) and covered a wavelength range 170–630 Å. Skylab/ATM was a highly successful mission, followed by several data analysis workshops, which brought together observers and theoreticians. The quality and quantity of data (mainly on photographic plates) provided a major impetus for space-based solar physics. Three topics were chosen for study at the Skylab workshops: Coronal Hole and High Speed Wind Streams (Zirker 1977), Solar Flares (Sturrock 1980) and Solar Active Regions (Orrall 1981). These volumes are an excellent starting point as a foundation for research in these fields.



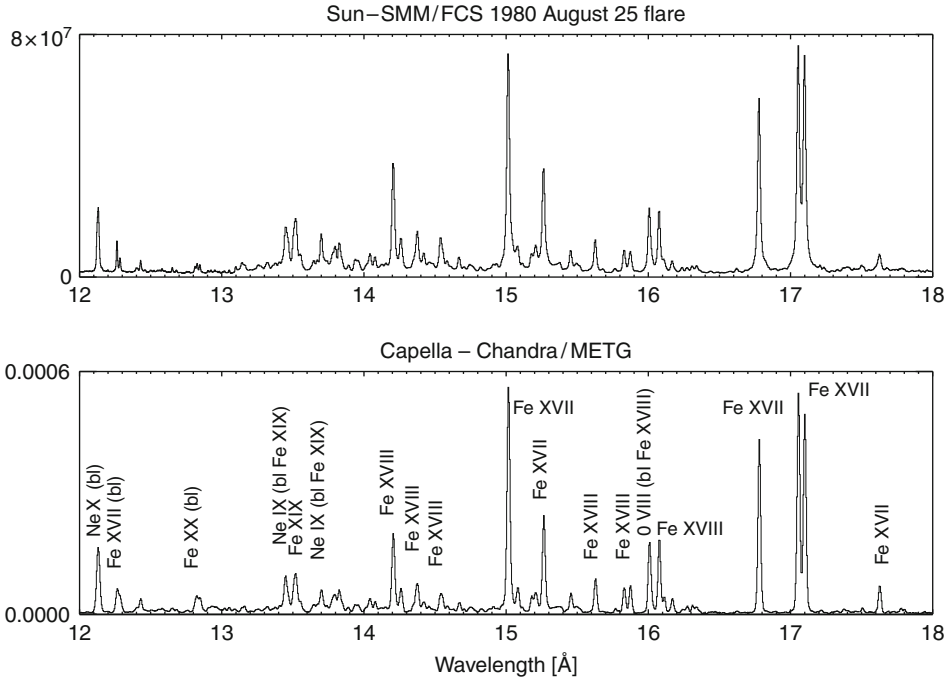
■ Fig. 3-9
The Skylab satellite and Apollo Telescope Mount (courtesy of NASA)



■ Fig. 3-10
The SMM satellite being repaired in space (courtesy of NASA)

February 1980 saw the launch of a new solar space satellite, the Solar Maximum Mission, SMM (cf. ▶ [Fig. 3-10](#)), dedicated to the study of the active Sun, active regions, and solar flares. SMM remained operational until December 1989, with an in-orbit repair by the NASA Space Shuttle in April 1984. SMM carried instruments to record gamma-rays, X-ray emission (both hard and soft), together with a UV spectrometer, a coronagraph, and also an irradiance monitor (ranging from UV to infrared). Preliminary results from SMM were published in a special volume of *ApL*, 1981, (244) and further results were published in a special NASA publication NASA, CP-2439, *Energetic Phenomena on the Sun* (1986).

The SMM X-ray polychromator (XRP) Flat and Bent Crystal Spectrometers (FCS and BCS) instruments produced excellent X-ray spectra of the solar corona, which remain unsurpassed even nowadays, three decades later. ▶ [Figure 3-11](#) shows an XRP/FCS spectrum of a flare, which is remarkably similar to the X-ray spectrum of active stars such as Capella, also shown in the Figure. These X-ray spectra are dominated by Fe xvii and Fe xviii lines in the 12–18 Å range. The XRP/FCS had limited spatial resolution. These data allowed measurements of the



■ Fig. 3-11

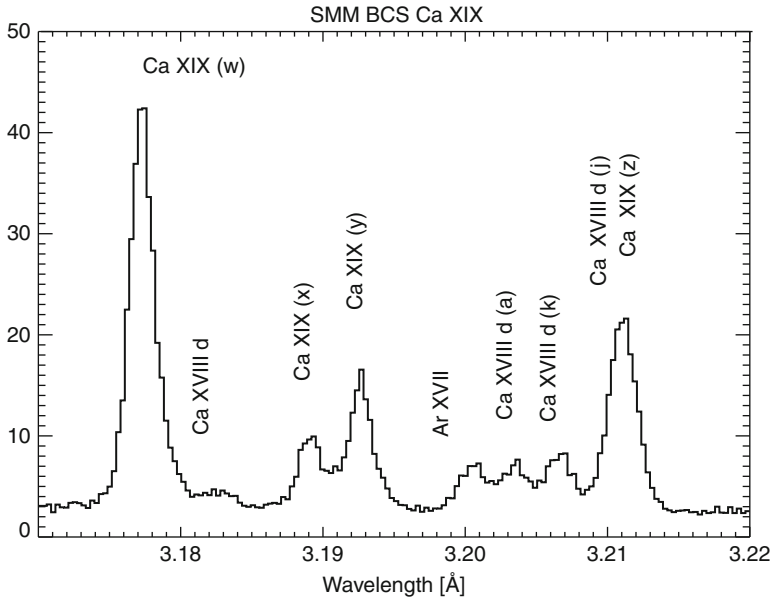
Solar spectrum of a flare from the SMM XRP/FCS instrument (*above*), compared to a Chandra METG spectrum of Capella (Adapted from Del Zanna 2002). Notice the similarities in the spectra

temperature distribution and electron density of solar active regions and flares together with measurements of relative coronal abundances of various elements. The XRP/BCS, which was full disk, observed X-ray line complexes of high temperature (in excess of 10 MK) coronal lines: Fe xxvi, Fe xxv, Ca xix, and S xv. The observed spectral range allowed a wide range of plasma diagnostics to be applied. The He-like ions (Fe xxv, Ca xix and S xv) allowed for example measurements of electron densities and temperatures (Gabriel and Jordan 1969). A sample XRP/BCS spectrum of a flare is given in Fig. 3-12. The resonance w line is the strongest transition, followed by the intercombination z and forbidden x, y. The satellite lines (i.e., those formed by dielectronic recombination) are indicated with a 'd'. The presence of satellite lines allowed some important diagnostic measurements (see, e.g., Phillips et al. 2008).

Other solar X-ray missions included the P78-1 satellite launched in 1979 and the Japanese satellite, Hinotori (meaning *firebird*) launched in 1981. A good overview of results from SMM and Hinotori can be found in Culhane and Jordan (1991).

3.2 Yohkoh

Yohkoh (Japanese for *sunbeam*) was a very successful joint Japanese, UK, NASA satellite launched in August 1991, which operated successfully for a decade until 2001. The instruments on Yohkoh were able to observe the Sun in X-ray and Gamma Ray emission. The spacecraft



■ Fig. 3-12

Solar spectrum of a flare from the SMM BCS instrument, with the resonance (w), forbidden (x,y) and intercombination (z) lines from the He-like Ca. Lines denoted with “d” are formed by dielectronic recombination

carried four instruments: the Soft X-Ray Telescope (SXT), the Bragg Crystal Spectrometer (BCS), the Wide Band Spectrometer (WBS), and the Hard X-Ray Telescope (HXT). The SXT instrument was widely used to study the plasma properties of active regions and solar flares. The SXT was a grazing-incidence X-ray telescope capable of imaging the Sun and resolving features down to $2.5''$ in size (see [Fig. 3-6](#)). Yohkoh/SXT could be used to derive some information about the temperature and density of the plasma by comparing images recorded using different filters. The BCS observed the X-ray H- and He-like line complexes observed by SMM/BCS. Early results from YOHKOH were presented in a special issue of the Publications of the Astronomical Society of Japan, PASJ, 1992, Vol. 4. There have been many conferences and workshops dedicated to results from YOHKOH.

3.3 Ulysses

Most satellites have orbits within the ecliptic. The Ulysses mission was the first and only space probe dedicated to the exploration of the heliosphere out of the ecliptic plane. Indeed, much of our knowledge about the solar wind comes from this unique mission. Ulysses was launched in October 1990 and, after an encounter with Jupiter, started on its journey out of the ecliptic.

3.4 The Solar and Heliospheric Observatory – SoHO

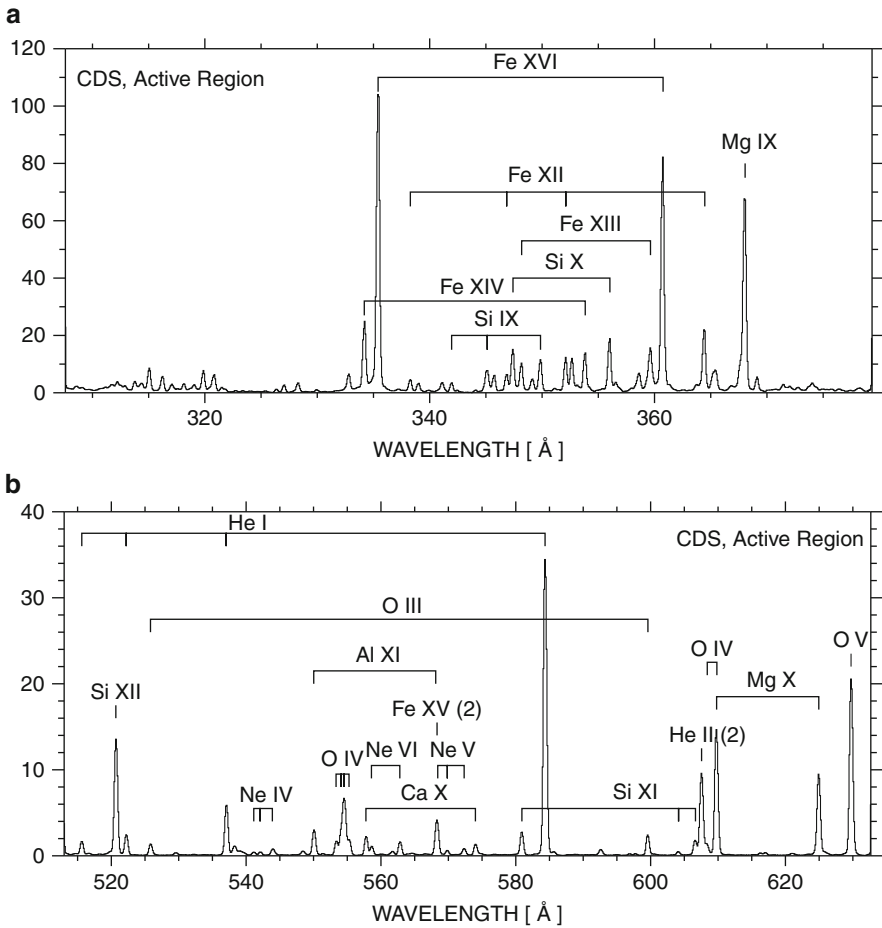
The Solar and Heliospheric Observatory is the most comprehensive and successful solar observatory ever built. SoHO is a joint NASA and ESA mission, which was launched in December 1995 and is still operational. The scientific objectives of SoHO are to study the solar interior, using helioseismology; to investigate the heating mechanism for the solar corona, together with the origin and acceleration mechanism of the solar wind. The SoHO satellite has an unusual orbit, it orbits the Sun at the first Lagrangian (L1) point, allowing the instruments an uninterrupted 24 h view of the Sun.

SoHO carries 12 instruments, including 4 EUV/UV instruments for studying the solar atmosphere. The Coronal Diagnostic Spectrometer (CDS) is a UK-led instrument designed at the Rutherford Appleton Laboratory (RAL). CDS has been used to study the relationship of the transition region and coronal emission – it is designed to determine the physical parameters of the solar atmosphere. The instrument measures EUV emission lines from the Sun's atmosphere in the wavelength range 150–800 Å. The instrument comprises two spectrometers: the Normal Incidence Spectrometer (NIS) and the Grazing Incidence Spectrometer (GIS). The wavelength range covered by the two detectors contains many emission lines. The NIS detector can receive radiation in the two wavelength bands, NIS-1, 308–381 Å and NIS-2, 513–633 Å (see ● Fig. 3-13). To construct monochromatic images (rasters) using the emission lines measured by NIS, a scan mirror is moved across the solar region with a chosen slit (2'' or 4''). One example is shown in ● Fig. 3-14. The CDS instrument has a maximum Field of View (FOV) of 4×4 arcmin² with a spatial resolution of about 5''.

The Solar Ultraviolet Measurement of Emitted Radiation (SUMER) is a high-resolution (spatial and spectral) instrument covering the wavelength range 500–1,600 Å in first and second order (see ● Fig. 3-15). SUMER can resolve fine structures, with a spatial resolution of about 2''. As in the case of the CDS, SUMER has been able to scan solar regions to obtain monochromatic images in selected spectral lines (see, e.g., ● Fig. 3-16). SUMER can also measure Doppler motions (flows) with an accuracy better than 2 km/s and nonthermal line broadening in the chromosphere and transition region.

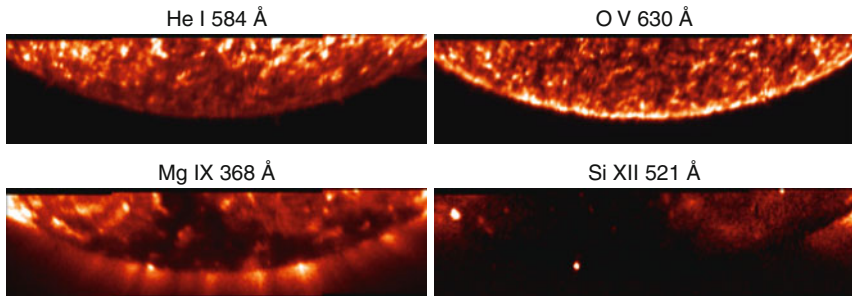
The Extreme-ultraviolet Imaging Telescope (EIT) has provided superb images and movies of the solar atmosphere with a spatial resolution of 2.6'' per pixel. The instrument uses multilayer technology, whereby the reflecting surfaces are coated with layers of various materials. High reflectivities in the EUV are achieved, but images are formed over passbands which are typically 10–50 Å wide. The EIT has four passbands centered on the following wavelengths: 171, 195, 284, 304 Å (see ● Fig. 3-17). In most conditions, the first band is dominated by Fe IX, Fe X formed at 1×10^6 K. The second band is dominated in active regions by Fe XII, formed around 1.6×10^6 K, but has significant contributions from much lower and much hotter lines. The third band is dominated in active regions by Fe XV at 2×10^6 K, but otherwise by transition-region lines. The last band is dominated by the He II chromospheric line 304 Å, but off-limb it is dominated by the coronal line Si XII.

The Ultraviolet Coronagraph Spectrometer (UVCS) can observe the solar corona from its base out to $10 R_{\odot}$. The UVCS spectroscopic diagnostics are based on the measurement of the intensities and spectral line profiles of resonantly and Thompson scattered H I Lyman- α , the collisionally excited and resonantly scattered Li-like resonance lines of O VI (1032 and 1037 Å); it can also detect other coronal lines such as Si XII (499 and 521 Å) and Fe XII (1242 Å) and is rich



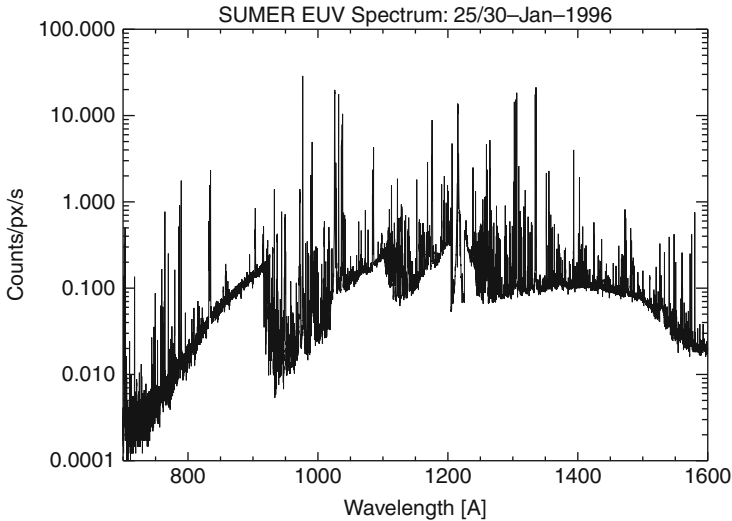
■ Fig. 3-13

SoHO CDS NIS-1 and NIS-2 spectra of an active region (Courtesy of P.R.Young)

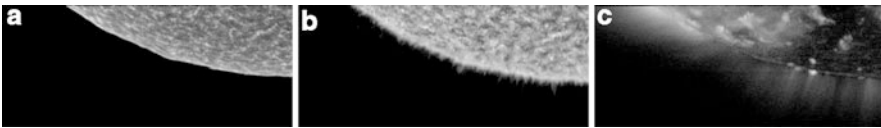


■ Fig. 3-14

Monochromatic images of the south pole on August 11, 1996, from SoHO CDS, as part of the Whole Sun Month campaign (Del Zanna 1999). He I is formed in the chromosphere, while O V in the middle transition region (0.5 MK, notice the limb-brightening), Mg IX in the upper transition region (1 MK), and Si XII in the hot (2 MK) corona



■ Fig. 3-15
A SoHO/SUMER spectral atlas (Courtesy of SoHO/SUMER)



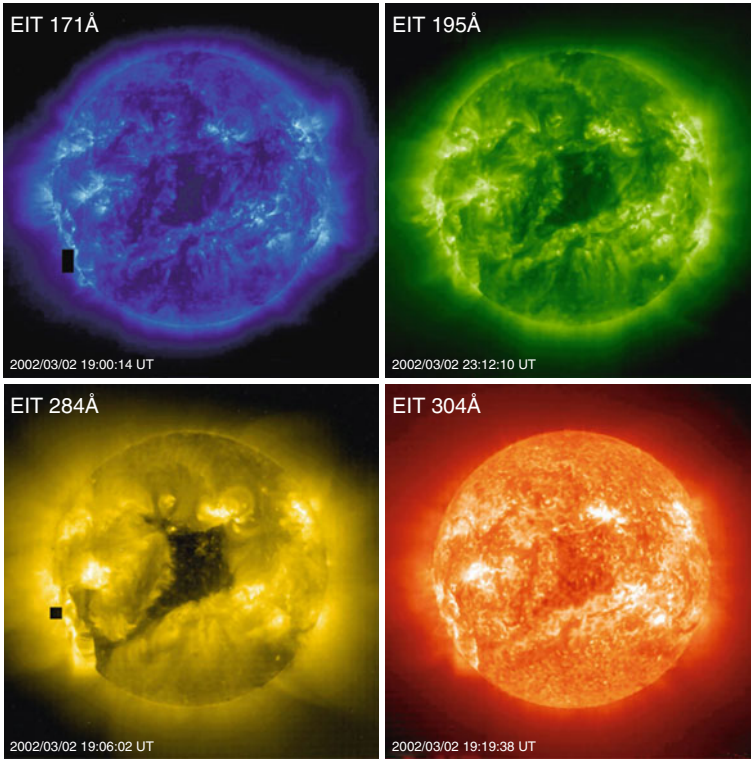
■ Fig. 3-16
A portion of the SE limb of the Sun observed by SoHO/SUMER in 1996 during the Whole Sun Month campaign. The monochromatic images are in C I, O V, and Mg X (a, b, and c respectively). C I is a photospheric line, the O v clearly shows the spicules at the limb, while the hotter (1 MK) Mg X shows the presence of a south polar coronal hole, dark in the image (Courtesy of SoHO/SUMER)

in diagnostic possibilities. ▶ [Figure 3-18](#) shows an O VI monochromatic image of the extended corona obtained by multiple UVCS slit positions around the Sun.

The Large Angle Spectrometric Coronagraph (LASCO) is a wide-field, white-light coronagraph which has provided images of the solar corona from 1.1 to 30 R_{\odot} with different fields of view (C1, C2, C3) and in several wavelength bands in the visible 5,300–6,000 Å. LASCO has provided fascinating observations of streamers, coronal mass ejections (CMEs), and many other large-scale dynamic phenomena. One image is shown in ▶ [Fig. 3-19](#).

In addition, SoHO carries an instrument for studying the photosphere: measuring the photospheric magnetic field and carrying out helioseismology studies. The Michelson Doppler Imager (MDI) uses a pair of tunable Michelson interferometers to record filtergrams. Polarizers are inserted to measure the line of sight, i.e., the longitudinal component of the magnetic field from the Zeeman splitting of the Ni I 6768 Å line with higher resolution (in a central region) or lower resolution (on the full Sun, cf. ▶ [Fig. 3-20](#) left).

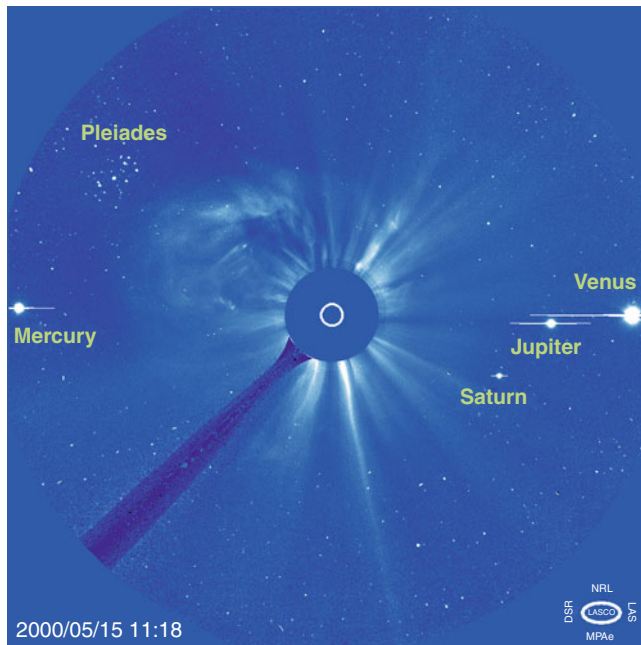
First results from SoHO were published in a special issue of Solar Physics in 1997. There have been many SoHO workshops, focusing on particular topics, during which results from different



■ Fig. 3-17
SoHO EIT images in different filters (Courtesy of SoHO/EIT consortium)

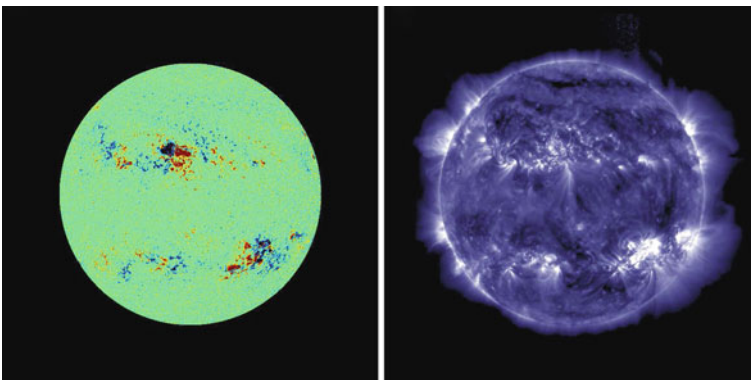


■ Fig. 3-18
Composite of O VI monochromatic image observed from SoHO UVCS. The inset shows a SoHO EIT image (Courtesy of SoHO/UVCS consortium)



■ Fig. 3-19

A SoHO LASCO C3 image, with various planets in the field of view. The white circle in the *middle* of the image indicates the size of the Sun, while the dark feature pointing toward the lower *left corner* is the shadow of the pylon holding the occulter of the coronagraph (Image courtesy of the SoHO/LASCO consortium and Steele Hill (NASA GSFC))



■ Fig. 3-20

Left: line-of-sight magnetogram from SoHO MDI; *right:* mosaic of coronal TRACE 171 Å images from the same day. Notice the obvious correlation between regions of strong magnetic fields and strong intensities in the corona (Courtesy of the SoHO and TRACE consortia)

instruments have been presented and published, starting with the First SoHO workshop held in Annapolis, Maryland, in 1992. One of the particularly successful SoHO workshops was held at St Andrew's University, Scotland in 2004.

3.5 Transition Region and Coronal Explorer (TRACE)

The Transition Region and Coronal Explorer (TRACE) is a very successful NASA small-explorer mission launched in April 2001. The instrument comprises a Cassegrain telescope to observe the solar corona in three EUV wavelength bands (similar to the SoHO/EIT ones), centered around: 171 Å; 195 Å; 284 Å. It also images the H I Lyman-alpha (1,216 Å), C IV (1,550 Å) and UV continuum (1,600 Å), and white light (5,000 Å). TRACE's unprecedented high spatial resolution (of approximately 1'', see [Fig. 3-20](#), right) and cadence (down to 10 s) render this instrument suitable for observing the detailed dynamics of the solar corona.

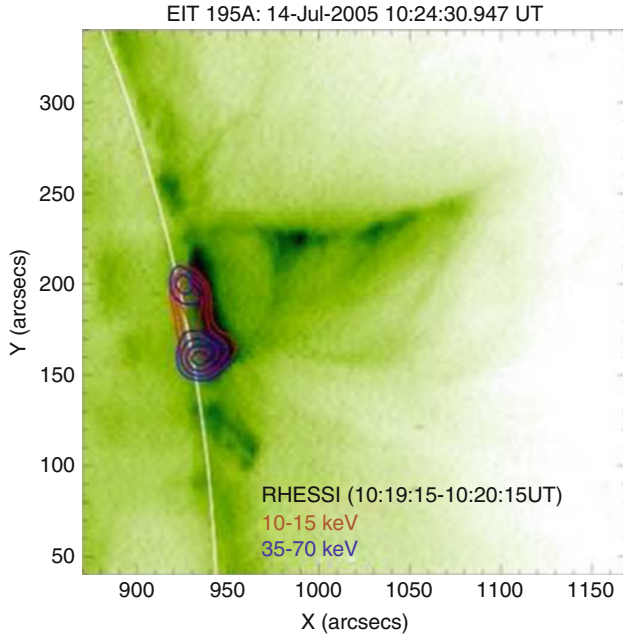
3.6 Ramaty High-Energy Solar Spectroscopic Imager (RHESSI)

The Reuven Ramaty High Energy Solar Spectroscopic Imager (RHESSI) is a NASA mission launched in February 2002 designed to study the particle acceleration and energy release in solar flares. Since its launch, the mission has been providing ground-breaking imaging and spectroscopy measurements from soft X-rays to gamma rays. RHESSI's uniquely high sensitivity at energies 3–15 keV enables studies of large flares, but also small-scale thermal and nonthermal emissions to much lower levels than ever before, from features such as micro-flares.

Obtaining images of high-energy emission from solar flares is extremely difficult. Sophisticated software has been developed to enable X-ray images to be reconstructed from the RHESSI data (see, e.g., [Fig. 3-21](#)). RHESSI also provides high spectral resolution. Spectral fitting techniques enable measurements of the physical parameters (temperature and emission measure) describing the hottest part of the thermal plasma. RHESSI observes thermal free-free and free-bound continuum together with emission lines emitted in the X-ray range 5–20 keV by flare plasmas with temperatures from approximately 7 MK to tens of MK. Furthermore, nonthermal plasma emission can be characterized by fitting models such as *bremstrahlung* from a power-law mean electron distribution. An example of a RHESSI spectrum acquired during a small pre-flare brightening is shown in [Fig. 3-22](#) (Chifor 2008). The ability to measure and image the Fe line complexes provides an additional powerful plasma diagnostic, needed to help separate the thermal and nonthermal continuum and obtain accurate energy estimates.

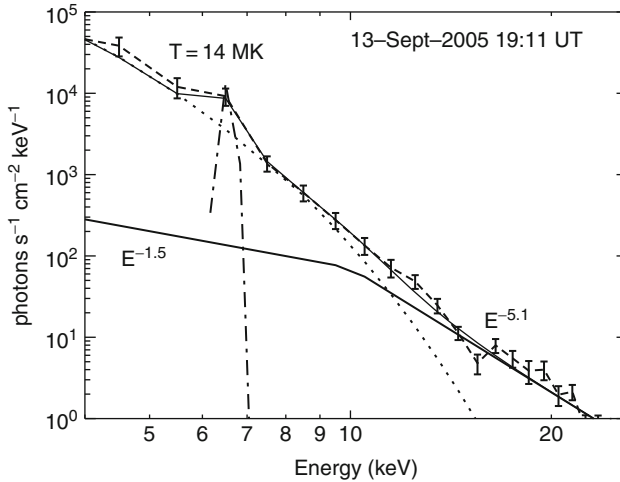
3.7 CORONAS Missions

CORONAS-F, launched in 2001, carried a suite of 15 instruments. It provided XUV monochromatic full-Sun imaging and XUV spectroscopy with the SPIRIT and RESIK suite of instruments. One of the SPIRIT instruments provided images in the Mg XII doublet, formed at a temperature of about 8 MK. A new class of highly dynamic plasma structures were discovered with various characteristic sizes and lifetimes, which still await an explanation (Zhitnik et al. 2003).



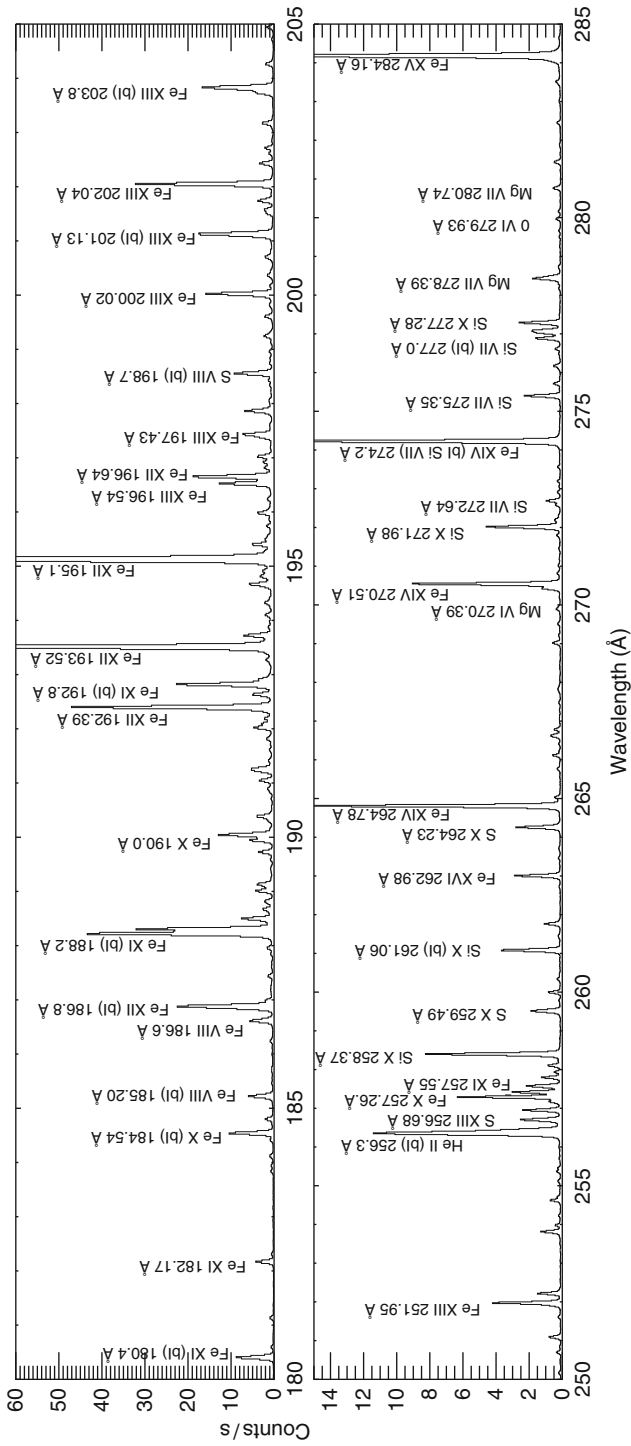
■ Fig. 3-21

RHESSI image (*red and blue contours*), superimposed to a SoHO EIT image during a solar flare at the limb (Courtesy of S. Krucker and H. Hudson)



■ Fig. 3-22

RHESSI spectrum (*dashed curve, with error bars*) of a pre-flare brightening. The thermal continuum was modeled with one isothermal component ($T = 14$ MK, *dotted curve*). One Gaussian function was added to fit the Fe line feature observed ~ 6.7 keV (*dashed-dot curve*). The high-energy tail of the spectrum was fitted with a power-law component $E^{-5.1}$ (*dashed dot-dot-dot*) breaking to $E^{-1.5}$ at energies below 10.5 keV (Courtesy of C. Chifor)

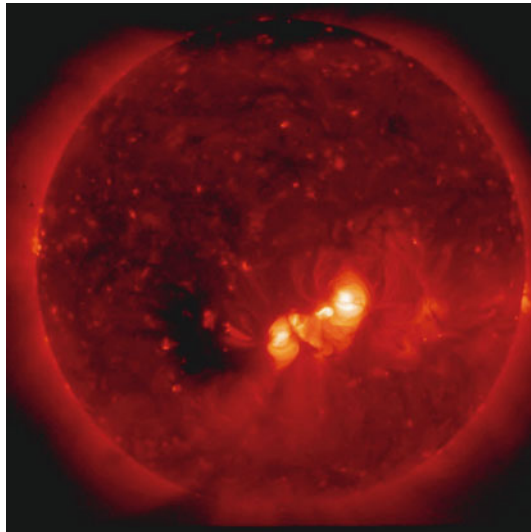


■ Fig. 3-24
Hinode EIS spectrum of an active region

density, together with bulk flow velocities (Doppler shifts), and nonthermal velocities (from line widths). The ten times greater effective areas than previous spectrometers, coupled with a higher data rate than was available from previous SoHO instruments (such as CDS) allow for high-cadence studies of transient phenomena to be undertaken.

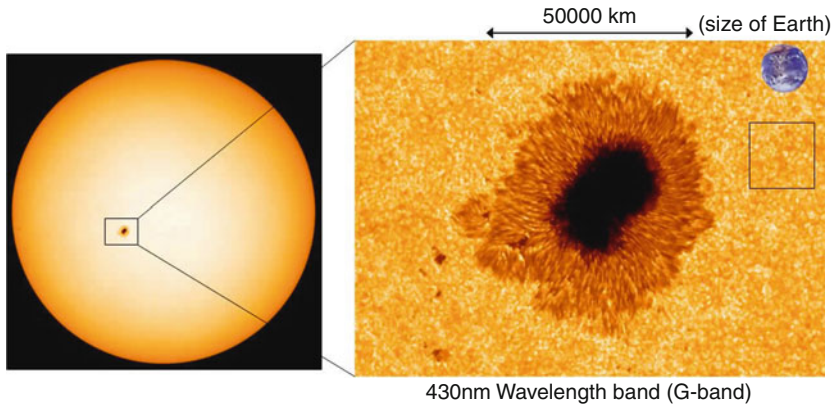
The Hinode/X-ray Telescope was designed to provide an unprecedented combination of spatial and temporal resolution in solar coronal studies. A primary purpose of the Hinode XRT is to observe the generation, transport, and emergence of solar magnetic fields, as well as the ultimate dissipation of magnetic energy in forms such as flares and micro-flares, coronal heating, and coronal mass ejections. High-resolution soft X-ray images reveal magnetic field configuration and its evolution, allowing one to observe the energy build up, storage and release process in the corona for any transient event. One of the unique features of XRT is its wide temperature coverage (1–20 MK) through nine X-ray filters, with $2''$ spatial resolution (see, e.g., [▶ Fig. 3-25](#)). XRT images complement the spectroscopic observations from EIS, by enabling higher cadence and a wider (up to full-Sun) field of view.

The Solar Optical Telescope was designed to provide photometric and vector magnetic images of the photosphere and chromosphere with unprecedented high resolution (see, e.g., [▶ Fig. 3-26](#)) for a long time (ground-based observations can achieve similar resolutions but are limited by *seeing*). The instrument comprises the Optical Telescope Assembly (OTA) consisting of a Gregorian telescope, and the Focal Plane Package (FPP) including a narrow-band (NFI) and a wide-band (BFI) filtergram, plus a Stokes spectro-polarimeter (SP). The time cadence ranges from tens of seconds for both photometric images and vector magnetograms in selected NFI lines to a few hours for a wide-field scan with SP. The maximum field of view is $328 \times 164 \text{ arcsec}^2$. SOT/SP provides the full line profiles in polarized light. The measurements of the Stokes I,Q,U,V signals allows a reconstruction of the vector magnetic field. Initial results from the Hinode satellite have been published in special issues of the PASJ, Science, and A&A journals in 2007 and 2008.

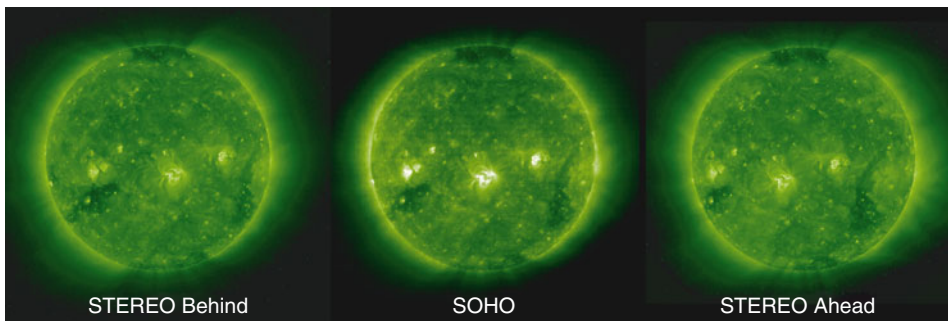


■ Fig. 3-25

Full-Sun X-ray image from Hinode/XRT (Courtesy of the Hinode/XRT team)



■ Fig. 3-26
Image from Hinode/SOT of a sunspot (Courtesy of Hinode/SOT team)



■ Fig. 3-27
EUV images from the STEREO SECCHI behind and ahead spacecraft, together with one from SoHO, showing three different views of the solar corona (Courtesy of STEREO SECCHI consortium)

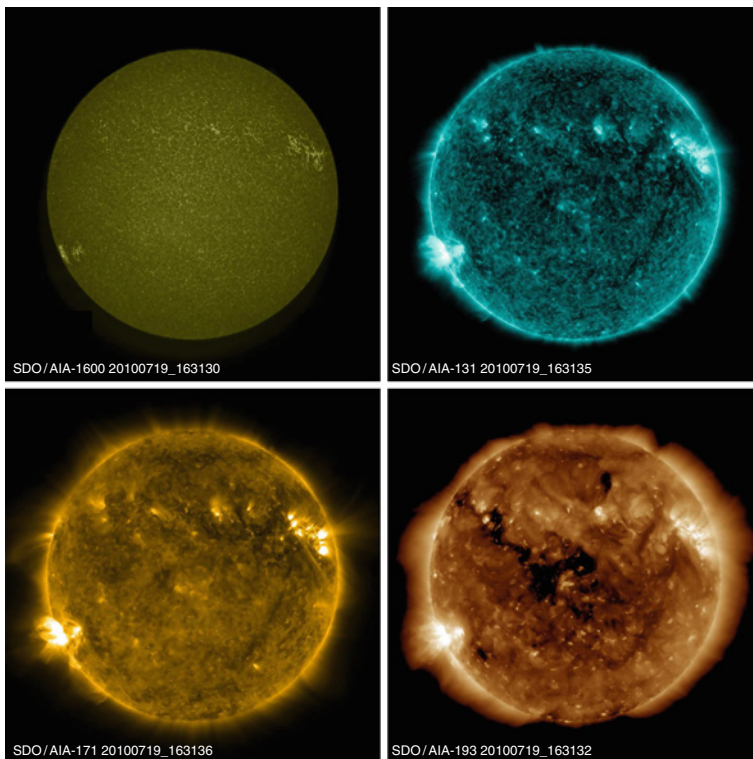
3.9 STEREO

The Solar TERrestrial Relations Observatory (STEREO) is a NASA mission launched in October 2006. The mission comprises the two nearly identical observatories – one Ahead (A) of Earth in its orbit, the other trailing Behind (B), designed to reveal the 3D structure of solar active regions and CMEs. The two spacecraft were launched together and used gravity assistance from the moon to slingshot the spacecraft into a heliocentric orbit. They drift away from Earth at an average rate of about 22.5° per year. Mounted on each of the STEREO spacecraft are four instrument packages: SECCHI, SWAVES, IMPACT, and PLASTIC. Sun Earth Connection Coronal and Heliospheric Investigation (SECCHI) comprises four instruments: an Extreme Ultraviolet Imager (EUVI), two white-light coronagraphs (COR1 and COR2), and a wide angle imaging system for viewing the inner heliosphere (HI1 and HI2). EUVI has a field of view out to 1.7 solar radii, and has four channels (similar to the SoHO/EIT ones) (see 📍 Fig. 3-27). The other instruments on STEREO sample the plasma, solar wind, and CMEs.

3.10 Solar Dynamics Observatory (SDO)

The Solar Dynamics Observatory (SDO) was launched in February 2010 and is providing full-Sun, multiwavelength observations with excellent spatial and temporal resolution. Full-disk magnetic field information is provided from the Helioseismic and Magnetic Imager (HMI). The Atmospheric Imaging Assembly (AIA) provides an unprecedented view of the solar corona, taking images that span at least 1.3 solar diameters in 10 wavelength ranges almost simultaneously, at a resolution of approx $1''$ and a cadence of about 10 s. One example set of images in four passbands is given in [Fig. 3-28](#). Combined with spectroscopic data from existing instruments, the SDO observations promise to advance our knowledge of both small-scale and large-scale solar activity.

The SDO EVE instrument includes two spectrographs and multiple photometers providing the solar EUV irradiance with an unprecedented wavelength range (1–1,220 Å) and temporal resolution (10 s). The EVE spectra are from the Multiple EUV Grating Spectrographs (MEGS) and have about 1 Å spectral resolution. The MEGS A channel is a grazing incidence spectrograph for the 50–380 Å range, and the MEGS B channel is a double-pass normal incidence



■ Fig. 3-28

SDO/AIA images in the 1,600, 131, 171 and 193 Å passbands. In quiet Sun areas, these bands are dominated by continuum (with C IV), by Fe VIII (0.4 MK), Fe IX (0.7 MK), and Fe XII (1.5 MK). Courtesy of the SDO

spectrograph for the 350–1,050 Å range. A prototype of the SDO EVE instrument was launched on board a rocket on April 14, 2008.

3.11 Imaging Versus Spectroscopic Instruments

In order to understand the physical conditions which lead to small and large-scale features of the solar atmosphere, it is essential to determine the local plasma parameters (temperature, density, abundance, flows, magnetic field, etc.) as a function of space and time. This can only be achieved by combining both multiwavelength imaging and spectroscopic observations of the solar atmosphere.

Imaging observations (from instruments such as SoHO/EIT, TRACE, Hinode/XRT, STEREO/EUVI, SDO/AIA etc.) generally provide a higher spatial resolution and cadence, with a wider FOV than spectroscopic observations (e.g., rasters which use a narrow slit when building up images). On the other hand, spectroscopic observations from instruments such as SoHO/CDS and Hinode/EIS are capable of observing individual spectral lines which provide both line profiles and line intensities.

Phillips et al. (2008) provide a recent review of solar UV and X-ray spectroscopy. Spectral line profiles provide information about the line shift (Doppler motion) and line width (from which thermal and nonthermal broadenings can be determined). The intensities of the spectral lines from some ions are sensitive to electron temperature or electron density. These may be used as diagnostics to probe the physical properties of the solar plasma, including temperature distributions, densities, filling factors (indicating to what extent the observed features are spatially resolved), and elemental abundances.

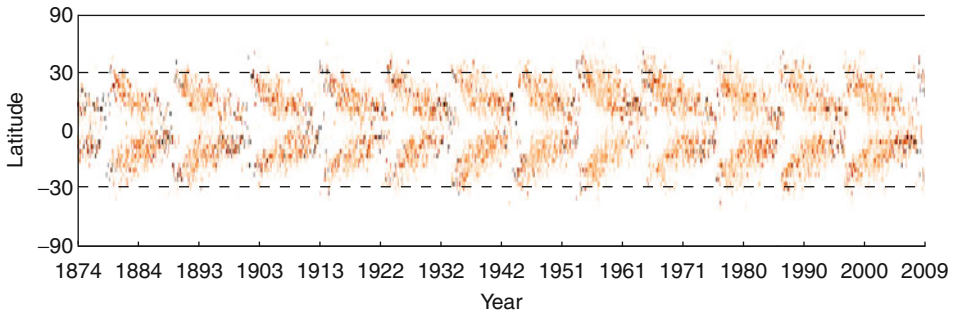
The vast array of solar instrumentation over the past three decades has enabled us to examine the solar atmosphere in microscopic detail, which sometimes seems overwhelming. It is a great challenge to be able to explain the dynamic and transient nature of the solar atmosphere.

4 The Lower Solar Atmosphere

4.1 The Photosphere and the Sun's Magnetic Field

For a detailed description of the photosphere see Thomas and Weiss (2008). The most prominent feature of the photosphere are the sunspots. Detailed observations of sunspots have been obtained by Zürich Observatory since 1849 and the Royal Greenwich Observatory since 1874. These records include information on the size and position of sunspots as well as the number. Various aspects of sunspots have been defined and used as a proxy of solar variability. The first was introduced by Rudolf Wolf of the Zürich Observatory, the Wolf Sunspot Number $WSN = c(10G + N)$, where G is the number of sunspot groups, N the number of individual ones, and c a constant factor. Many different observations existed before 1849, and efforts have been ongoing to build a more complete sample. One noteworthy example is that of Hoyt and Schatten (1998), who defined a Group Sunspot Number (GSN) and collected all archival data available at the time.

Heinrich Schwabe in 1844 was the first to indicate the presence of a solar cycle in the observed variations of the number of sunspot groups. In the second half of the nineteenth



■ Fig. 3-29
The solar butterfly diagram

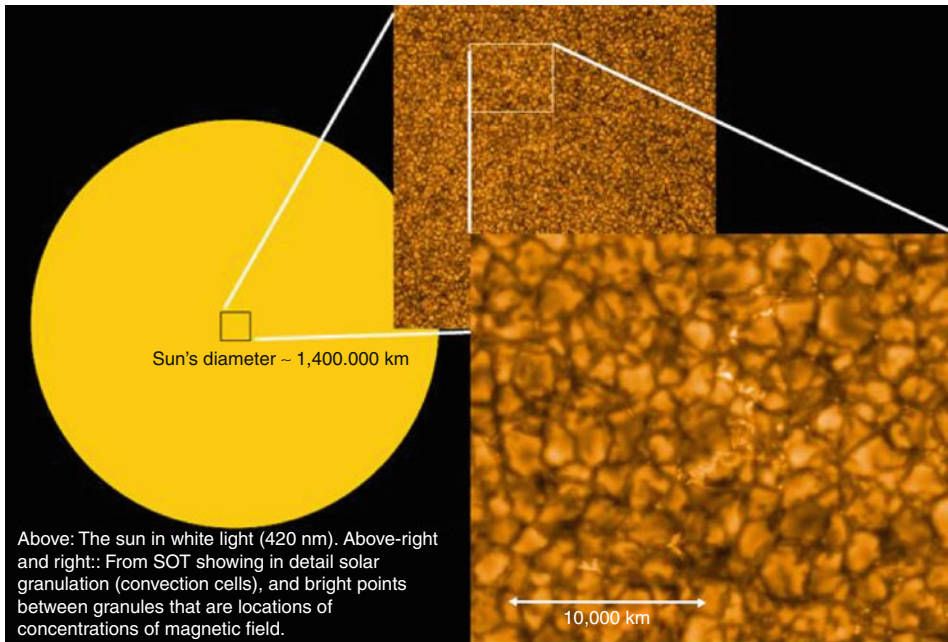
century it was noted by both Carrington and Spörer that as the cycle progresses, sunspots appear first at mid-latitudes, and then closer and closer to the equator until solar minimum is reached. This pattern is best visualized in the form of the so-called butterfly diagram, the first version of which was elegantly produced by Maunder in 1904, using data he collected together with his wife. A butterfly diagram obtained from a collection of data (rescaled and adjusted by David Hathaway.¹) is shown in ► Fig. 3-29. Sunspots for a new solar cycle tend to appear at midlatitudes while larger, more isolated sunspots from the previous cycle still persist.

Hale was the first, in 1908, to measure magnetic fields on the Sun (in sunspots where it is strongest, up to several 1,000 G). He also showed in 1919 that the orientation of the magnetic field is opposite in the northern and southern hemisphere and that the orientation of the polarities changes every 11 years during a solar cycle. During solar minimum, the solar magnetic field is approximately dipolar. Sunspots tend to be bipolar and slightly tilted compared to the direction of solar rotation (approximately east-west). The polar fields were also found to invert their polarity (Joy's law).

Magnetic flux emergence occurs continuously everywhere on the Sun. Magnetic fragments of opposite polarity tend to emerge and separate in the east-west direction. Sunspots normally form after the coalescence of magnetic fragments, and predominantly in the leading polarity (the western one). Sunspots appear dark because their temperature is much lower than the surroundings, an effect caused by the strong magnetic field (convection beneath the sunspot is inhibited). Most sunspots have an umbra and a penumbra, together with an associated (bright) plage area. Small bipolar regions continuously emerge at all latitudes on the Sun. This was seen clearly with the SoHO/MDI observations. The whole *magnetic carpet* for the quiet Sun was found to be replaced over approximately 40 h. The better the spatial and temporal resolution which is achieved in the observations, the more dynamic the Sun appears. For example, the Hinode/SOT observations show flux emergence and cancellation occurring on spatial scales smaller than $1''$, and with temporal cadence of minutes or less.

On closer inspection the apparently smooth surface of the Sun, the photosphere, is seen to actually be made up of many small granules each of around 15–2,500 km across. ► Figure 3-30 shows as an example a recent image from the Hinode SOT instrument. Time sequences of images show that these granules are in continuous motion. Granules last on average 18 min,

¹<http://solarscience.msfc.nasa.gov/greenwch.shtml>



■ Fig. 3-30

First-light image from Hinode SOT showing the granular pattern in the solar photosphere (Courtesy of Hinode SOT)

and are formed by convection – upward motions of hotter material which then cools and falls back down in the intergranular lanes (observed as dark channels). Relative velocities of the up- and down-flows are only about 2 km/s.

There are also large-scale motions that form the *supergranular pattern*. Slow (0.4 km/s), almost horizontal flow from the center of cells, which are about 30,000 km in size, brings structures toward a boundary, where downflows of about 0.1 km/s are observed (Leighton et al. 1962).

The typical strength of magnetic flux elements in the supergranular cell centers is of the order of 10–20 G. About 90% of the emergent magnetic flux is located in the network, with discrete elements that have strengths up to two orders of magnitude higher (Stenflo 1989).

The region of the upper photosphere and chromosphere extends up to several thousand kilometer above the visible surface. Here, the density and pressure decrease with a scale height of only a few 100 km. The magnetic flux elements naturally expand their horizontal cross section to keep the pressure balance with the surrounding plasma. Within this layer, it is predicted that most flux tubes would either merge with flux of the same polarity or connect to nearby flux elements of opposite polarity to form the so-called *magnetic canopy*.

A significant amount of information is obtained from imaging and spectroscopy of the photosphere in the visible light. Some examples (oscillations, chemical abundances) are provided later in this chapter. However, to achieve a good understanding of what is observed, detailed modeling which includes radiative transfer effects is needed. This is beyond the scope of this chapter.

4.2 The Chromosphere

The chromosphere is the thin region above the photosphere, discovered during eclipse observations through a *flash spectrum*. Chromospheric jets, spicules, and prominences are often readily visible to the naked eye at the solar limb during an eclipse, having a distinctive pink-red color, mostly arising from the strong neutral hydrogen $H\alpha$ and $H\beta$ lines in emission (see [Fig. 3-31](#)).

In the visible, the chromosphere is observable in the strong neutral hydrogen $H\alpha$ and in the singly ionized $Ca II$ H and K lines, which are formed mostly in the middle/higher chromosphere. These lines, in on-disk observations, show wide absorption profiles, which are occasionally self-reversed (e.g., in emission) in the core. A detailed understanding of the $Ca II$ H and K line profiles requires in-depth modeling which takes into account radiative transfer, non-local thermodynamic equilibrium (NLTE), and nonequilibrium ionization effects, not discussed in this chapter. Further recommended reading is Athay (1976), Athay and Thomas (1961), Judge (2006), Rutten (2007).

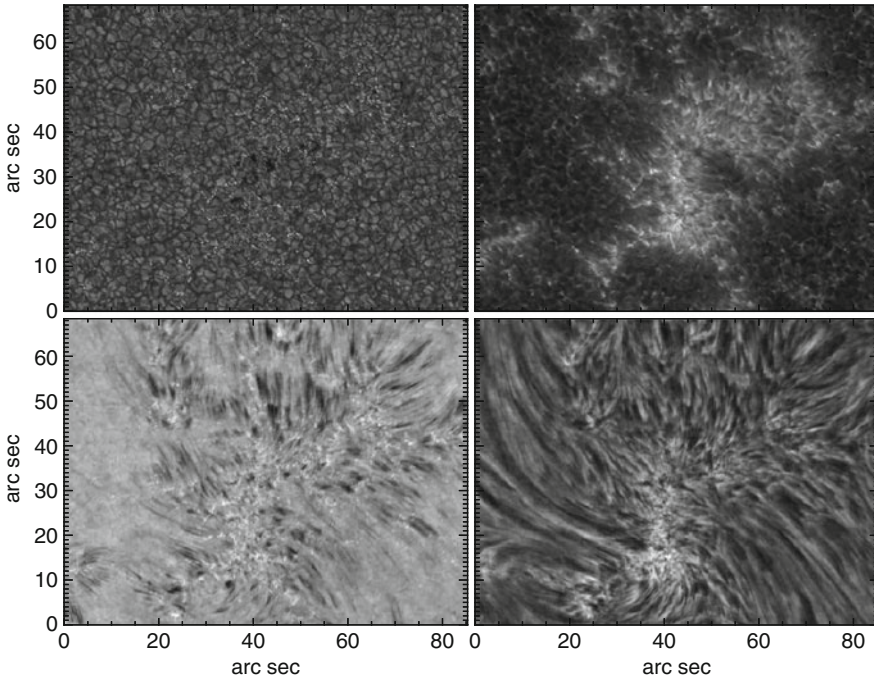
In on-disk observations, these lines show an extremely fine structure, organized in a supergranular cell-network pattern (see [Fig. 3-32](#)), and also very dynamic small-scale activity. At the limb, spicules are observed (see, e.g., [Figs. 3-33](#), and [3-34](#)).

Father Secchi SJ was the first one to make regular spectroscopic observations of the Sun, in particular of the chromosphere. He discovered the solar spicules, dynamic jets about 10,000 km long and 500 km wide, with short lifetimes (10–20 min), and with upward velocities of about 20 km/s (although even higher velocities, up to 100 km/s, have been recently reported using new high-resolution HINODE observations). These spicules tend to either fall back or fade from view. The entire chromosphere is dominated by them, indeed it is estimated that at any one time there are 70,000–400,000 spicules on the Sun. This is the reason why Secchi termed them *prateria ardente* (burning fields). Since Secchi, the dynamical character of the chromosphere has



■ Fig. 3-31

Image of the chromosphere during a total solar eclipse (Courtesy of S.Koutchmy)



■ Fig. 3-32

On-disc images from Dutch Open Telescope (DOT) ground observations in G-band (*top left panel*), Ca II H (*top right panel*), $H\alpha-0.07$ nm (*bottom left panel*), and $H\alpha$ line center (*bottom right panel*) (Figures courtesy of K. Tziotziou)

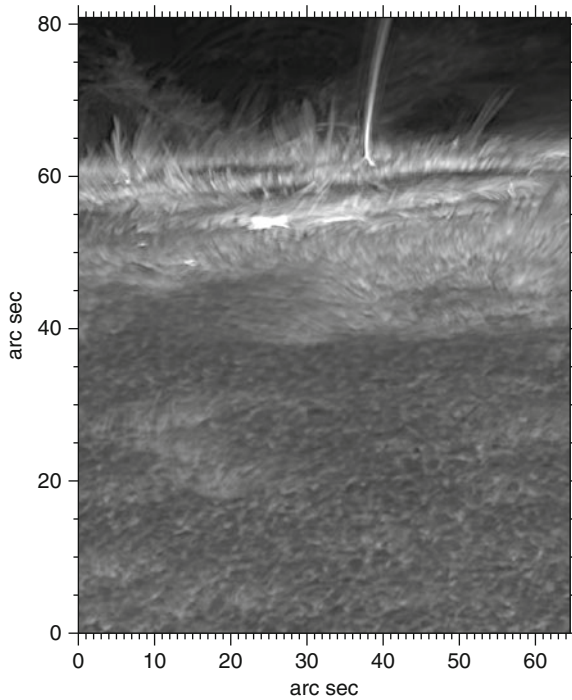
been explored extensively, for example, by Hinode/SOT (see [Fig. 3-34](#)). The chromosphere in coronal holes is similar, although there is the tendency to have a few macro-spicules, i.e., spicules much more extended in length. Interestingly, the thickness of the chromosphere increases at the poles during solar minimum conditions.

Cool “chromospheric” material is often found also at coronal heights, the most prominent example being quiet Sun or active region *filaments*, seen in absorption in on-disc observations, and in emission when observed above the limb called *prominences* (see [Fig. 3-35](#)).

Nowadays, the chromosphere is believed to be the fundamental supplier of mass and energy to the corona, and is also the place where large part of the coronal thermal energy, transferred via thermal conduction and enthalpy, is radiated.

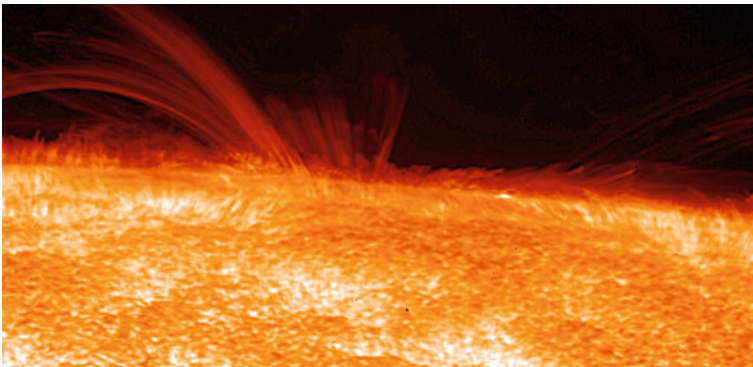
In the UV, observations of the continuum and emission lines provide detailed information about the chromosphere. The H I Ly α alone radiates most of the energy emitted at chromospheric temperatures, which is an enormous amount, about 100 times the total energy required to power the extended solar corona. Other EUV-UV emission lines from neutral and singly ionized elements, in particular He, O, C, and Si, also contribute significantly.

In broad terms, chromospheric emission from the Sun arises from plasma at temperatures between 7,000 K and 25,000 K. The chromosphere is a complex region where hydrogen and the other elements become ionized (hydrogen becomes fully ionized around 20,000 K), and where chemical fractionation processes occurs (see the chemical abundance [Sect. 7](#)). The lower chromosphere has a similar behaviour to the photosphere, being mostly dominated by



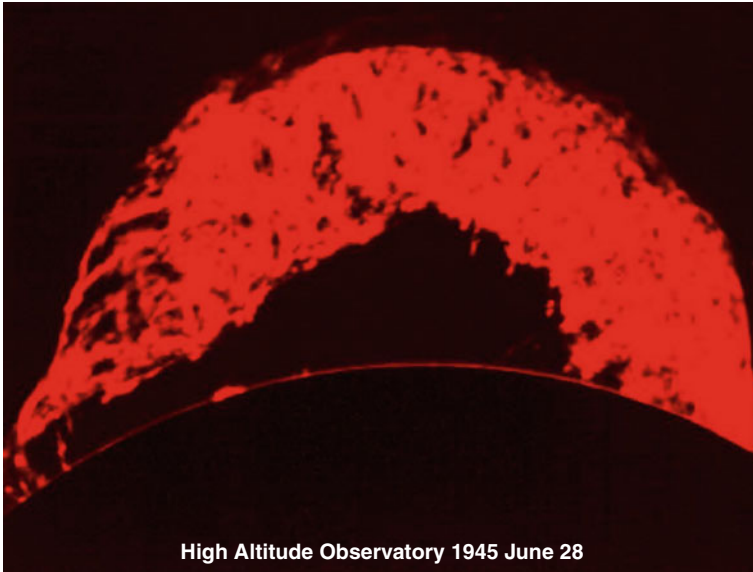
■ Fig. 3-33

A sample DOT Ca II H filtergram showing an active region on the limb on November 4, 2003. The dark pancake structures near the limb are sunspots. The bright large-scale cellular pattern at the bottom of the image is the chromospheric network, while reverse granulation is seen in the inter-network. Numerous jet-like structures are clearly visible on the limb in addition to a large surge (Courtesy of K. Tziotziou)



■ Fig. 3-34

Image of the chromosphere at the solar limb from Hinode SOT (Courtesy of Hinode SOT)



■ Fig. 3-35
The “grand dad” prominence eruption as seen in 1945 in hydrogen $H\alpha$

hydrodynamics. The upper chromosphere (above 1,300 km), on the other hand, is more like the corona, in that the morphology and dynamics of structures (mostly spicules) appear loop-like, being dominated by the magnetic fields. In fact, chromospheric emission is much brighter at the supergranular cell boundaries, where magnetic elements converge, having been advected by the supergranular flows (see ● Sect. 4.1).

Unfortunately, because of the many observational and theoretical complexities, a unified physical explanation of the chromosphere in general, and of spicules in particular, is still lacking. Many theories have been proposed for the formation of spicules, such as shocks resulting from the granular buffeting of flux tubes (e.g., Roberts 1979) and of course magnetic reconnection (e.g., Pikel’Ner 1969; Tziotziou et al. 2003). Another addition to the formation theories is the suggestion (see, e.g., De Pontieu et al. 2004; Suematsu 1990) that spicules form as a result of shocks which arise from the leakage of 5-min p-mode oscillations along tilted field lines in the Sun’s surface.

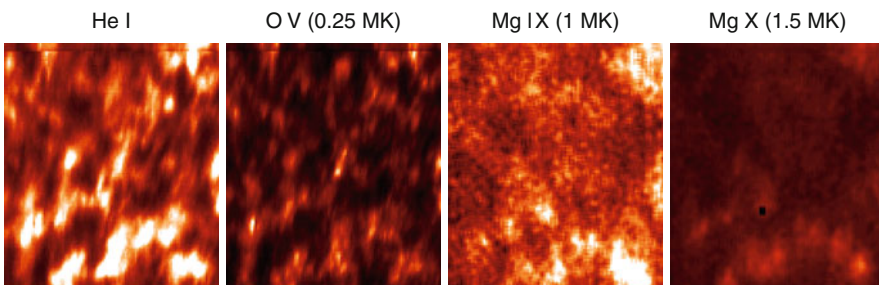
Waves with periods of about 3 min are present in the chromospheric inter-network regions (see ● Sect. 5.2). It was originally proposed that these are standing acoustic modes reflecting within the walls of a cavity formed by the temperature structure of the chromosphere. It was also thought that these p-modes in the chromosphere are not important because the waves could not propagate outside the cavity, however a clear relation between photospheric and lower chromospheric oscillations is observed. Also, some evidence for the presence of traveling waves was found in Skylab data (see the review in Mariska 1992). SoHO SUMER has provided a wealth of observations of photospheric and chromospheric lines and oscillations, which have stimulated modeling. For example, Carlsson and Stein (1997) developed a 1D hydrodynamic model where they studied the response of the lower chromosphere driven by a piston calculated to match the observed variations in a photospheric line. The piston induces the upward propagation of

3-min compressive waves and a shock near 1,000 km above the photosphere. As a result, the inter-network chromosphere below 1,300 km oscillates in response to the p modes. The results of the modeling are in agreement with chromospheric observations, which is a significant progress.

4.3 The Transition Region

In the quiet Sun, the transition region (TR) is clearly observed in emission lines formed between 0.3 and 0.9 MK. The upper TR is the region where lines between 0.6 and 0.9 MK are formed. The emission is optically thin in lines formed above 0.4 MK. Eclipse and spatially resolved observations have shown that the thickness of the TR in the quiet Sun is only about 2,000 km. Observations at the solar limb clearly show the *limb brightening*, an increase in intensity (density), due to the increased line of sight across the transition region. Limb observations show that lines formed at higher temperatures have peak emission at progressively greater heights. Observations on the solar disk instead show that the TR emission is mostly concentrated in the supergranular network, where photospheric magnetic fragments of opposite polarity continuously coalesce. This has been known for a long time (see, e.g., the Skylab ATM observations, Reeves 1976) and has been very clearly shown from SoHO observations (see, e.g. [Fig. 3-36](#)). On-disk observations also show that emission from the quiet Sun at higher temperatures becomes more and more diffuse, until it reaches 1 MK when it becomes totally unresolved at the best spatial resolution ($1''$). Interestingly, there is no significant difference between the transition region in the quiet Sun and in coronal holes.

Some authors (e.g., Feldman 1983 and subsequent papers) have argued that the TR is mostly composed of unresolved fine structures (UFS) which do not physically connect the chromospheric structures with the coronal ones. This view is hotly debated, and future instrumentation with very high spatial and temporal resolution might be needed to clarify this issue. It is however clear that the majority of lower-temperature structures appear to be low-lying, as also shown in Landi et al. (2000), where more details of the quiet Sun TR in the supergranular network can be found. It is also interesting to note that the only coronal structures easily resolvable in



■ Fig. 3-36

Monochromatic images (From a SoHO/CDS synoptic observation near Sun center) of the chromosphere-transition region in the quiet Sun, showing the supergranular network which progressively disappears at higher temperatures

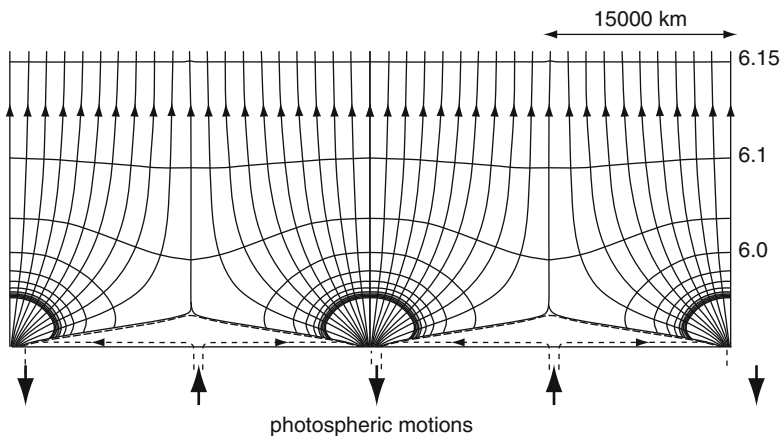
the corona, such as coronal hole plumes and coronal loops, do show a clear connection from chromospheric to coronal temperatures (Del Zanna 2003; Del Zanna et al. 2003).

At high resolution, the TR emission is structured in fine-structure emission similar to the chromospheric plasma (spicules). Dere et al. (1987) used HRTS measurements to show that chromospheric and TR spicular structures *are* the same, however this does not seem to always be the case. Dere et al. (1987) also measured very small filling factors for the TR at 10^5 K of the order of 10^{-4} (see Sect. 6.9), which is interpreted by many as evidence that this region has a filamentary structure.

Early static models of the solar atmosphere (see, e.g., the book by Mariska (1992)) proposed a plane parallel model with the existence of a thin layer, the *transitions region* (TR), with the presence of constant conductive flux from the corona toward the chromosphere, covering temperatures between say 0.3 and 1 MK. The first more physically realistic model of the TR was that of Gabriel (1976), as shown in Fig. 3-37. The strong magnetic fields at the supergranular boundaries exert a strong magnetic pressure, which naturally forces a very large expansion of the strong field, which occupies the majority of space in a small height (1,500 km). The model had various assumptions, one of which was that the supergranular cell had a unipolar magnetic field, something not confirmed by observations. A more refined model was proposed by Dowdy et al. (1986), where only a fraction of the lower-lying magnetic structures would reach the corona.

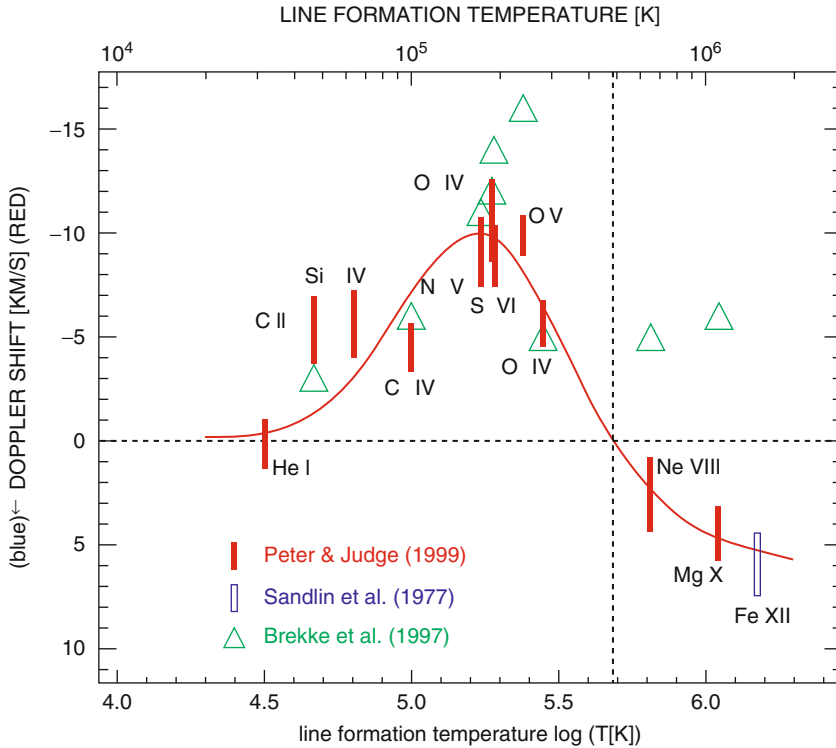
Models of a static plane parallel TR have now become obsolete, mainly because the TR is now known to be very dynamic, in terms of line intensity variations and Doppler motions. However, a clear physical picture of the TR has still not fully emerged.

Transition region spectra are characterized by line profiles much broader than their thermal width. The excess broadening varies with the temperature of formation of the line (see Sect. 6.12). Observations have been obtained by Skylab (Kjeldseth Moe and Nicolas 1977), rocket instruments (e.g., HRTS, see Dere and Mason 1993), and more recently with SoHO SUMER. The nature of this excess broadening puts constraints on possible heating processes.



■ Fig. 3-37

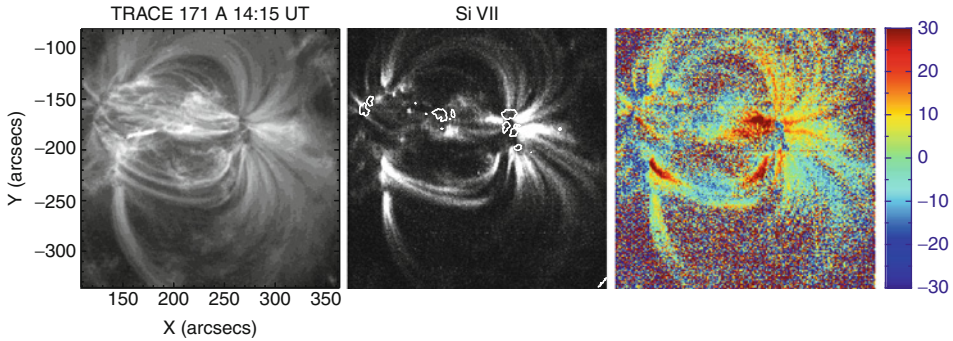
A model of the transition region according to Gabriel (1976) (Revised version courtesy of A. Gabriel), showing the magnetic field and contours of $\log T$ [K]



■ Fig. 3-38
Dopplershifts measured in the transition region

At transition-region temperatures, lines appear red-shifted (see, e.g., ► Fig. 3-38), as shown from the spectrometers aboard OSO 8, the HRTS flights, Skylab, and more recently from the CDS and SUMER aboard SoHO and EIS on Hinode. Stellar UV spectra show the same pattern, which has been considered a puzzle for a long time. Many solar measurements were limited because either did not have good spatial resolution, or they were confined to small regions (Sunspots), or only considered the center-to-limb behavior of the quiet Sun (see, e.g., Peter and Judge 1999). It was only with routine measurements from EIS on Hinode that it became clear that almost all active region loops exhibit strong redshifts in both legs (Del Zanna 2007, 2008). ► Figure 3-39 shows one example. The redshifts at below 1 MK are ubiquitous, sustained, and become stronger toward the footpoints of the loop structures.

These redshifts are possibly the signature of plasma that is cooling and flowing back toward the chromosphere. Indeed, from theoretical considerations, the lifetime of a plasma that is cooling is much longer than the lifetime of a low-density plasma that is suddenly heated. Cooling plasma in the corona is dense and therefore readily observable. The cooling is mostly due to energy lost by radiation that freely escapes and by the enthalpy flux. In fact, the enthalpy flux (Bradshaw 2008; Pneuman and Kopp 1978) is a considerable mechanism by which energy can be transferred from the corona to the chromosphere. Indeed the energy transferred by thermal conduction is estimated to be a small fraction of the energy required to sustain the chromospheric radiative losses.



■ Fig. 3-39

Left: TRACE 171 Å image of an active region, showing warm loops connecting the two opposite magnetic polarities. *Middle:* monochromatic image in Si VII from Hinode/EIS. *Right:* Dopplergram in Si VII from Hinode/EIS, showing redshifts in the legs of all loops (Adapted from Del Zanna 2007)

5 The Interior of the Sun

5.1 The Standard Model and the Solar Neutrinos

The standard solar model assumes that the Sun is a spherically symmetric nonrotating star. The energy produced by nuclear fusion in the core is transferred by radiation until it reaches the outer 30% region of the solar interior. In this region, the radiative gradient exceeds the adiabatic one, and the gas becomes unstable to convection. The convection is observed in the solar photosphere in the form of the granular and the supergranular motions.

The standard model equations are integrated in time from a set of initial conditions in order to match the observed mass, luminosity, diameter, and chemical composition of the Sun at this time. The five structural variables are pressure, opacity coefficient, energy production rate, entropy, and adiabatic exponent, all of which are functions of density, temperature, and chemical abundance.

The age of the Sun is estimated to be 4.6 billion years. Knowledge of the chemical composition of the Sun and stars is nontrivial as discussed in Sect. 7. In particular, the helium abundance of the Sun is not well known. Moreover, it is not clear if the chemical abundances measured at the photosphere are representative of those inside the Sun. The convective motions should maintain sufficient mixing, however diffusion and gravitational settling are also present and could alter the internal composition. The current mass loss of the Sun through the solar wind and eruptions such as coronal mass ejections is negligible, however it is unclear how this has changed with time. The Sun is a relatively slow rotator, however it is likely that this is due to loss of angular momentum via the solar wind, magnetically coupled to the outer convection zone (see the book by Mestel 1999). In fact all young stars are fast rotators.

The rate of energy generation depends on the various ways in which hydrogen is converted into helium by fusion:



The positrons, e^+ , immediately become annihilated by encounters with free electrons, while the electron neutrinos, ν_e , largely escape from the Sun, given their extremely low cross section

for interaction with matter. The energy carried away by the neutrinos is small (about 3%) compared to the total energy released. The neutrinos offer a beautiful link between different branches of physics. The standard hydrodynamic equations, together with atomic physics calculations which provide the opacity term, can predict the status of the solar interior, defining its overall characteristics. Nuclear physics can predict the energy released by fusion and the number of neutrinos produced. We cannot easily measure the status of the solar core; however measurements of neutrinos can confirm the predictions of the various theories. Details about the observations of neutrinos and their relevance for the *solar standard model* can be found in the book *Neutrino Astrophysics* by J.N. Bahcall.

The most efficient path is the pp chain, where a continuum of low-energy (<0.4 MeV) neutrinos is produced. In the ${}^7\text{Be}$ chain, mono-energetic neutrinos are produced. In the ${}^8\text{B}$ chain, a continuum of high-energy neutrinos is produced. The number of neutrinos at 1 AU is about $7 \times 10^{10} \text{ cm}^{-2} \text{ s}^{-1}$. Over the last four decades, various experiments have measured the number of solar neutrinos. Results are normally summarized in terms of the Solar Neutrino Units (SNU), which correspond to 10^{-36} reactions per target atom per second. The first experiment was in the Homestake Gold Mine, South Dakota, and led by R. Davis and J.N. Bahcall, following a suggestion from B. Pontecorvo to use chlorine: $\nu_e + \text{Cl}^{37} \rightarrow \text{Ar}^{37} + e^-$. The first measurements in 1968 gave 3 SNU. The average of results from 1970 to 1995 gave 2.56 ± 0.16 SNU. This experiment is sensitive to high-energy neutrinos, and hence sensitive to the central temperature in the core of the Sun. Standard models predict about 8 SNU for the high-energy neutrinos. This large discrepancy was termed the “solar neutrino problem”.

The Kamiokande and Super-Kamiokande experiments, which measured neutrino scattering on electrons in water, also only detected the high-energy neutrinos. The result was a flux smaller by about a factor of 2 than that predicted by the standard model.

Detection of the lower-energy neutrinos has been made possible by using gallium as a target. The GALLEX/GNO (Gran Sasso laboratory, Italy) and SAGE (Baskan underground laboratory, Caucasus) experiments have yielded values of 77.5/62.9 and 70.8 SNU respectively, again much lower (by almost a factor of 2) than estimated for lower-energy neutrinos (see the review of Dore and Orestano 2008).

A possible solution to the problem came with the idea first introduced by B. Pontecorvo in the 1950s that neutrinos might have mass, and interact with matter by oscillating between the three different types, the electron, muon, and tau neutrino. Details of the oscillation as neutrinos interact with matter were published in the 1970s and 80s.

In 2001–2002, the Sudbury Neutrino Observatory (Ontario, Canada) measured high-energy neutrinos interacting with deuterium and producing Cherenkov radiation. The experiment can measure processes which are sensitive to the different neutrino flavors. Results confirm the predictions based on the neutrino oscillation theory. The same holds for recent measurements from the Borexino experiment (Dore and Orestano 2008). It therefore appears that the solar neutrino problem has been solved. The missing neutrinos were electron neutrinos which had changed to other types on their way to Earth. They therefore escaped detection.


5.2 Solar Oscillations

The first complete observations of solar oscillations were obtained by Leighton et al. (1962). Oscillations with periods of about 5 min in the local Doppler velocity in photospheric absorption lines were observed. The amplitude of the velocity oscillation was about 0.5 km/s,

which is the result of a random combination of a large number (10^7) of individual modes, with a large degree of spatial and temporal coherence. Single modes have tiny velocity amplitudes of less than 20 cm/s. In terms of the relative intensity variation, this corresponds to a few part per million, hence is very difficult to observe. The same observations revealed the supergranular scales in the photosphere.

Ulrich (1970) proposed that these oscillations were due to standing acoustic waves in the solar interior. The theory was further developed by Stein and Leibacher (1974). Deubner (1975) found the predicted ridges in the wavenumber frequency diagram. Each ridge corresponds to a fixed number of nodes in the radial direction (n , see below). Claverie et al. (1979) first reported the 5-min oscillations at low angular, l , degree from full-Sun Dopplergrams.

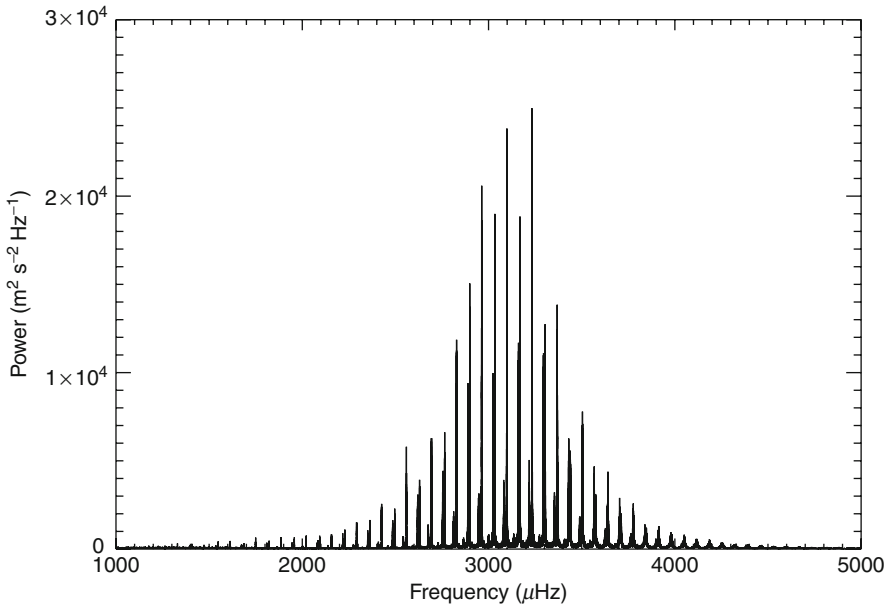
Solar-like oscillations in other stars are very difficult to observe because of their very small amplitudes. However, significant advances in instrumentation have been achieved in the search for extrasolar planets. Accurate radial-velocity measurements are now routinely carried out, to search for signals caused by the motion in the star induced by the gravitational effect of a planet. A number of ground-based observations have found that stars other than the Sun, as expected, also exhibit oscillations. New spacecraft have been launched or are planned in this field of astrophysics. For example, the French-led ESA satellite Convection, Rotation and planetary Transits (CoRoT) has been obtaining data since 2007 from a number of stars and has been measuring stellar oscillations.

Chromospheric lines also show oscillations, clustered around 3 min. These oscillations are characteristic of propagating waves rather than the evanescent waves observed in the photosphere. The modes are spatially coherent and long lasting, hence observations are needed over extended periods of time. Various ground-based networks have been established to study solar oscillations. They often observe the Sun as a star, revealing truly global oscillations. The Birmingham Solar Oscillation Network (BiSON) was established in 1981 and carries out disk-averaged velocity observations by means of potassium-vapor resonant-scattering cells. This provides very accurate measurements of the low degree modes. An example of a power spectrum is shown in  Fig. 3-40. The Global Oscillation Network Group (GONG) has been operational since 1995. Other important observations of low- l modes have come from the LOWL instrument. These ground-based observations are important because they provide long-term records. From these measurements, it has been found that the frequencies of oscillations vary with the solar cycle, for reasons yet to be understood.

SoHO carries three helioseismic instruments. GOLF (Global Oscillations at Low Frequency) was designed as a resonant scattering Doppler-velocity instrument using sodium vapor, but has suffered some technical problems. VIRGO (Variability of solar Irradiance and Gravity Oscillations) measures disk-integrated and low-resolution intensities in three different wavelength regions. SOI/MDI (Solar Oscillations Investigation Michelson Doppler Imager) provides observations of Doppler velocities over the entire solar disk with a spatial resolution of $2''$. SDO/HMI is now providing measurements with a spatial resolution of $0.5''$.

The theory of solar oscillations is complex, however the basic characteristics can be obtained by adopting some basic approximations. Readers are referred to Leibacher and Stein (1981), Christensen-Dalsgaard (2002), Stix (2002); and references therein for more details.

To a first approximation, the rotation and small asphericity of the Sun can be neglected. We know that the timescales for the oscillations are very short when compared to the timescales for energy transport, even the fast timescales given by convection. So, a common assumption is for the oscillations to be adiabatic.



■ Fig. 3-40

Power spectrum of the solar oscillations, obtained from full-Sun Doppler observations. (Courtesy of A.M. Broomhall and the BiSON network)

The amplitude of the oscillations is really tiny, when compared to the size of the Sun, so we are only interested in the linear variations of density and pressure, i.e., small variations around equilibrium. The basic hydrodynamic equations are linearized and a search is made for a stationary solution. The equations become greatly simplified when the approximation due to Cowling (1941) is adopted. Cowling's idea was that the effect of the oscillations on the gravity can be neglected.

During the analytical derivation, three fundamental frequencies are found. The first is the acoustic cutoff frequency $\omega_a = \gamma g / 2c_s$, where $\gamma = 5/3$ for a perfect fully ionized, g is the local gravity, and c_s the sound speed. The second is the frequency of the gravity waves ω_g (known as *Brunt-Väisälä frequency*), which is the natural frequency of oscillation of a plasma element displaced from equilibrium in the presence of gravity. The third is the Lamb frequency ω_L , the frequency of a horizontally propagating sound wave.

By searching for a local solution in terms of a plane wave for the velocity $\vec{v} \simeq e^{i(\vec{k}\cdot\vec{r}-\omega t)}$, dispersion relations can be found between the frequency of oscillation ω and the wavenumber k . Different dispersion relations are obtained when e.g., radial or oblique oscillations are considered.

🔍 *Figure 3-41* (left) presents a diagnostic diagram obtained for a simple isothermal atmosphere, i.e., frequencies versus the horizontal wavenumber k_x . Shaded areas are regions where waves can propagate. For $\omega > \omega_a > \omega_g$ we have acoustic waves that propagate radially, named *p-modes* by Cowling. They are fundamentally acoustic waves modified by the gravity field. These waves can propagate radially only if their frequency is higher than ω_a . In other words, acoustic waves that oscillate too slowly are not allowed to propagate because of the presence of the density stratification created by the gravity. At large wavenumbers, the

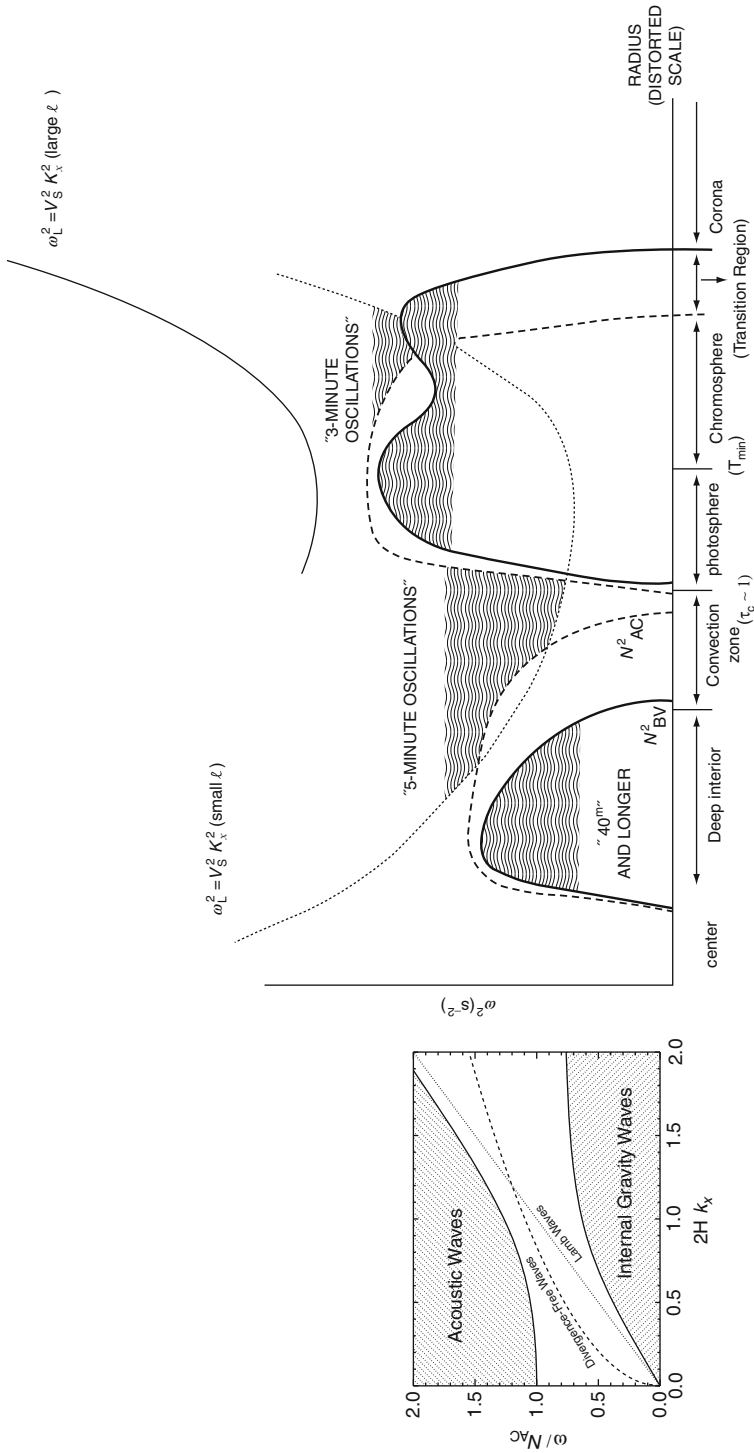




Fig. 3-41


Left: diagnostic diagram for an isothermal atmosphere. The frequency ω , normalized to the cutoff frequency N_{AC} , is shown as a function of the horizontal wavenumber k_x . H is the isothermal scale height for the pressure (and density). Shaded regions indicate where waves can propagate. Right: schematic diagram showing the trapping of 5- and 3-min modes in the solar atmosphere (Courtesy of J. Leibacher). The solid lines indicate the Brunt-Väisälä frequency N_{BV}^0 . The dashed lines indicate the cutoff frequency N_{AC}^2 .

p-modes are bound by the asymptotic Lamb frequency $\omega_L = c_s k_h$. The propagation speed for the high-frequency p-modes is the sound speed c_s . Since their discovery on the Sun, p-modes have received much attention, because it was thought that they could significantly contribute to the heating of the chromosphere.

For $\omega < \omega_g < \omega_a$ we have the *g-modes*, which are *internal gravity waves*, i.e., waves for which the restoring force is the Archimedean buoyancy (still, modified by the fact that the gas is compressible). At large wavenumbers, the g-modes are bounded by the Brunt-Väisälä ω_g frequency, and by the Lamb frequency $\omega_L = c_s k_x$ at low wavenumbers. The g-modes are essentially transverse waves, like the waves on the surface of the sea. There have been contradicting reports about observations of g-modes, and no convincing evidence has yet been found, because of the great difficulty in observing them.

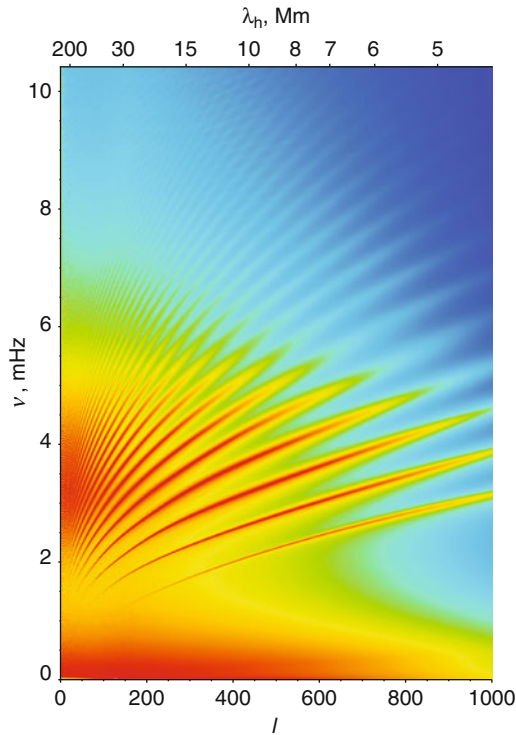
The fundamental modes (*f-modes*) are located in the evanescent-wave region, between the p- and g-modes and are essentially surface gravity waves, i.e., modes without compression. They are observed at large wavenumbers and their dispersion relation is $\omega^2 \simeq g_s k_x$ where g_s is the local surface gravity and k_x the horizontal wavenumber. They are indicated in  Fig. 3-41 (left) as the *divergence-free modes*, because $\nabla \cdot \vec{v} = 0$.

The sound speed is directly related to the temperature ($c_s \sim \sqrt{T}$ for an isothermal atmosphere), so the rapid changes of the temperature with height across the photosphere–chromosphere produce large variations in the sound speed, hence in the acoustic cutoff and Lamb frequencies. As shown in the diagnostic diagram, this in turn can affect the propagation of the acoustic waves. The lower photosphere and upper chromosphere act as two cavities where the acoustic waves become significantly trapped (see  Fig. 3-41, right). The temperature reaches a minimum at around 4500 K, and acoustic modes with periods larger than 3 min and large l become trapped in the photosphere. Acoustic waves also become trapped in the chromosphere when they have periods of 3 min or longer.

The stationary solutions (*modes*) are uniquely characterized by their frequency ω and by their spatial distribution, i.e., their different pattern on the surface of the Sun. This is characterized by two integer numbers, n, l . n is the radial order and represents, to a first approximation, the number of nodes of the radial part of the solution, while the degree l the number of nodes of the angular part on a sphere. When solar rotation is introduced, a third azimuthal number m is required to characterize the solution, and a splitting in the frequencies occurs. Radial modes, with $l = 0$, penetrate to the center, whereas the modes of highest degree observed in the Sun, with $l = 1,000$ (see  Fig. 3-42), are trapped in the outer shell of the Sun, which occupies only a small fraction of a percent of the solar radius. In other words, oscillations of different frequencies probe different layers of the solar interior and carry a great deal of information.

5.3 Some Results from Helioseismology Inversions

The observed frequencies depend on the local values of quantities such as density and temperature in the Sun, and so offer an opportunity to learn more about the solar interior. Densities and temperatures in turn depend on the local opacity and chemical abundances, as well as the details of the energy transport. It is therefore possible, with some assumptions and modeling, to obtain a variety of information from the observed frequencies. The methods and theory are quite involved, see for example Gough and Toomre (1991), Stix (2002), Christensen-Dalsgaard (2002); and references therein. The inversion to obtain the internal solar rotation is the simplest case, since it is linear with the observed splittings in the frequencies.



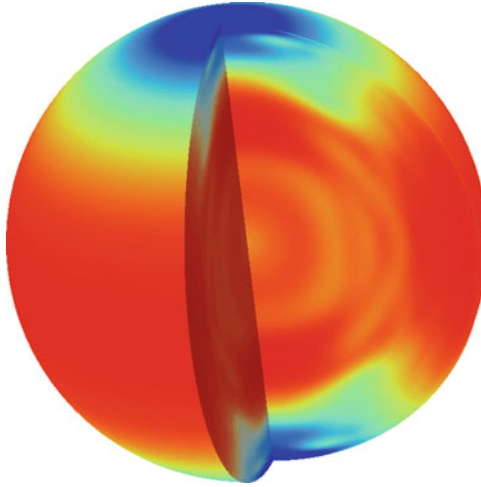
■ Fig. 3-42

Cyclic frequencies $\nu = \omega/2\pi$ as a function of the degree of the mode, l , obtained from SoHO/MDI high-cadence full disk data. Shows mode frequencies up to 10 mHz and $l = 1,000$. Each ridge corresponds to a given value of the radial order n . Courtesy of SoHO/MDI

It has long been known, since the tracking of sunspots (after Galileo), that the solar surface has a differential rotation, with the equatorial regions spinning much faster than the poles. Inversions of ground-based observations (e.g., BBSO) of oscillations did indicate that the differential rotation continued down to the base of the convection zone, but large uncertainties were present in the interior. SoHO/MDI has confirmed that the change in rotation occurs in the zonal belts and extends deep into the convection zone.

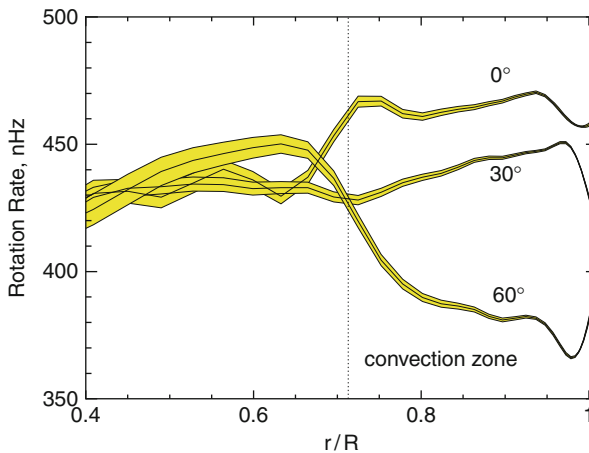
An important discovery from SoHO/MDI has been that the Sun rotates almost rigidly in the radiative zone (cf. ► Figs. 3-43, and ◀ 3-44). These observations were totally unexpected from previous models, and have recently transformed our understanding on the internal rotation in a star (see the review of Thompson et al. 2003). The region where strong shear is present, known as the *tachocline*, is close to the base of the convection zone (as estimated from inversion methods). It is now thought to be the region where magnetic fields are created via hydromagnetic dynamo processes and then transported to the surface by the convective motions. See Tobias and Weiss (2007), Miesch (2005), Charbonneau (2005), Weiss and Thompson (2009) for details.

SoHO/MDI also confirmed the presence of a meridional flow, from the equator to the poles. It was previously deduced from ground-based observations, but thanks to MDI it is now clear that it affects a significant depth of the outer layer of the Sun, down to 10,000 km. The velocity



■ Fig. 3-43

This false-color image represents surface and internal velocities of the Sun as obtained from 1 year of SoHO MDI observations, beginning in May 1996. *Red* indicates greater angular rotation rates, and *dark blue* the slowest. The inner 70% of the Sun is thought to rotate almost as a solid body, whilst in the outer layer there is a marked differential rotation, with the equator rotating faster than the poles. Internal flows of gas at the equator and near the poles are also present (Courtesy of P. Scherrer and the SoHO/MDI consortium)




■ Fig. 3-44

Solar rotation rate inferred from 2 months of MDI data as a function of radius at three latitudes (Courtesy of SoHO/MDI and A. Kosovichev)

of the meridional flow is very slow (about 1%), when compared to the rotation speed, but is fast enough to recycle material within 1 year, a relatively short timescale, compared to the solar cycle. Note that the velocity of this flow is opposite to the changes in magnetic field emergence along the cycle (from high latitudes toward the equator), and it is still not clear what happens

to the flow when it reaches the poles. However, it is clear that the flow must have an important role for the solar cycle.

Helioseismological inversions to obtain information on the solar structure are more complex, because the relation between frequencies and structural quantities is highly nonlinear. The inversion methods are normally based on linearizing the equations for the oscillations (often assumed adiabatic) around a known reference model. The differences between the observed and computed frequencies are then related via some kernels to two model parameters, for example density and sound speed. Various inversion techniques are applied to obtain the variation of the model parameters with radius. The helioseismology results are often presented as the relative differences between the observed and predicted ones.


One parameter, the sound speed, can be measured accurately and does not depend greatly on the solar model used. Accurate measurements were obtained from early ground-based observations, but more accurate ones come from SoHO/MDI.  [Figure 3-45](#) shows the difference in the square of the sound speed between that obtained from 2 months of MDI data and the reference solar model “S” of Christensen-Dalsgaard of 1996. These types of differences are very small but are nonetheless significant, and models are being continuously refined to reduce them.

Another important parameter for the solar structure that is obtained from helioseismology is the location of the bottom of the convective zone.

5.4 Abundances and Helioseismic Models

Parameters such as the chemical abundances are more difficult to derive from helioseismology. The sound speed is directly related to the chemical composition, hence it should be possible to assess whether or not the adopted solar abundances are correct by comparing the variation of the sound speed as predicted by solar structure models with the observed one. However,

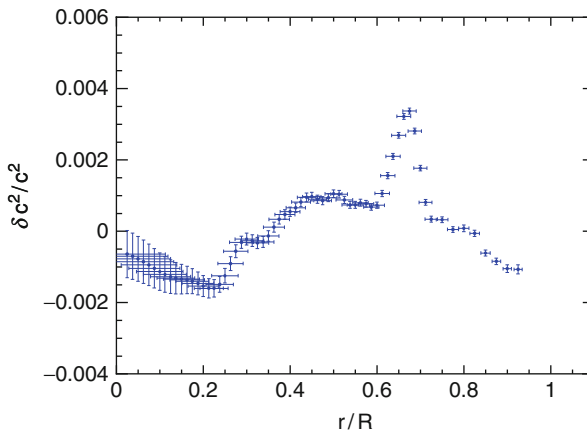


 **Fig. 3-45**

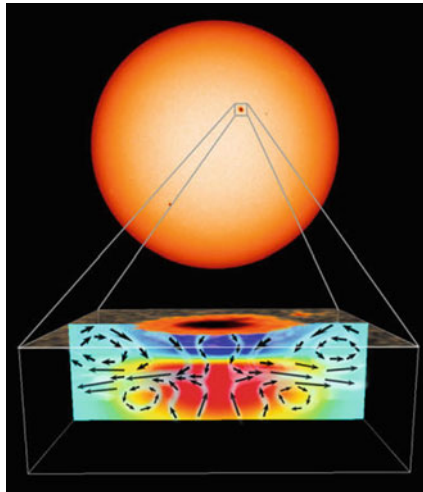
The relative differences between the squared sound speed in the Sun and in a standard solar model, as a function of radial distance (Courtesy of A. Kosovichev)

the methods are complex and depend on several physical assumptions, in particular on the calculation of opacities. For a recent review see Basu and Antia (2008).

Until recently, the predicted sound speed (as a function of depth) from standard solar models showed very good agreement with the helioseismic values. However, adopting the reduced photospheric abundances obtained from the new 3-D simulations causes the opacity to decrease, which in turns reduces the depth of the convection zone, to a level inconsistent with the seismic estimate. See, for example, Serenelli et al. (2009). It appears that the discrepancies cannot be resolved, even with the most recent opacity calculations from the Opacity Project, see Badnell et al. (2005). The He abundance from the latest solar structure models is also at odds with the value inferred from helioseismology. More work is needed in this important area of research.

5.5 Local Helioseismology

Recent helioseismic techniques such as Ring-analysis, Time-distance and Acoustic-holography (see review by Gizon and Birch 2005) measure large-scale flows and sound speed perturbations in and around magnetically active regions (see, e.g., [Fig. 3-46](#)). The interaction of flow fields and observed magnetic fields are important for understanding the stability and long-term evolution of the active regions. It was also established from the innovative work of Braun and coworkers (see Braun and Birch 2008 and references therein) that the sunspots and plages absorb 50–70% of the acoustic power. Unfortunately, it is not clear what changes magnetism causes to the helioseismically determined flows and sound speeds near and within the active regions. Some modeling efforts to assess these have only just begun (e.g., Jain et al. 2009). With the much awaited high-resolution data from the HMI instrument of the Solar Dynamics Observatory, these are exciting times for local magnetic helioseismology.



■ Fig. 3-46

Flow pattern underneath a sunspot, from SoHO MDI helioseismology (Courtesy of the MDI consortium)

5.6 The Solar Dynamo

The issue of the continuous regeneration of the solar magnetic fields is too extensive to be covered in detail in this review chapter. Readers are referred to reviews such as Weiss (1994), Tobias (2004), Miesch (2005), Charbonneau (2005), Solanki et al. (2006). As with the coronal heating problem, many ideas and models have been put forward, but a comprehensive coherent model based on solid physical grounds is still needed. Even the most advanced computations are still not sufficient to model both the fine and large-scale structures in the convection zone. The major problem is how to explain the observed cyclic behavior of magnetic flux emergence on the Sun. During solar minimum conditions, the solar magnetic field is mainly bipolar (poloidal). The differential solar rotation stretches the magnetic field lines and creates a toroidal component. This occurs because the magnetic field is expected to be frozen-in with the plasma motions. In the 1950s, E.N. Parker suggested the idea of a turbulent dynamo, i.e., that within the convection zone, up-flowing volumes of plasma would rotate because of the Coriolis force. This would twist the toroidal field to produce loops in the poloidal plane. Dynamo mean field theory was subsequently developed and became very popular. This theory later failed to explain a variety of features, most importantly the migration patterns and the internal solar rotation as inferred from helioseismology.

In different approaches, the rearrangement of the solar magnetic fields in the solar corona plays a major role. In the Babcock–Leighton (Babcock 1961; Leighton 1964, 1969) mechanism, toroidal field is still produced by the differential rotation of the Sun in the convection zone. This toroidal component creates largely bipolar sunspots that emerge through the photosphere by magnetic buoyancy. It is known (Joy’s law) that bipolar sunspots are normally tilted, so when they decay they tend to create a diffuse poloidal component of the field. The pattern is opposite in the two hemispheres. One current idea is that these weak diffuse poloidal fields are advected toward the poles by the meridional circulation and regenerate the solar poloidal field. There is little doubt now that this occurs on the Sun. What is still not clear is if this is a key component of the dynamo cycle, or just a consequence of it.

In recent years, the importance of considering further effects occurring in the corona has been recognized. For example, Fisk and Schwadron (2001) proposed a theory for the evolution of “open” magnetic flux, by which open field lines continuously reconnect with closed structures, and are subject to the convective diffusive motions on the solar surface. These diffusive motions can explain the accumulation of open flux in the polar regions of the Sun during minimum, and their reversal from cycle to cycle. As a by-product, the reconnection provides mass and acceleration to the solar wind. Another process which is clearly occurring on the Sun is the generation of Coronal Mass Ejections, CMEs, which are global coronal events and can similarly rearrange the large-scale solar fields and become important contributors to the 11-year solar cycle (see, e.g., Low 2001).

6 Radiation from the Solar Corona: Atomic Processes and Plasma Diagnostics

Emission lines result from the spontaneous decay of an excited electron within an ion to a lower energy state, the excess energy being carried off by a photon. The intensity of a particular emission line as measured by an observer clearly depends on the number of emitting

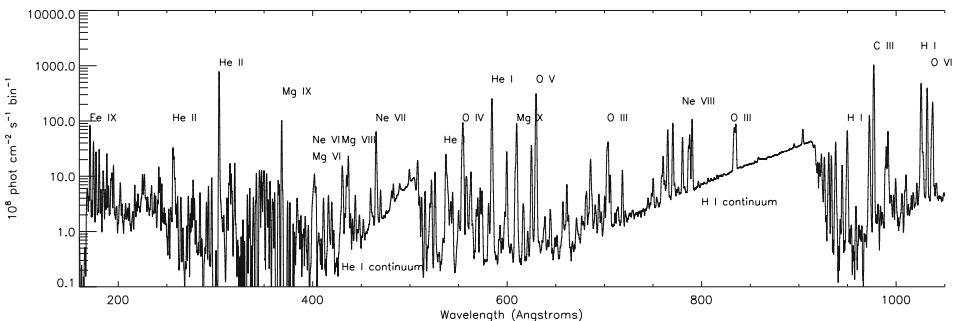
ions in the line of sight and the fraction of these ions that are in the particular excited state that gives rise to the spectral line. We are thus interested in both the *ionization state* of the plasma and the *level balance* within an ion. For each atom there is an ongoing competition between processes changing the ionization state of the ions and processes changing their energy state.

The outer solar atmosphere consists of a hot, low-density plasma. The corona is a fully ionized plasma, being composed mainly of hydrogen and helium fully stripped of their electrons, while heavier elements are at least partially ionized. Hot coronal plasma itself gives rise to line as well as to continuum radiation in the UV to X-ray wavelengths. One can also detect the visible and UV radiation from the lower atmospheric layers, since the low-density corona is *optically thin*.

The EUV spectral range (see ► [Fig. 3-47](#)) is rich in chromospheric lines from He II, lines from the transition region, and coronal lines. It also has continuum emission from hydrogen and helium. The far UV has strong chromospheric lines, the brightest ones being those from H I, but also lines from the transition region, and a few coronal lines.

In principle, knowing the relevant atomic parameters, at a given temperature and electron density, one can determine both the *ionization state* and the energy *level balance* within an ion. From this, the intensity of the emission lines and continuum due to *bound-bound* (from one energy to another within an atom), *bound-free*, and *free-free* electron processes, can be predicted. In practice, however, the calculations represent a very complex task. For each atom, there is an ongoing competition between processes changing the ionization (charged) state of ions (ionization/recombination) on one hand, and processes changing their energy state (excitation/decay) on the other hand. All atomic processes are required to balance their corresponding inverse processes, according to the *principle of detailed balance*.

Reviews of atomic processes and spectroscopic diagnostics for the solar transition region and corona are provided by Dere and Mason (1981), Foukal (2004), Gabriel and Mason (1982), Mariska (1992), Mason and Monsignori Fossi (1994), Del Zanna et al. (2002b), and Phillips et al. (2008).



► **Fig. 3-47**

The EUV spectrum of the whole Sun, as measured by the prototype SDO/EVE instrument flown aboard a rocket in April 14 2008 (Chamberlin et al. 2009; Woods et al. 2009)

6.1 Line Flux and Intensity

When the Sun is observed as a star, the spectral flux (i.e., total irradiance in a line), $F_T(\lambda_{ji})$, for an optically thin line of wavelength λ_{ji} (frequency $\nu_{ij} = \frac{c}{h\lambda_{ji}}$, where h is Planck's constant) is defined as:

$$F_T(\lambda_{ji}) = \frac{1}{4\pi d^2} \int_V P_{ji} dV \quad (\text{erg cm}^{-2} \text{ s}^{-1}) \quad (3.2)$$

where d is the Sun/Earth distance, $P_{ji} = N_j(X^{+m})A_{ji}h\nu_{ji}$ is the power emitted ($\text{erg cm}^{-3} \text{ s}^{-1}$) in the line per unit volume (also called the line emissivity). Here i, j are the lower and upper atomic levels, A_{ji} is the spontaneous radiative transition probability, and $N_j(X^{+m})$ is the number density of the upper level j of the emitting ion. The integral is over the volume V of the emitting plasma.

Most solar observations are spatially resolved, so what is measured is the radiance, or intensity $I(\lambda_{ij})$, of an optically thin spectral line emitted from a volume V , which is:

$$I(\lambda_{ij}) = \frac{h\nu_{ij}}{4\pi} \int_V N_j(X^{+m}) A_{ji} dV \quad [\text{ergs s}^{-1} \text{ sr}^{-1}] \quad (3.3)$$

In practice, the spatial resolution of the instrument defines the volume of plasma, $V = Sh$, where S is the projected area of the instrument aperture, the solid angle and h is the line of sight through the emitting plasma.

There are many processes that cause changes in the energy state for an emitting ion, due to its electrons transitioning between different energy levels. For instance, an ion in its ground state configuration becomes excited when one of its electrons makes a transition to a higher energy level. Similarly, the same ion may return to the ground state configuration when the excited electron falls back down to the ground energy level.

Generally, the processes that populate/depopulate the excited levels of an ion are much faster than the processes affecting the charged state of the ions (ionization/recombination). Thus, the problem of calculating the excited level populations can be separated from that of calculating the ionization state. The population of the level j is then often expressed as:

$$N_j(X^{+m}) = \frac{N_j(X^{+m})}{N(X^{+m})} \frac{N(X^{+m})}{N(X)} \frac{N(X)}{N(H)} \frac{N(H)}{N_e} N_e \quad (3.4)$$

- $N(X^{+m})/N(X)$ is the ionization ratio of the ion X^{+m} relative to the total number density of element X
- $A(X) = N(X)/N(H)$ is the chemical abundance of element X relative to hydrogen ($N(H)$ or N_H);
- $N(H)/N_e$ is the hydrogen density relative to the free electron density. In the literature, it is often assumed to be equal to 0.83 (assuming fully ionized plasma and assuming $N(H)/N(\text{He}) = 10$), however this value depends on the ionization state and helium abundance.
- The fraction $N_j = \frac{N_j(X^{+m})}{N(X^{+m})}$ of ions X^{+m} lying in the state j .

In this case we can express the line intensity as:

$$I(\lambda_{ji}) = \int_h N_e N_H A(X) G(N_e, T, \lambda_{j,i}) dh \quad (3.5)$$

where $G(N_e, T, \lambda_{j,i})$, sometimes denoted as $G(T)$, the *contribution function* is calculated from atomic parameters for that spectral line. $G(T)$ has a very strong dependence on temperature, through the ionization balance calculations, and a weak dependence on electron number density, N_e .

6.2 Differential Emission Measure and Emission Measure

If a unique relationship exists between N_e and T , a differential emission measure $\text{DEM}(T)$, a function of only the plasma temperature, can be defined (Withbroe 1978):

$$\int_T \text{DEM}(T) dT = \int_h N_e N_H dh \quad (3.6)$$

i.e.,

$$\text{DEM}(T) = N_e N_H \frac{dh}{dT} \quad [\text{cm}^{-5} \text{K}^{-1}] \quad (3.7)$$

For example, if we assume that the plasma pressure, P , along the line of sight is constant, then from the perfect-gas law $N_e^2 \sim (P^2/T^2)$, and the electron density is only a function of temperature, and the $\text{DEM}(T)$ can be defined.

The DEM gives an indication of the amount of plasma along the line of sight that is emitting the radiation observed and has a temperature between T and $T + dT$. For a plane parallel atmosphere, the DEM can be related to the conductive flux and can give information about the structure of the atmosphere. With this definition, the intensity integral becomes

$$I(\lambda_{ij}) = A(X) \int_T G(T) \text{DEM}(T) dT, \quad (3.8)$$

where the abundance of the element $A(X)$ is assumed to be constant along the line of sight. We therefore have a system of Fredholm integrals of the first species to be inverted, in order to deduce the DEM from a set of observed intensities. This inversion procedure is notoriously difficult (see, e.g., Craig and Brown 1976).

Once the differential emission measure DEM is known, the *total column emission measure* EM_h can be calculated by integrating the DEM over the whole temperature range:

$$EM_h \equiv \int_h N_e N_H dh = \int_T \text{DEM}(T) dT \quad [\text{cm}^{-5}] \quad (3.9)$$

When fluxes are observed, instead of intensities, the *volume emission measure* $EM_V = \int_V N_e^2 dV$ (cm^{-3}) and its differential in temperature $\text{DEM}_V(T) = N_e^2 \frac{dV}{dT}$ are defined accordingly.

6.3 Atomic Processes Affecting the Ion Excitation

The number density population of level j is calculated by solving the statistical equilibrium equations for a number of low-lying levels and including all the important collisional and

radiative excitation and de-excitation mechanisms:

$$\frac{dN_j}{dt} = \sum_{i<j} N_i R_{i,j} + \sum_{i>j} N_i A_{i,j} + \sum_{i>j} N_i N_e C_{i,j}^e + \sum_{i<j} N_i N_e C_{i,j}^e - N_j (\sum_{i<j} A_{j,i} + \sum_{i>j} R_{j,i} + N_e \sum_{i<j} C_{j,i}^e + N_e \sum_{i>j} C_{j,i}^e) \quad (3.10)$$

- * C^e ($\text{cm}^{-3} \text{s}^{-1}$) are the electron collisional excitation rate coefficients. $N_e C_{i,j}^e$ gives the number of electron collisional transitions per unit time such that an ion changes its state from i to j .

The proton collisional coefficient can be considered as an additional term. Proton collisions are important when excitation energies are small, $\Delta E_{i,j} \ll kT_e$. This happens, for instance, for transitions between fine structure levels within the ground configuration of an ion at high temperatures, as for example the Fe XIV transition in the ground configuration: $3s^2 3p$ (${}^2P_{1/2} - {}^2P_{3/2}$) as explained in Seaton (1964a).

- * $A_{j,i}$ (s^{-1}) are the spontaneous radiation transition probabilities.
- * $R_{j,i}$ (s^{-1}) are the stimulated absorption rate coefficients, proportional to the mean intensity of the radiation field. Photoexcitation and stimulated emission are important processes which also need to be included in the level balance equations. It is possible to show that this can be simply done by replacing the $A_{i,j}$ value with a generalized radiative decay rate.

In practice, because of the short timescales of the relevant processes, for the solar corona it is normally assumed that the plasma is in a steady state ($\frac{dN_j}{dt} = 0$). The set of equations 3.10 is then solved for a number of low-lying levels, with the additional requirement that $N(X^{+m}) = \sum_j N_j$.

The electron collisional excitation rate coefficient for a Maxwellian electron velocity distribution with a temperature $T_e(K)$, is given by

$$C_{i,j}^e = \frac{8.63 \times 10^{-6}}{T_e^{1/2}} \frac{Y_{i,j}(T_e)}{\omega_i} \exp\left(\frac{-\Delta E_{i,j}}{kT_e}\right) \quad (3.11)$$

where ω_i is the statistical weight of level i , $\Delta E_{i,j}$ is the energy difference between levels i and j , k is the Boltzmann constant and $Y_{i,j}$ is the thermally averaged collision strength:

$$Y_{i,j}(T_e) = \int_0^\infty \Omega_{i,j} \exp\left(-\frac{E_j}{kT_e}\right) d\left(\frac{E_j}{kT_e}\right) \quad (3.12)$$

Here the collision strength (Ω) is a symmetric, dimensionless quantity, which is related to the electron excitation cross section; E_j is the energy of the scattered electron relative to the final energy state of the ion. The electron de-excitation rates are obtained by the application of the principle of the detailed balance.

$$C_{j,i}^e = \frac{\omega_i}{\omega_j} C_{i,j}^e \exp\left(\frac{\Delta E_{i,j}}{kT_e}\right) \quad (3.13)$$

The solution of the electron-ion scattering problem is complex and takes a great deal of computing resources. The accuracy of a particular calculation depends on two main factors. The first is the representation which is used for the target wavefunctions, the second is the type of scattering approximation chosen. The collision strengths usually have a slowly varying part and spikes that are due to resonances (dielectronic captures). The theory on electron-ion collisions has been developed by Seaton (1964b). Calculations can be very accurate (better than 10%),

but are not trivial for many ions. The target must take account of configuration interaction and allow for intermediate coupling for the higher stages of ionization. The main approximations used for electron-ion scattering are *Distorted Wave* (DW), *Coulomb Bethe* (CBe) and the more elaborate *Close-Coupling* (CC) approximation. In the CC approximation, the scattering electron sees individual target electrons, the channels are coupled and a set of integro-differential equations are solved.

There are an abundance of electron scattering calculations for individual ions in the literature. The complexity of iron ions leads to many spectral lines and useful diagnostics, but also means atomic calculations are difficult. The Iron Project, an international collaboration of atomic physicists, was set up to calculate electron excitation rates for all the iron ions (Hummer et al. 1993). A series of Iron Project papers have been published in *Astronomy and Astrophysics*. A large set of excitation data have also been produced recently by the UK Rmax and APAP networks. The most accurate calculations for coronal iron have been performed by P.J.Storey and collaborators. Other international groups, for example at Queen's University of Belfast, have also produced extensive atomic data. Atomic data has been assessed and gathered in various databases, for example the CHIANTI database discussed below.

6.4 Atomic Processes Affecting the Ion State


Since the coronal plasma is optically thin, most of the radiation escapes, the plasma is not in local thermodynamic equilibrium (LTE), and the main processes that regulate the ionization balance are spontaneous radiative recombination, di-electronic recombination, photoionization, and collisional ionization. By considering the detailed balance equations that relate successive ionization stages for these processes and requiring that the population of ions in a given state is constant with time, it is possible to derive for each state the ratio of two successive ionization stages $N(X^{+m+1})/N(X^{+m})$, which is mainly a function of the temperature, and only slightly depends on the electron density. With the additional condition $N(X) = \sum_m N(X^{+m})$, it is possible to derive the ionization ratio.

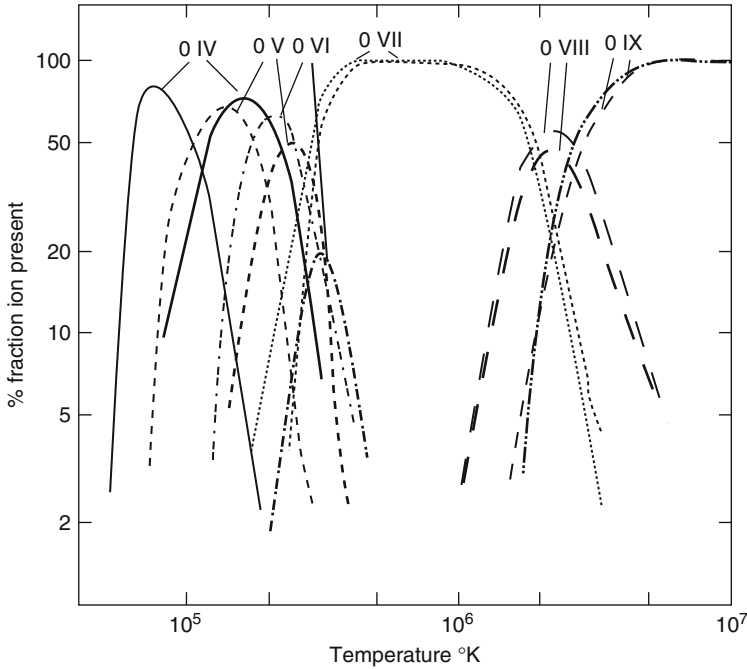
In the case of local thermodynamic equilibrium (LTE), if we write the detailed balance including photoionization and radiative recombination we obtain the Saha equation. At low densities, the plasma becomes optically thin and most of the radiation escapes, therefore processes like photoionization and radiative recombination are attenuated and the plasma is no longer in LTE.

If the timescales of the observed phenomena in the coronal plasma are longer than those for ionization and recombination, ($\frac{dN(X^{+m})}{dt} = 0$), the degree of ionization of an element is obtained by equating the ionization and recombination rates that relate successive ionization stages:

$$N(X^{+m})(q_{\text{col}} + q_{\text{au}} + q_{\text{ct}}) = N(X^{+m+1})(\alpha_{\text{r}} + \alpha_{\text{d}} + \alpha_{\text{ct}}) \quad (3.14)$$

The dominant processes in optically thin plasmas are *collisional ionization – direct ionization from the inner and outer shells* (q_{col}) and excitation followed by *autoionization* (q_{au}); *radiative recombination* (α_{r}) and *dielectronic recombination* (α_{d}); and *charge transfer* ($\alpha_{\text{ct}}, q_{\text{ct}}$).

The process of dielectronic recombination was shown by Burgess (1964, 1965), and Seaton (1964b) to be a very important effect for the solar corona.  [Figure 3-48](#) shows the effect that inclusion of dielectronic recombination has on the ion abundances. Dielectronic recombination occurs when a free electron is captured into an autoionization state of the recombining



■ Fig. 3-48

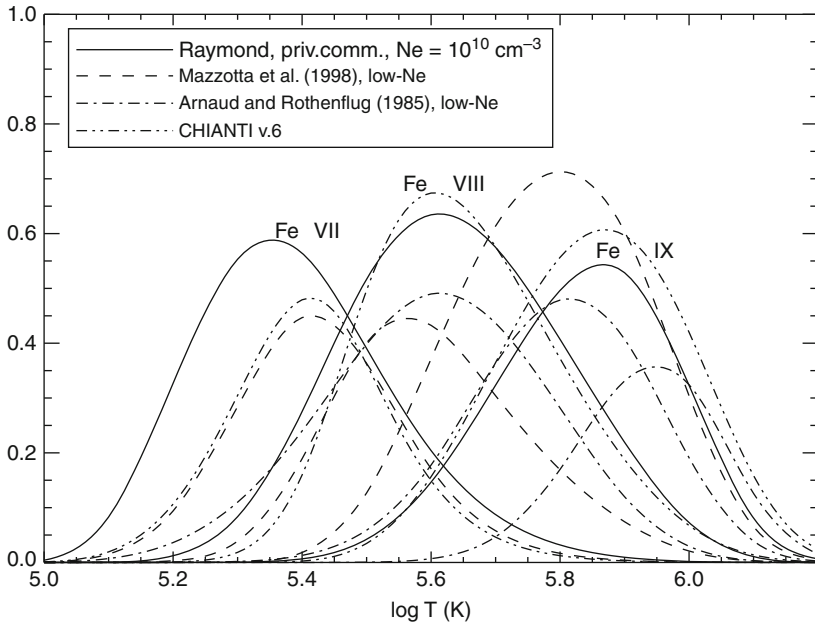
The effect that dielectronic recombination has on ion abundances (*thin lines* are calculated with-out), from Pottasch (1967)

ion, the ion can then autoionize (releasing again a free electron) or produce a radiative transition into a bound state of the recombined ion. The transition can only occur at specific wavelengths. There are many diagnostic applications using these satellite lines, which we cannot describe here. See, for example, Gabriel and Mason (1982), Phillips et al. (2008); and references therein. A significant number of recombination rates have been calculated by N.R.Badnell and collaborators.

Most ion abundances are calculated in the low-density limit, assuming that all the population in an ion is in the ground state. This is a good approximation for many ions, but not those which have metastable levels. The ion population slightly depends on the electron density through the rate coefficients, as shown by Burgess and Summers (1969). An example of how different ion abundances can be obtained using different rates is shown in ► Fig. 3-49.

6.5 Coronal Model Approximation: Two-Level Ion

In the low-density corona, radiative decay (spontaneous emission with Einstein coefficient A_{ji}) occurs much more often than collisional excitation processes, and, in general, one can neglect the population of higher excited states, j , relative to the ground state, g . Under this so-called *coronal-model approximation*, it is only the electron *collisional excitation* from the ground state



■ Fig. 3-49

The abundances of three iron ions as calculated in equilibrium using different sets of ionization/recombination rates

of an ion and the *spontaneous radiative decay* that are competing. Thus, the radiative emission rate may be inferred from the equilibrium between the excitation/de-excitation processes expressed by the following equation:

$$N_g N_e C_{g,j}^e = N_j A_{j,g} \quad (3.15)$$

If the coronal approximation breaks down, if for example A_{jg} is small (a forbidden or intersystem transition), then collisional de-excitation can compete with radiative decay as a depopulating mechanism.

6.6 Emission Measure Approximations

Following Pottasch (1963), many authors have approximated the above expression (● 3.5) by removing an averaged value of $G(T)$ from the integral:

$$I_{\text{th}} = A(X) \langle G(T) \rangle \int_h N_e N_H dh \quad (3.16)$$


A *line emission measure* EM_L can therefore be defined, for each observed line of intensity I_{ob} :

$$EM_L \equiv \frac{I_{\text{ob}}}{A(X) \langle G(T) \rangle} \quad [\text{cm}^{-5}] \quad (3.17)$$

where $\langle G(T) \rangle = 0.7G(T_{\max})$. The method assumes that each line is mainly formed at temperatures close to the peak value T_{\max} of its contribution function, $G(T_{\max})$, and produces plots of the *line emission measures* (multiplied by the corresponding abundance value)

$$A(X) \text{ EM}_L = \frac{I_{\text{ob}}}{0.7G(T_{\max})} \quad (3.18)$$

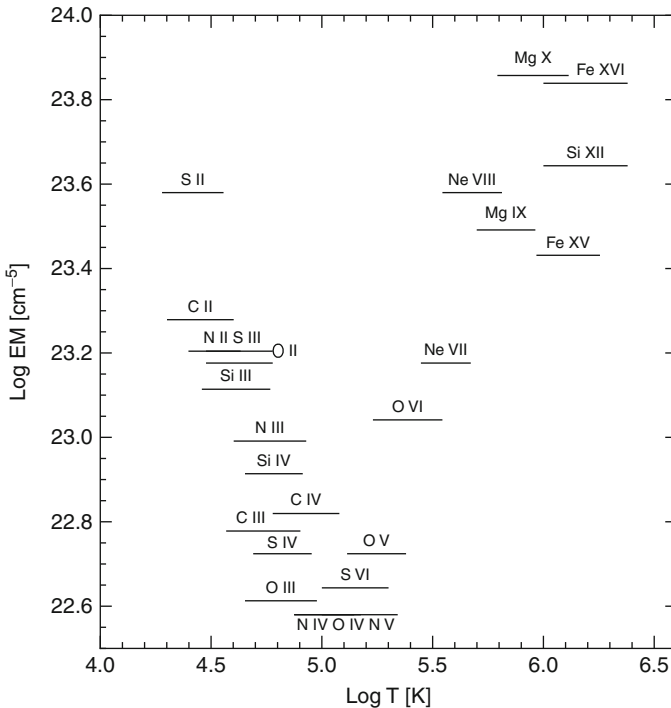
as a function of T_{\max} .


The method was developed to measure the relative abundances of elements contributing to the observed lines. The relative abundances of the elements are derived in order to have all the *line emission measures* of the various ions lie along a common smooth curve. One example is given in  Fig. 3-50, obtained from the original data as in Pottasch (1963).

Many other approximations and methods have been proposed. One approximation widely used and originally proposed by Widing and Feldman (1989) was to define a *line differential emission measure* DEM_L value:

$$\text{DEM}_L \equiv \left\langle N_e N_H \frac{dh}{dT} \right\rangle \quad [\text{cm}^{-5} \text{K}^{-1}] \quad (3.19)$$

and adjust the abundances $A(X)$ so that the $A(X) \text{ DEM}_L = I_{\text{ob}} / \int_T G(T) dT$ values form a smooth curve as a function of T_{\max} .

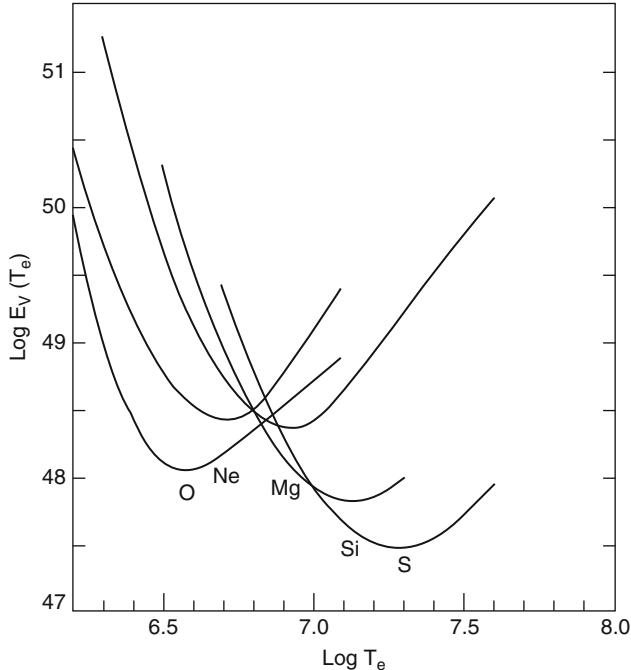


 Fig. 3-50

The line emission measure values obtained by Pottasch (1963) from irradiance measurements of the quiet Sun [values from the original paper]

The above methods are limited because of the assumption that the bulk of each line is formed at the T_{\max} temperature. This is broadly correct if the plasma is uniformly distributed in temperature, but if not, most of the intensity in each line could come from either lower or higher temperatures. Another problem is that many ions (e.g., He I-like, Li I-like) have broad contribution functions, so are naturally formed over large temperature ranges. The major problem, however, lies in the assumption that the plasma is uniformly distributed in temperature. There are many cases on the Sun (e.g., coronal loops, coronal hole plumes) where the distribution is actually nearly isothermal. In these cases, it has been shown by Del Zanna et al. (2001), Del Zanna (2003), and Del Zanna et al. (2003) that the method seriously overestimates the relative chemical abundances.

Another way to estimate the $EM(T)$ is the *Emission Measure Loci* method, by which the loci of the curves $I_{\text{ob}}/(A(X) \times G(T))$ as a function of temperature are considered. In fact, for each line and temperature T_* , the value $I_{\text{ob}}/(A(X) \times G(T_*))$ represents an upper limit to the value of the emission measure $EM(T_*)$ at that temperature, assuming that all the observed emission I_{ob} is produced by an isothermal plasma at the temperature T_* . The EM Loci method was first introduced by Strong (1978) and later applied by Veck et al. (1984) to the analysis of solar X-ray flare spectra (see ► Fig. 3-51) and by Del Zanna and Mason (2003) to solar active regions.

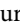


► Fig. 3-51
The EM Loci method used by Veck et al. (1984)

6.7 A Word of Warning: Problems with Emission Measures

The Li- and Na-like ions give rise to some of the strongest lines in the UV. However, it has long been known (see, e.g., Burton et al. 1971) that the emission measures for lines from ions of the Li- and Na-like isoelectronic sequences are at odds with those of the others. This fact has been largely neglected or underestimated in the literature.

Del Zanna (1999) reanalyzed Skylab data using up-to-date atomic data to show the extent of this anomalous behavior. Li-like N V and C IV are underestimated by factors of 3 and 10, while those of Ne VIII and Mg X are overestimated by factors of 5 and 10, respectively.

Del Zanna et al. (2002b) showed, for the first time, that the same problem occurs when stellar emission measures are considered (see  Fig. 3-52). This was only possible by combining UV observations from different instruments (FUSE, HST/STIS). All previous literature considered stellar observations at wavelengths where by far the brightest lines are those from Li- and Na-like ions (e.g., IUE and HST/STIS). As a consequence, results in previous literature should be revised.

6.8 Electron Density Determination

The electron (number) density can be defined as the ratio of the emission measure (EM) to the volume (V) of the emitting plasma: $N_e^2 = EM/V$. This approximation is reasonable under the assumption of plasma being distributed homogeneously throughout the emitting volume. To determine the electron density using this method, assumptions about the element abundance and ionization balance are also needed.

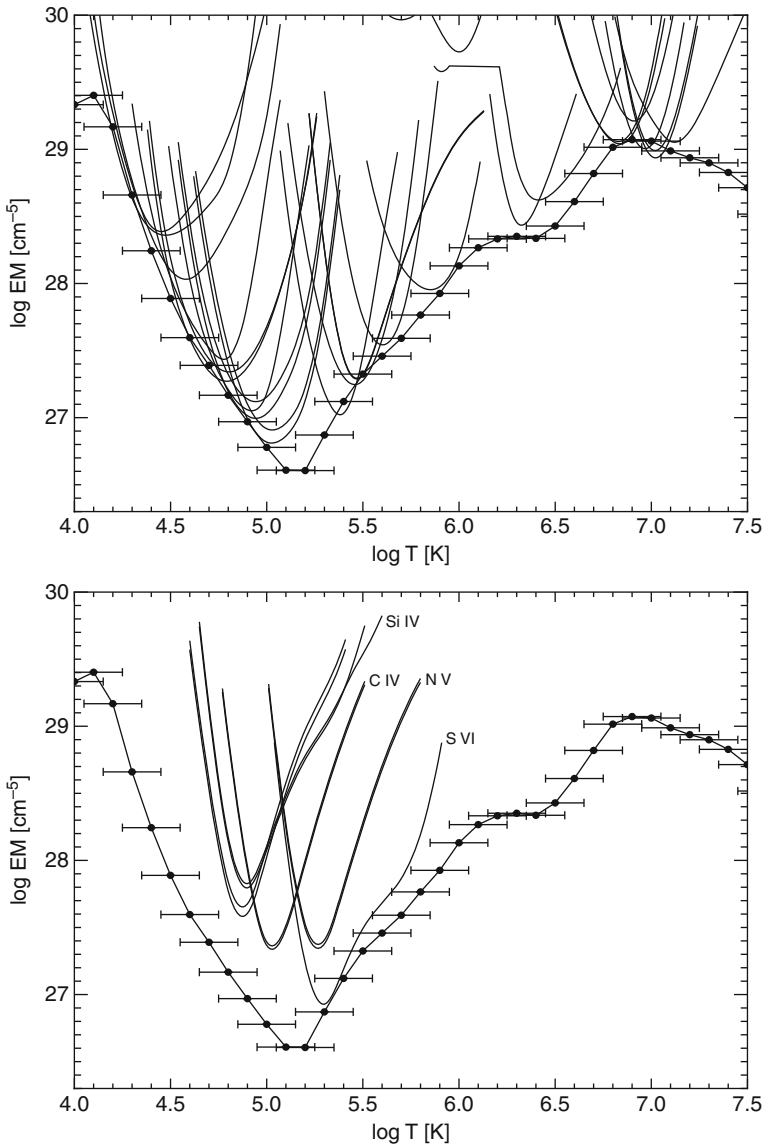
A more reliable diagnostic method for measuring density is the use of density-dependent line ratios from a single ion which has *metastable levels*. A metastable level, m , within an ion is defined as a level that has a small radiative decay rate, so that collisional de-excitation competes with radiative decay as a depopulating process. Metastable levels could for example be excited levels within the ground configuration which can only decay via forbidden transitions. The ion population is shifted from the ground level into the metastable(s) as the electron density of the plasma increases. Therefore, two lines principally excited from the ground and the metastable levels, respectively, have different dependencies on density.

For simplicity we again consider a two-level model. For forbidden and intersystem transitions the radiative decay rate is generally very small ($A_{m,g} \simeq 10^0 - 10^2 \text{ sec}^{-1}$), and collisional de-excitation then becomes an important depopulating mechanism ($A_{m,g} \simeq N_e C_{m,g}^e$) and may even be the dominant mechanism; moreover the population of the metastable level becomes comparable with the population of the ground level and we have:

$$N_m = \frac{N_g N_e C_{g,m}^e}{N_e C_{m,g}^e + A_{m,g}} \quad (3.20)$$

For small electron densities, $N_e \rightarrow 0$, $A_{m,g} \gg N_e C_{m,g}^e$, then the intensity has the same dependence on the density as an allowed line (I^A):

$$I_{m,g} \simeq N_e^2 \quad (3.21)$$



■ Fig. 3-52

The emission measure obtained by Del Zanna et al. (2002b) from irradiance measurements of the dMe star AU Mic. The *dots* indicate the emission measure calculated over a temperature interval $\Delta \log T = 0.3$. The *curves* are the $I_{\text{obs}} / (A(X) \times G(T))$ values, obtained from the FUSE, HST/STIS lines used for the emission measure calculation (*Top*) and from the lines of the “anomalous” ions, from the Li- and Na-like isoelectronic sequences (*Bottom*)

For very large values of the electron density, $N_e \rightarrow \infty$, the collisional depopulation dominates, $N_e C_{m,g}^e \gg A_{m,g}$; the metastable level is in Boltzmann equilibrium with the ground level:

$$\frac{N_m}{N_g} = \frac{C_{g,m}^e}{C_{m,g}^e} = \frac{\omega_m}{\omega_g} \exp\left(\frac{-\Delta E_{g,m}}{kT}\right) \quad (3.22)$$

And the line intensity has the form:

$$I_{m,g} \simeq N_e \quad (3.23)$$

For intermediate values of the electron density $A_{m,g} \simeq N_e C_{m,g}^e$, the population of the metastable level is significant and the intensity varies as

$$I_{m,g} \simeq N_e^\beta \quad 1 < \beta < 2 \quad (3.24)$$

The intensity ratio of a forbidden to an allowed transition (I^F/I^A) for different spectral lines from the same ion can be used to determine an average electron density for the emitting volume. This value is independent of the elemental abundance, ionization ratio, and any assumptions about the size of that volume.

If the population of a metastable level (m) is comparable with the ground level (g), then other excited levels (k) can be populated from this metastable level as well as from the ground level and the dependence of the intensity on electron density becomes

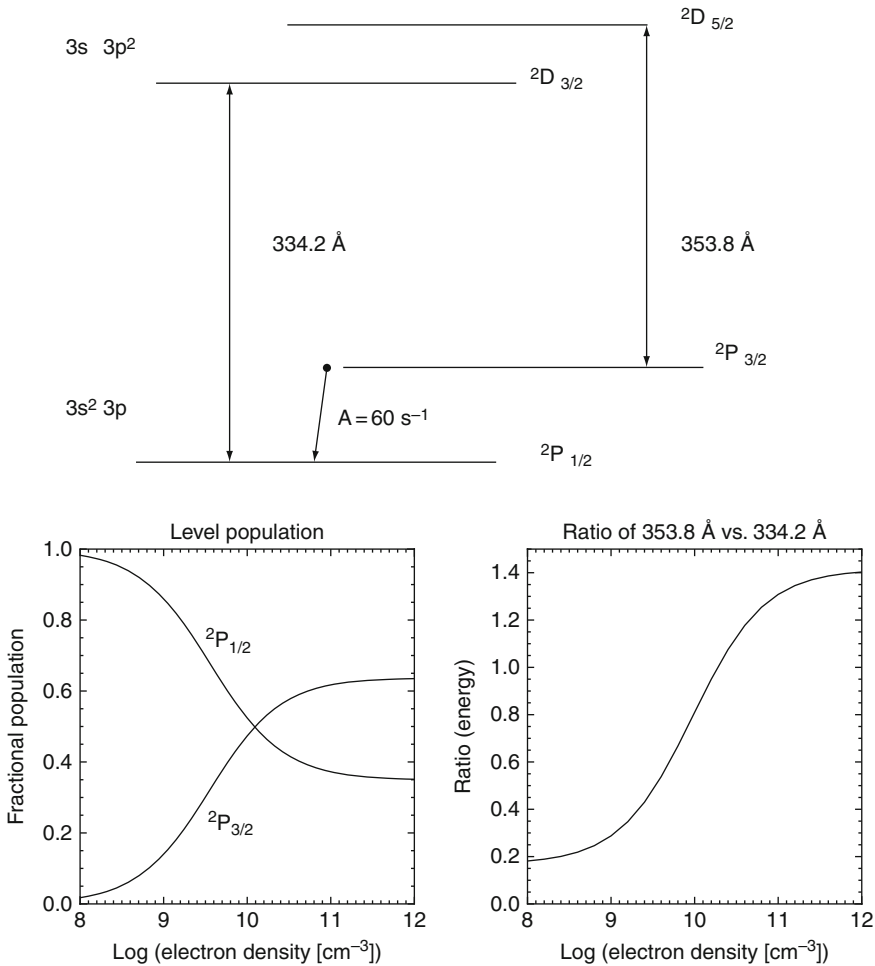
$$I_{k,m} \simeq N_e^\beta \quad 2 < \beta < 3 \quad (3.25)$$

Taking Fe XIV as an example (☉ Fig. 3-53), the ground configuration $3s^23p$ has two levels: $^2P_{1/2}$ and $^2P_{3/2}$; the transition between these two levels gives rise to the coronal green line at 5303 \AA . The metastable level is actually the upper level in the ground configuration ($3s^23p^2P_{3/2}$). Its transition probability to the ground level is in fact only 60 s^{-1} . For low electron densities (10^8 cm^{-3}), almost all the population for Fe XIV is in the ground level, but as electron density is increased (10^{10} cm^{-3}), the upper level begins to have a significant population as well. The spectral line at 334.2 \AA is excited from the ground level ($3s^23p^2P_{1/2}$), whereas the line at 353.8 \AA is excited from the upper level in the ground configuration ($3s^23p^2P_{3/2}$). The intensity ratio of these two lines (☉ Fig. 3-53) varies with electron density, reflecting the level population changes in the ground configuration. For active region observations, the [353.8/334.2] ratio gives electron densities varying from around 10^9 cm^{-3} in the quiet part to around $10^{10.5} \text{ cm}^{-3}$ in the core (Mason et al. 1999).

The CDS and SUMER instruments on board SoHO have provided a wide range of density diagnostics, but density measurements from these two instruments are generally only accurate to the 30–40% level at best. The high sensitivity of the EIS instrument on board Hinode now allows electron number density measurements to an unprecedented precision of up to 5% in active regions.

6.9 Spectroscopic Filling Factors

If one assumes a homogeneous slab of plasma of thickness dh , once elemental abundances are known, and a line intensity measured, one can obtain an average $EM_L = N_e^2 dh$ from



■ Fig. 3-53

Electron density sensitivity for a pair of Fe XIV lines

which the path length dh can be estimated once the electron density N_e is measured from, e.g., a line ratio. Dere et al. (1987) used HRTS transition region C IV intensities and densities from a line ratio of O IV (both formed at around 10^5 K) to obtain path lengths of 0.1–10 km, which was much smaller than the observed sizes of the spicular structures (2,400 km). This is often interpreted as due to the transition region having a filamentary structure, so that most of the plasma occupies only a small fraction (0.01–0.00001 – the filling factor) of the observed volume. However, translating the spectroscopic measurements into a geometrical filling factors is not straightforward (see, e.g., Judge 2000).

6.10 Electron Temperature Determination

One way to measure the electron temperature is to consider the intensity ratio of two allowed lines excited from the ground level, g having significantly different excitation energies.

The intensity ratio can be written as

$$\frac{I_{g,j}}{I_{g,k}} = \frac{\Delta E_{g,j} \Upsilon_{g,j}}{\Delta E_{g,k} \Upsilon_{g,k}} \exp \left[\frac{\Delta E_{g,k} - \Delta E_{g,j}}{k_B T} \right], \quad (3.26)$$

where j and k denote the excited levels; Υ is the thermally averaged collision strength, and k_B is the Boltzman constant. The ratio becomes sensitive to changes in the temperature if the thermal energy of the electrons is much smaller than the difference between the excitation energies

$$\frac{\Delta E_{g,k} - \Delta E_{g,j}}{k_B T} \gg 1 \quad (3.27)$$

assuming that the lines are emitted by the same isothermal volume with the same electron density.

Such spectral lines are normally far apart in wavelength and it is often necessary to use observations from different instruments, which can lead to inaccuracies (e.g., O VI 1032, 173 Å lines observed by SoHO SUMER and CDS/GIS). Be-like ions offer a good opportunity for diagnostics, as the ratios of the strong resonance and intercombination lines are good temperature indicators. Of all the Be-like ions, Mg IX is that one formed closest to the average coronal T (1 MK). The atomic structure of Be-like ions is such that the resonance line in second order is very close to the intercombination line. For Mg, the resonance 368.07 Å line has been routinely observed in second order by the SoHO/GIS close to the 706.06 Å intercombination line. The 368.07, 706.06, and 749.55 Å lines are basically density-insensitive but have a different temperature dependence. Therefore, any combination of two of these three lines is a good temperature diagnostic. The 706.06, and 749.55 Å lines have been observed with SUMER and used as a temperature diagnostic in coronal holes. Del Zanna et al. (2008) have calculated the atomic data for Mg IX, and revised previous electron temperature measurements.

6.11 Continuum

The continuum emission can be significant in the UV, but diminishes in the EUV. *Free-free* emission is produced when an electron interacts with a charged particle X^{+m+1} and makes a transition from an energy E to an energy E' releasing a photon of energy $h\nu$: $X^{+m+1} + e(E) \Rightarrow X^{+m+1} + e(E') + h\nu$ For a Maxwellian velocity distribution of electrons the process is called *thermal bremsstrahlung*. The formulation for the emitted energy per unit of time and volume is based on the mean Gaunt factors computed by Karzas and Latter (1961). Free-free emission is the main radiative loss mechanism for low-density plasmas at $T > 10^7$ K.

Free-bound emission is produced when a free electron of energy E is captured by an ion (X^{+m+1}) into a bound state of X^{+m} :



a photon of energy $h\nu = E + I_n$ is emitted and I_n is the ionization energy of the bound state n . For a Maxwellian electron velocity distribution, the continuum emission is characterized by discontinuities at the ionization thresholds. The process is called *radiative recombination*. The free-bound emission depends on the chemical abundances.

For hydrogen and helium-like ions, another continuum (*two-photon*) is important, in particular at $T \leq 3 \cdot 10^4$ K. The metastable 2s state of hydrogenic and helium-like ions depopulates via collisional excitation to the 2p level and by the two-photon decay process.

6.12 Line Widths, Ion Temperatures, and Doppler Motions

Spectral line profiles give information about the dynamic nature of the solar and stellar atmospheres. The Dopplershift $\Delta\lambda$ in a spectral line is directly proportional to the line-of-sight velocity v of the plasma element emitting the line: $\Delta\lambda/\lambda = v/c$, where c is the speed of light. A blueshift indicates plasma moving toward the observer. Naturally, different plasma velocities along the line of sight can be present. These would modify the line profile from the simple thermal broadening of the line.

An emission line has a natural width (called the thermal width) that is characteristic of the temperature of formation of the emitting ion and is due to the Doppler motions of the emitting ions. An additional broadening is also introduced by the observing instrument and depends on the quality and alignment of the optical components. If a line width is found to be broader than the combined thermal and instrumental widths, then we refer to the additional component as the non-thermal width. The line width of an optically thin spectral line has a Gaussian profile and is expressed mathematically in terms of three components.

The intensity per unit wavelength I_λ is defined as

$$I_\lambda = \frac{I}{\sqrt{2\pi}\sigma} \exp[-(\lambda - \lambda_0)^2/2\sigma^2] \quad (3.29)$$

where $I = \int I_\lambda d\lambda$ is the integrated intensity and σ is the Gaussian width given by

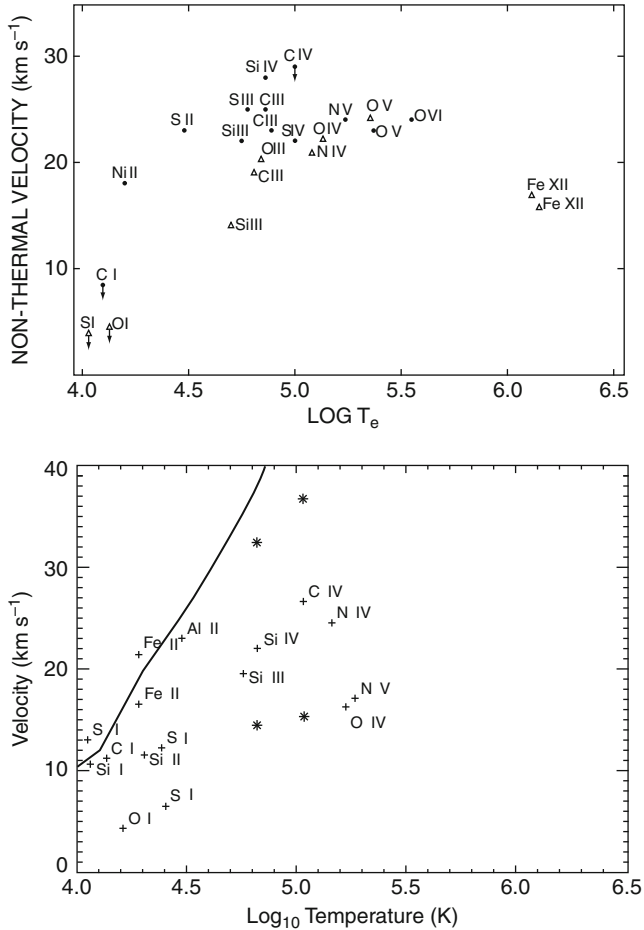
$$\sigma^2 = \frac{\lambda^2}{2c^2} \left(\frac{2kT_i}{M} + \xi^2 \right) + \sigma_I^2 \quad (3.30)$$

for a Maxwellian velocity distribution for the ion emitting the line at a temperature T_i . Here M is the ion mass, σ_I is the Gaussian instrumental width, and ξ is the most probable nonthermal velocity ntv . Nonthermal velocities can be obtained by assuming that T_i is the temperature corresponding to peak abundance of the ion (see [Fig. 3-54](#)). Conversely, if assumptions are made on the nonthermal velocities, the ion temperature T_i can be obtained.

Several coronagraph experiments (e.g., Spartan, SoHO/UVCS) have provided information on hydrogen atom and electron temperatures from H I Ly α profiles (see, e.g., the review of Kohl et al. 2006). The spectral line profiles, at the distances observed by these instruments, have two components. The resonantly scattered, relatively narrow component provides empirical constraints on the electron and proton temperatures. The weaker, electron scattered component is wider and related to the electron density and temperature.

6.13 The CHIANTI Atomic Package

Quantitative modeling of the EUV and soft X-ray plasma emission provides a powerful temperature and density diagnostic of the coronal plasma. However, to calculate optically-thin synthetic spectra and to apply spectral analysis and plasma diagnostics to solar EUV and soft X-ray emission, data from thousands of atomic energy levels are required. For this purpose, the CHIANTI atomic database (Dere et al. 1997), which was first released in 1996, provides a comprehensive dataset covering the UV and X-ray wavelength ranges. The database contains state-of-the-art energy levels, radiative data, and electron and proton collisional data for the majority of astrophysical ions of interest. Furthermore, the CHIANTI codes represent a diagnostics toolbox for astrophysical and solar plasmas. In CHIANTI, the atomic data (energy levels,



■ Fig. 3-54

Nonthermal velocities in the quiet Sun obtained from Skylab (Kjeldseth Moe and Nicolas 1977) and HRTS (Dere and Mason 1993)

wavelengths, radiative transition probabilities and excitation data) are stored in ASCII files. The wavelengths are based on experimental data. Lines for which only theoretical energy levels are available are also provided. The radiative data are taken from published literature and, where necessary, supplemented by new calculations. CHIANTI also includes ancillary data such as standard differential emission measures, elemental abundance, and ionization fraction files.

In the CHIANTI database, the assumption of Maxwellian electron distributions is implicit through the storage of Maxwellian-averaged electron collision strengths. However, recent observations of the small-scale transient solar activity have shown that the solar atmosphere is dynamic and nonthermal (e.g., Dzifčáková et al. 2008). Therefore, to progress our knowledge of the solar atmospheric activity, nonequilibrium and nonthermal spectral plasma emission models are required in the future.

6.14 Benchmarking the Atomic Data

Ongoing work has been carried out to benchmark the atomic data against observations. A large part of the work is done as part of the assessment for each CHIANTI release.

The atomic data, identifications, and diagnostics from the X-rays to the visible for the most important lines on an ion by ion basis have been assessed against laboratory and astrophysical observations in a series of papers published in *Astronomy and Astrophysics*. The assessments include atomic calculations and provide the most accurate identifications to date. The first paper in the series is on Fe x (Del Zanna et al. 2004).

7 Chemical Abundances

An accurate knowledge of the chemical composition of the Sun is of paramount importance for a variety of reasons, the most important one being to obtain an accurate model of the Sun as a Star (the standard model). Chemical abundances have been measured in a variety of ways, from samples of meteoritic materials, to remote-sensing of the photospheric (visible) and coronal (XUV) emission of the Sun, to helioseismology and to in situ measurements of the solar wind and of the solar energetic particles (SEP). Gamma-ray spectroscopy is another powerful tool for measuring the abundances of various elements, as described in the review from Ramaty and Murphy (1987). The drawback is that very few observations of strong flares which produce gamma-rays are available. One was observed on April 27, 1981, and a few have been observed more recently with RHESSI.

The photospheric and coronal abundances of many elements are still uncertain, because they depend critically on the spectral resolution, the method adopted, and the accuracy of atomic physics calculations. Some useful review articles on elemental abundances are Anders and Grevesse (1989), Meyer (1985), Bochsler (2007), Asplund et al. (2009), Lodders et al. (2009). Various review articles can also be found in Wimmer-Schweingruber (2001), the proceedings of a joint SoHO/ACE workshop on solar and galactic composition in 2001.

Elemental abundances, A , are normally provided as number densities relative to hydrogen (often as $\log_{10}(\text{dex})$, i.e., assuming $\log_{10}(A(H)) = 12$). In terms of number densities, the Sun and its neighborhood are composed primarily (90%) of hydrogen, with significant (10%) helium, but with only about 0.1% of the remaining elements. Abundances of Li, Be, and B are very low. The Li abundance is an interesting proxy for estimating the age of a star.

J. von Fraunhofer (1787–1826) was the first to observe the dark lines in the visible spectrum of the Sun. G. Kirchhoff (1824–1887) correctly proposed that these were due to absorption of light by cooler, overlying layers of the solar atmosphere. Russell (1929) produced a pioneering piece of work, establishing the photospheric abundances of a large number of elements from the visible spectrum of the Sun.

Goldschmidt (1938) compiled chemical data for terrestrial rocks and meteorites in a pioneering piece of work. Along with others, he suggested that the abundances of non-volatile elements in the CI carbonaceous chondrites meteorites should be representative of the average values for our solar system. Among the many types of meteorites, the CI carbonaceous chondrites (CC) are thought to originate from asteroids which were formed at the same time as the rest of the planets in the solar system, but that were not subject to the many changes which occurred during the evolution. Indeed, there is a remarkable agreement between CC

and the most up-to-date photospheric abundances of non-volatile elements. A recent review on abundances in chondritic meteorites is given by Lodders et al. (2009).

The solar (photospheric) abundances of non-volatile elements such as Mg, Si, Ca, Fe, Ni, can be established from the absorption lines in the visible spectrum, or obtained from meteoritic samples. The abundances of volatile elements such as H, C, N, O can in principle also be obtained from photospheric spectra, but not from meteoritic samples because they are not fully retained. The abundances of the important noble gases He, Ne, Ar cannot be obtained either way, in the first instance because these elements do not produce usable absorption lines, and in the second case because they are volatile elements.

Detailed examination of the Sun's upper atmosphere reveals that elemental abundances vary from the photospheric values between different solar regions. In addition, measurements of the solar wind composition differ from photospheric values. There is a correlation between the abundance and the first ionization potential (FIP) of the different elements. In particular, the low-FIP (≤ 10 eV) elements are more abundant than high-FIP in the slow solar wind (SSW) and in coronal loop plasma.

7.1 Photospheric Abundances

Many semiempirical 1D models adopting LTE have been developed to study the photosphere. Sophisticated model atmospheres include departures from LTE and, in general, comparisons between observed high-resolution spectra and theoretical ones are very satisfactory.

In recent years, it has become possible to perform 3D time-dependent hydrodynamic simulations of solar convection, where the hydrodynamic equations are solved together with 3D radiative transfer equations (for a review see Nordlund et al. 2009). The calculations are carried out adopting a limited set of opacities when computing the radiative heating/cooling rate in the energy equation. These models successfully reproduce the main features of the solar granulation, in terms of spatial, temporal, and velocity scales. These new models produce significantly lower abundances of carbon, nitrogen, and oxygen, compared with the widely used earlier values.

Oxygen is the most abundant element after H and He. The derived “photospheric” abundance of oxygen has changed from $10^{8.93}$ (Anders and Grevesse 1989) to $10^{8.69}$ (Asplund et al. 2009). The latest result is based on the analysis of forbidden and permitted O I transitions as well as vibration–rotation and pure rotation lines of OH. Various discrepancies that have been present for a long time appear to have been resolved, once severe blending and the new simulations are taken into account.

An up-to-date review on photospheric abundances is given by Asplund et al. (2009), where references to recent work can be found. There is still a debate in the literature about the accuracy of these new abundances. If confirmed, they have far-reaching implications in a variety of fields. As most previous measurements have been carried out *relative* to oxygen, for example, a large part of literature may need to be revised. The revised abundances have important implications for the *standard solar model*, as discussed for example by Basu and Antia (2008).

7.2 Coronal Abundances

For a review of some of the uncertainties related to abundance determinations derived from UV and X-ray spectra, see Mason (1995). A vast literature exists on abundance measurements

using various techniques from the Skylab, Yohkoh, and SMM missions. Only some examples are given here. Pottasch (1963) applied an approximate method (see [▶ Sect. 6.6](#)) to show that the abundances in the solar corona are different from those of the photosphere. Walker et al. (1974) used the intensities of resonance lines of hydrogen-like and He-like ions in the X-rays to obtain relative chemical abundances for a number of elements. Interestingly, for the active regions and flares that they studied, they found near-photospheric abundances.

An extensive literature based on Skylab EUV observations exists. For example, Widing and Feldman (2001) used Skylab spectroheliographs and measured the rate of change of the radiance ratios of Mg/Ne lines of active regions as they evolved with time, as a proxy for the FIP effect. Interestingly, at birth of an active region, they measured ‘photospheric’ composition, while after 2–3 days after the emergence of the active region, the relative abundance changes by factors of 4–5. However, most results from Skylab need to be revisited, since the Widing and Feldman (1989) approximation (see [▶ Sect. 6.6](#)) which was used extensively may have some limitations. This approximation tends to overestimate the FIP effect when the plasma distribution is not multi-thermal, as is the case of active region loops (as discussed in Del Zanna 2003). For example, the EM Loci method, applied to a Skylab observation, was shown by Del Zanna (2003) to be consistent with an FIP bias of 3.7, rather than a large FIP bias of 14 obtained previously.

Some results based on EUV SoHO CDS spectra exist, and tend to indicate that the Mg/Ne abundances in quiescent 1 MK loops have near-photospheric abundances (cf. [▶ Fig. 3-59](#) and Del Zanna 2003; Del Zanna and Mason 2003). On the other hand, Young and Mason (1997) studied the Mg/Ne abundance ratio in an active region and found that emerging flux regions had photospheric abundances in contrast to longer-lived active region loops which showed a large FIP bias.

UV measurements in the outer corona have been obtained by SoHO UVCS. Raymond et al. (1997) analyzed SoHO UVCS spectra where lines from hydrogen and other elements were observed at a radial distance $R = 1.5 R_{\odot}$. In the core of a quiescent equatorial streamer during solar minimum, high-FIP elements were found to be depleted by an order of magnitude (compared with photospheric abundances), while low-FIP were also depleted by about a factor of 3. Along the edges of a quiescent streamer, and in a streamer associated with an active region, high-FIP elements were found to be depleted by a factor of 3. The abundances along the edges of the streamer legs were similar to those measured in the slow solar wind, which would be an important indication that these are the source regions for the slow wind. Different streamers observed when the Sun was more active, however, have shown different abundances and much reduced depletion.

Feldman et al. (1998) report an analysis of SoHO SUMER spectra very close to the solar limb, at a radial distance $R \leq 1.03 R_{\odot}$ in a quiet Sun region and above the north polar coronal hole. Low-FIP elements were found to be enriched by about a factor of 4 in the corona above the quiet equatorial region, but not in the coronal hole. One significant problem is that *the Ne VIII, Na IX, Mg X lines, all of which belong to the Li-like isoelectronic sequence, appear to indicate a systematic lower effective FIP bias value than the rest of the lines.* The authors used the O VI 1032 Å to normalize all the other lines, and since O VI is also in the same isoelectronic sequence, the results are quite uncertain. The same issue applies to the interpretation of SoHO UVCS spectra, and is related to the problem of anomalous ions in emission measure analyses (see [▶ Sect. 6.7](#)).

Various spectral measurements in the EUV and UV from the SoHO CDS UVCS and SUMER instruments as a function of height from the solar limb have now indicated the presence of gravitational settling in the sense that emission lines from elements with larger atomic weights such as Fe have radiances which decrease much rapidly than lines which should be formed at similar temperatures but are from lighter elements (e.g., Mg, Si). Feldman et al. (1998)

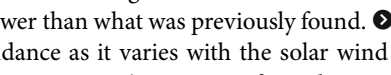
found evidence of gravitational settling and suggested that the Raymond et al. (1997) results may just be caused by gravitational settling. This is reasonable, if the streamer core is formed of quiescent closed structures so gravitational settling acts in reducing the abundances of the heavier elements, a fact that is not yet well established.

7.3 Abundances from In Situ Measurements

In situ chemical composition measurements are now available for over 25 years, from foil collections during the Apollo missions (and Genesis), to mass spectrometers such as the Solar Wind Ion Composition Spectrometer (SWICS) on Ulysses and CELIAS on SoHO, and more recently from the ACE and the STEREO missions.

In situ observations of the SW and of solar energetic particle (SEP) have shown that elemental abundances are highly variable. SEP events are transient and are now known to be associated with acceleration processes within CME-driven shocks and flares. SEP events are extremely variable and are therefore not suitable for determining the bulk of the solar composition. See Reames (1999) for a review of the characteristics of SEP events.

For many years, in situ measurements have indicated a FIP effect of about 4–5 in the slow SW, while the fast SW does not seem to have a significant FIP effect (as shown e.g., by Ulysses observations of a proxy, the Mg/O ratio). In the slow and fast SW, the He abundance is very variable but on average it is 2–3 times lower than the photospheric value.

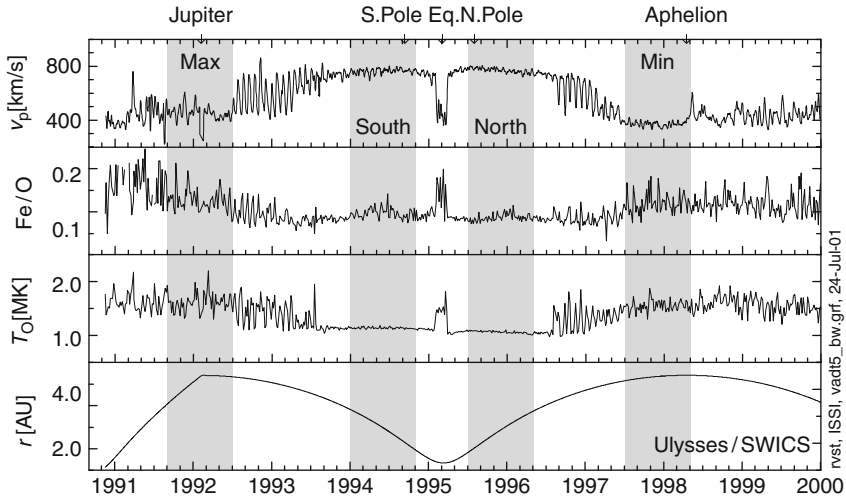
von Steiger et al. (2000) adopted an improved analysis technique to measure the average solar wind charge state and chemical composition of about 40 ion species of He, C, N, O, Ne, Mg, Si, S, and Fe observed with the SWICS on Ulysses. The FIP effect was confirmed, however it was found that on average the differences between slow and fast SW were only about a factor of 3, much lower than what was previously found.  *Figure 3-55* shows as an example the Fe/O relative abundance as it varies with the solar wind speed. It is evident that during the polar passes at solar minimum (1994, 1996, fast solar wind), the variability is much reduced and the relative abundance of Fe/O is lower.

Genesis was a NASA mission devoted to the collection of solar wind data at L1 from December 2001 to April 2004. Initial results show results consistent with other measurements. Accurate values, in particular for isotopic composition, should soon be available.

7.4 Depletion, Enhancement or Both?

It is still unclear whether the low-FIP elements such as Fe are *enhanced* in the corona, or high-FIP ones such as O are *depleted*, relative to their photospheric values, or if a “hybrid” solution such as that one proposed by Fludra and Schmelz (1999) applies.

Veck and Parkinson (1981) were the first to measure elemental abundances from line-to-continuum X-ray measurements from OSO-8. They found that the low-FIP elements seem to have photospheric values, and that high-FIP elements seem to be *depleted*. Since then, a large body of conflicting evidence on the subject has been presented. However, most direct remote-sensing measurements seem to confirm the early results from Veck and Parkinson (1981). For example, Fludra and Schmelz (1995) applied a *DEM* and line-to-continuum analysis on flare observations with the SMM Bent Crystal Spectrometer, and found high-FIP elements *depleted*, compared with their photospheric values. Direct measurements of inner-shell Fe lines formed during large solar flares by fluorescence of X-rays exciting photospheric iron, observed



■ Fig. 3-55

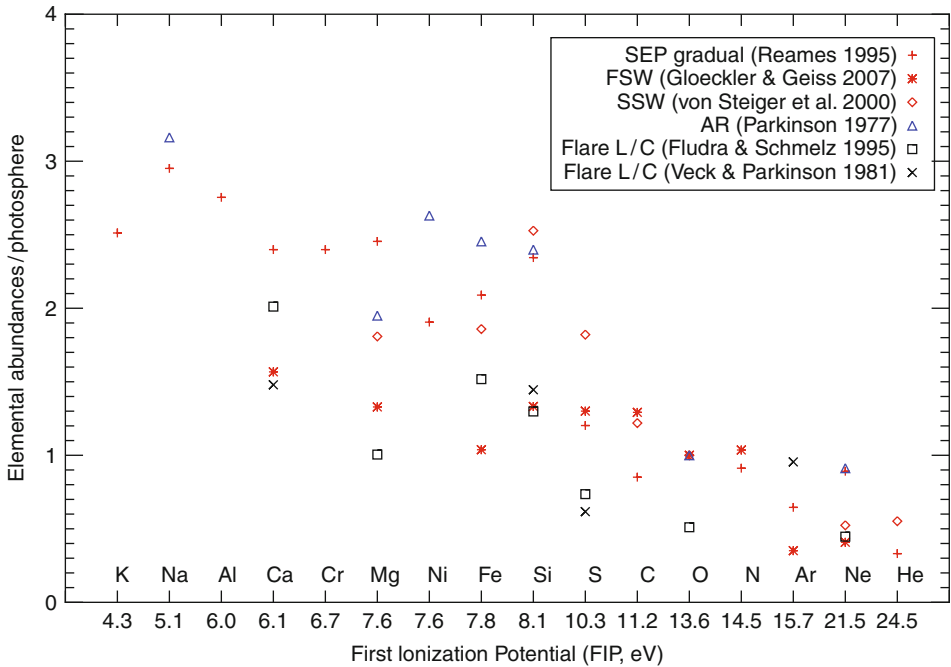
Results from the Solar Wind Ion Composition Spectrometer on Ulysses. From top to bottom: proton velocity, Fe/O relative abundance, freezing-in temperature, and distance of the spacecraft from the Sun. (Figure courtesy of R. von Steiger)

with various crystal spectrometers on Yohkoh, SMM, and P78-1 are consistent with the coronal Fe abundance being equal to the photospheric value, within a factor of 2 (Phillips et al. 1995). The RESIK crystal spectrometer on board the CORONAS-F spacecraft has also allowed line-to-continuum analyses of solar flares in the X-rays. For example, Chifor et al. (2007) found near-photospheric abundances for K, Si, and Ar and S abundances consistent with older measurements from SMM.

► Figure 3-56 shows a sample of a few abundance measurements, some in situ (in red), and some from remote sensing. For the in situ, we show measurements of Solar Energetic Particles (SEP) gradual events, which are thought to be associated with ejecta from the solar corona. We also show two average Ulysses solar wind measurements, one from the fast solar wind (FSW) from Gloeckler and Geiss (2007), and one from the slow solar wind (SSW) during maximum (von Steiger et al. 2000). All these in situ measurements were relative ones, and are plotted here taking the Oxygen abundance as a reference. The Figure also shows two measurements from X-ray observations of active regions (AR), again rescaled to the Oxygen abundance. Finally, we have added two sets of “absolute” abundances obtained from X-ray spectra of flares, and a line-to-continuum (L/C) analysis. All the measurements are plotted as a ratio relative to the “photospheric” abundances of Asplund et al. (2009). There is a clear trend for low-FIP elements to be overabundant and for high-FIP ones to be underabundant; however the scatter, mostly due to real solar variability, is large.

7.5 Helium, Neon, and Argon

Helium chromospheric lines were observed by Sir Norman Lockyer during a solar eclipse in the nineteenth century, at a time when the element was still unknown. After H, neutral and ionized



■ Fig. 3-56

Plot of coronal/photospheric elemental abundances as a function of element, ordered by the first ionization potential. In situ measurements (in red), remote sensing measurements (in blue and black)

He lines are the strongest lines in the XUV. The Coronal Helium Abundance Spacelab Experiment (CHASE) on the Spacelab 2 Mission was specifically designed to determine the helium abundance from the ratio of the scattered He II 304 Å to Lyman- α 1218 Å, on the disk and off the limb. A value for the He/H abundance of $7.0 \pm 1\%$ for the quiet corona was deduced by Gabriel et al. (1995).

Helium abundance measurements have also been indirectly obtained from helioseismology. A variety of measurements exist in the literature. For example, Basu and Antia (2004) obtained a value of 10.93 dex, equivalent to 8.5% by number, using OPAL opacities. This is close to the value of 8.3% predicted from standard Big Bang nucleosynthesis theory.

The modeling for all He lines needs detailed radiative transfer calculations, taking into account many effects, such as photon scattering, or the so-called photoionization-recombination mechanism, whereby coronal radiation can be a significant source of photoionization for neutral helium. Another complexity relates to the fact that all He lines have high excitation energies, which makes them very sensitive to non-thermal electron velocity distributions and other non-equilibrium effects. For a discussion of some of these effects, see e.g., Andretta et al. (2003), Jordan et al. (2005). In general, the EUV radiances in quiet Sun for all He lines are much stronger than realistic models predict.

Andretta et al. (2008) devised a new technique which involved modeling and observations from SoHO instruments of a C-class flare to obtain the first accurate measurement of the He abundance in the chromosphere, $7.5 \pm 1\%$, a value in marginal agreement with the helioseismic value.

In situ measurements of the relative abundance of helium to hydrogen show a very low abundance, less than 5%, with a large variability which is partly correlated with the solar wind speed and partly with the solar activity and cycle.

Neon and argon photospheric abundances are not directly measured, but have been inferred relative to oxygen or other elements from XUV spectra. They are also measured in situ. Gloeckler and Geiss (2007) suggest that Ulysses SW observations of Ne and Ar can be used to provide reliable “photospheric” abundances. They suggest a Ne/O abundance of 0.078 and an Ar/O one of 0.0018.

7.6 Modeling

The presence of an FIP effect implies an ion-neutral fractionation, which probably takes place low down in the solar atmosphere, possibly in the chromosphere at $T \leq 10^4$ K, where the ions start to become ionized. The ionization is mainly by the coronal EUV photons, but the low-FIP elements are more easily ionized by electron collisions. It was proposed some time ago (see, e.g., Geiss 1982) that once the fractionation has taken place in the chromosphere, the ions then drift up into the corona, guided by the magnetic field, to become ions of higher stages. The amount of the FIP effect would depend on how ions drift up into the corona, hence on the topology of the magnetic field. The key factor is the Coulomb drag of the ions with the protons. Low-FIP elements are more easily ionized and have a stronger coupling with the proton flow.

The issue is complex, and there are various physical processes at work that need to be studied in detail. On the one hand there are the ionizing/recombining processes. In the chromosphere, the H I L_α is by far the strongest contributor to ionizing UV photons, and is able to ionize all neutrals from elements with FIP ≤ 13.6 eV. Then, there are the collisions between all the particles, which produce charge exchange and diffusion, for example. In addition, gravitational settling is also present. In hydrostatic equilibrium, each ion is distributed in the corona with a pressure scale height which is proportional to its mass. Heavier ions tend to accumulate at lower heights, unless mixing due to e.g., flows is present.

Thermal diffusion is also strong for ions (see, e.g., Geiss and Buergi 1986), and occurs in the presence of a steep temperature gradient. This drags ions of heavier elements toward higher temperatures. In the transition region, temperature gradients are large and positive, and thermal diffusion acts in the opposite direction to gravitational settling.

Many models, based on first principles, have been proposed. Various authors followed von Steiger and Geiss (1989) by assuming that diffusion processes in the upper chromosphere are the main factors. Recently, Laming (2004) have presented an unified picture of the FIP and inverse FIP effects based on the action of the ponderomotive force of Alfvén waves in the chromosphere. The model simulations reproduce some of the main observational features (i.e., overabundance of low-FIP and underabundance of high-FIP), which is very encouraging.

7.7 Stellar and Galactic Abundances

The solar metallicity is quite typical when compared to nearby stars of similar spectral type (G). Accurate measurements have recently been obtained as a by-product of the search of extrasolar planets. It turns out that the majority of planet-bearing stars are metal-rich by 0.1–0.3 dex compared to the Sun, which in turn is metal-rich by about 0.2 dex compared to stars with no

planets (see, e.g., Butler et al. 2000). A recent compilation from Fuhrmann (2008) of nearby stars (within 25 pc) confirms that the Sun has an average metallicity.

When chemical abundances within our Galaxy are studied, a large scatter is normally found, but also an overall gradient, as a function of galactocentric distance. The latest measurements indicate that the Sun has quite typical photospheric abundances. This can be seen e.g., in Hou et al. (2000), with recently compiled chemical abundances obtained from H II regions, planetary nebulae, and B stars.

In contrast, the situation regarding stellar coronae is not clear. Some early measurements from the EUVE satellites provided chemical abundances for a few stars which showed a solar-like FIP effect (see, e.g. Drake et al. 1997), but it has only been since the launch of the *XMM-Newton*, *Chandra* satellites in 1999 that systematic measurements in the X-rays have been obtained. Some line-to-continuum measurements have been obtained, however in the majority of cases simple emission measure analyses have provided relative abundances between low-FIP elements (mainly iron) and high-FIP ones (mainly oxygen, neon). A complex picture has emerged, with many active stars and binaries showing an *inverse FIP effect*, with low-FIP elements being a lot more depleted than the high-FIP ones (both compared to hydrogen). This effect becomes more prominent with increasing activity of the star (see, e.g., Güdel and Nazé 2009 and references therein). These results have been puzzling, however some caveats apply. First, measurements of photospheric abundances have often been lacking, due to the strong stellar rotation which broadens the spectral lines. It is often assumed that stars have the same photospheric composition as the Sun. In only a few cases the inverse FIP effect seems to be confirmed. Second, the emission measure methods provide meaningful results only if the emission in lines emitted by different ions/elements is co-spatial, something very difficult to ascertain. Third, density effects and departures from ionization equilibrium may play a role.

8 The Solar Corona

8.1 Solar Features as Seen in X-rays and EUV

The most dramatic change in our perception of the solar atmosphere in the past few decades is due to X-ray and EUV observations from space. It is now evident how dynamic and active the solar atmosphere is, both on small and large temporal and spatial scales. Early concepts of relatively uniform, plane parallel models for the solar atmosphere are no longer sustainable. The structured and dynamic nature of the solar corona was first evident from the Skylab X-ray telescope observations. Spectacular observations were then made over an extended period with YOHKOH/SXT, showing dramatic changes from solar minimum to solar maximum, later shown in more detail with SoHO EIT and CDS observations (see [◆ Sect. 11.3.1](#)).

The SoHO/EIT observations showed the dynamic nature of the solar corona in the EUV, while the SoHO/MDI observations showed changes in the photospheric magnetic field over short timescales, even in the quiet Sun regions. TRACE has provided some stunning EUV images and movies of solar features, especially active regions.


When viewed in X-ray emission ([◆ Fig. 3-6](#)) the structures on the Sun can clearly be divided into different characteristics. Coronal hole areas are dark with quite well-defined boundaries. This occurs because the averaged density is about half the density of the averaged quiet regions, and because there is hardly any plasma at temperatures above 1 MK (see, e.g.,

results from SoHO CDS: Del Zanna and Bromage 1999). During solar minimum coronal holes are apparent at the north and south poles, but during solar maximum, coronal holes frequently extend down to lower latitudes. Coronal holes represent areas in the solar atmosphere where the magnetic field is predominantly unipolar and is “open”, that is goes out into the heliosphere. The fast coronal wind flows from these regions. Coronal holes contain sub-features, long plumes of bright emission, bright points (small bipolar regions), and dynamic jets.

The quiet sun is the more diffuse area of weak X-ray emission. On closer inspection, even the quiet sun regions are covered by a multitude of small transient brightening (and small bipolar regions), due to the constant motion of the photospheric footpoints of the magnetic field. Other solar features include prominences, seen in the quiet Sun and active regions. These can sometimes erupt and can be associated with Coronal Mass Ejections (CMEs) which shoot out from the Sun.

In this section we discuss the characteristics and properties of the solar corona, in particular with regard to active regions. We pay particular regard to the measurements of plasma properties: temperature, electron density, flows etc, which are an essential requirement to constrain heating models.

8.2 Solar Active Regions

Solar active regions (ARs) are areas of enhanced UV and X-ray emission that lie directly above areas of enhanced magnetic field, sometimes with associated sunspots. The heliographic position of active regions is typically confined within latitudes of $\pm 40^\circ$ from the solar equator, as is the case of the sunspots. ARs typically exhibit a strongly concentrated leading magnetic polarity, followed by a more fragmented trailing group of opposite polarity. Because of this bipolar nature, active regions are mainly made up of closed magnetic field lines. Due to continuous magnetic flux emergence, and reconfiguration, a number of dynamic processes such as plasma heating, flares, and coronal mass ejections occur in active regions. Active regions have the familiar appearance of numerous filled loops, which are hotter and denser than the background corona, producing bright emission in soft X-rays and EUV wavelengths (see  Fig. 3-6). It is normally accepted that loops trace out the magnetic field structure in the corona.

The Monograph from the Skylab Workshop III on Solar Active Regions (Orrall 1981) is a good starting point for the study of solar active regions. In particular, the S082A instrument provided some good observations of active regions and flares. The S082A observations indicated that the *hot core loops* (seen e.g., in Fe xvi and X-rays) were mostly low lying, compact and closely packed (unresolved). They seemed to connect across the magnetic neutral line. The cooler *warm loops* (seen in Ne vii) seemed better defined, were larger and slender. There were also many bright patches of emission or *kernels* in strong magnetic regions on either side of the neutral line (corresponding to the bright chromospheric plage areas). These kernels could be identified as the footpoints of the Fe xvi and X-ray loops. Dere and Mason (1981) provided a summary of electron density values derived for active regions, which ranged from $0.7\text{--}6.0 \times 10^9 \text{ cm}^{-3}$ for a temperature range of 1.2–2 MK.

After Skylab, the YOHKOH/SXT instrument was widely used to study the plasma properties of active regions and solar flares, as well as SoHO/EIT, TRACE, and other broadband imagers in the X-rays and EUV.

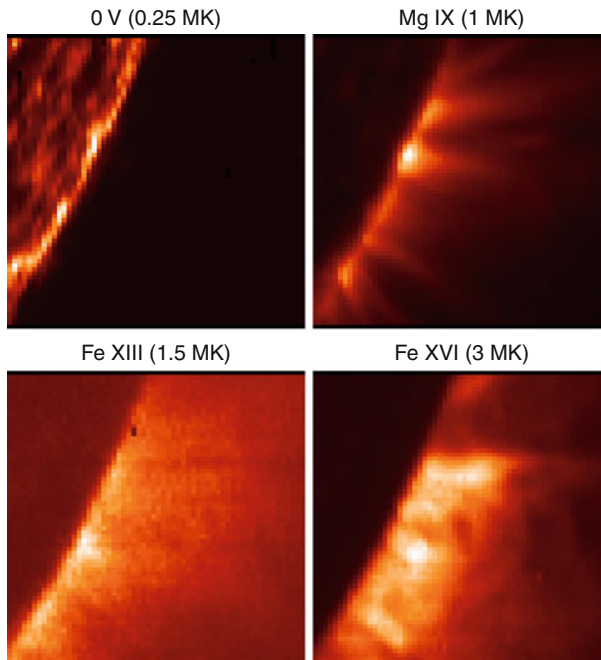
A specific type of emission known as *active region moss* was clearly visible in the 173 Å passband of TRACE. Although this type of emission was mentioned in early observations taken

by Skylab, TRACE provided the first detailed observations of moss. It is currently thought that the moss emission corresponds to the footpoints of the hot loops seen e.g., in the Yohkoh/SXT images (see, e.g., Martens et al. 2000).

8.2.1 Active Regions Observed with SoHO CDS

Monochromatic imaging in spectral lines emitted in a wide range of temperatures became routine with the SoHO/CDS instrument. Active regions appear very different at different temperatures. Mason et al. (1999) studied an active region at the limb using CDS observations. The core of the active region was found to be very hot in comparison to the surroundings. The density map of the active region derived from Si x line ratio shows that the density is highest (greater than $2.3 \times 10^9 \text{ cm}^{-3}$) in the hot core of the active region. Further studies with CDS, and later Hinode/EIS gave similar results.

Del Zanna and Mason (2003) used both imaging (TRACE) and spectroscopic (CDS) observations to show that the dominant EUV emission in active regions is multi-thermal and unresolved even at $1''$ resolution (TRACE). Its peak emission is around 1.5 MK where Fe XIII is formed (cf. [Fig. 3-57](#)). This diffuse emission forms a background and foreground which needs to be taken into account when analyzing loop structures.



■ Fig. 3-57

Monochromatic images of an active region observed by SoHO/CDS at the limb (Adapted from Del Zanna and Mason 2003). Notice the limb brightening in O v, the warm loops seen around 1 MK, the unresolved emission at 1.5 MK, and the bright hot (3 MK) loops in the core

The SoHO/CDS instrument also allowed measurements of EM and DEM from the observation of several spectral lines. These can be compared with simulated emission measures derived from theoretical models. [▶ Figure 3-58](#) shows a sample DEM for an active region. The peak emission is at $\log T[K] \simeq 6.3$, (2 MK) compared to the quiet Sun which has peak emission at about 1.5 MK, and coronal holes where there is hardly any emission above 1 MK.

The large, quiescent 1 MK loops are best seen in the TRACE 173 Å band, sensitive to Fe IX/Fe X emission, and a considerable number of studies has been published. Early results from TRACE indicated that these warm loops were almost isothermal along their length and “over dense”, compared to what expected in hydrostatic equilibrium. However, TRACE measurements of temperature and density along and across coronal loops have severe limitations, which only spectroscopic measurements can resolve. SoHO/CDS showed that these quiescent warm (1 MK) coronal loops are nearly isothermal at each location along their length (e.g., Del Zanna 2003, see [▶ Fig. 3-59](#)), but are not isothermal along their length, something later confirmed with Hinode/EIS observations (Tripathi et al. 2009). With CDS, it was also possible to follow the coronal loops down to the chromosphere (Del Zanna 2003).

SoHO/CDS also showed (Del Zanna et al. 2006b) that hot and cool loops are intermingled and tend to keep their characteristics, in particular the temperature, for a very long time ([▶ Fig. 3-60](#)). In essence, most structures must continuously be heated in a steady way to maintain their temperatures. These results radically changed our knowledge of loops, given that it was widely thought that cooler loops naturally form via cooling of the hotter ones.

8.2.2 Active Regions Observed with Hinode EIS

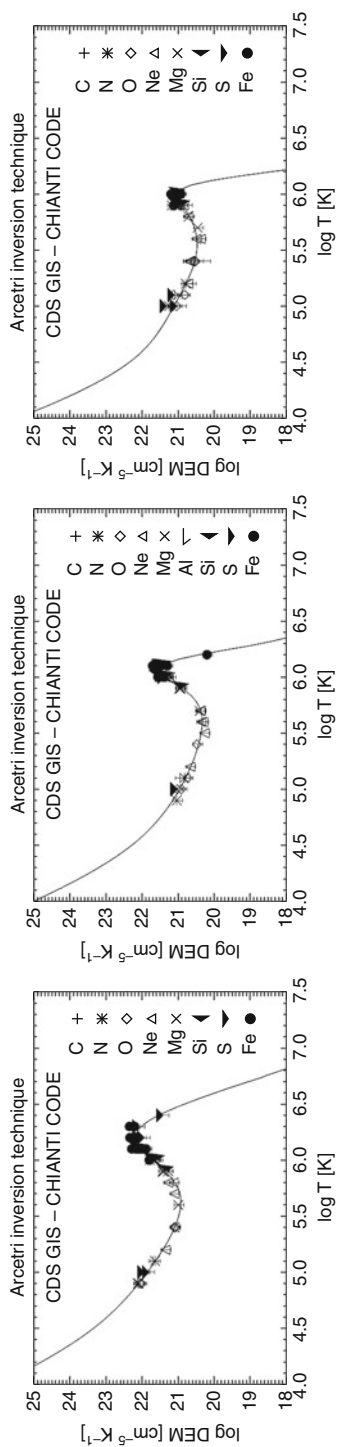
A major advantage of the Hinode/EIS instrument over previous ones is the ability to measure Dopplershifts and line widths in coronal lines emitted above 1 MK. New features have emerged. EIS observations of active regions have shown a clear pattern of blueshifts (Del Zanna 2007, 2008; Doschek et al. 2007), increasing at higher temperatures. The blueshifted areas are always in low-density, low-emission regions, and have associated large line widths, indicating that they are places where strong heating is taking place. [▶ Figure 3-61](#) shows one example, from Del Zanna (2008).

Some signatures of blueshifted emission in “coronal” ($T > 1$ MK) lines were previously obtained from SMM/UVSP, SoHO/CDS, and SUMER, but most observations had a poor spatial coverage and/or resolution. Perhaps surprisingly, loops tend to have smaller line widths.

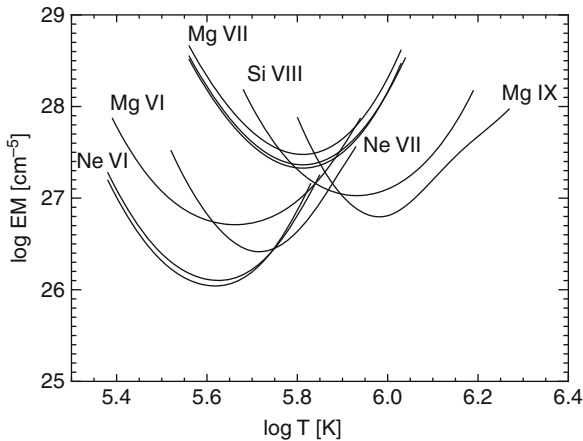
Hinode/EIS has also shown that almost all active region loops exhibit strong redshifts in both legs, with increasing values toward the footpoints, in progressively cooler emission lines (Del Zanna 2007, 2008), as described in [▶ Sect. 4.3](#).

8.3 Coronal Heating

The amount of energy required to sustain and heat the corona is very small, compared to e.g., the total energy radiated from the Sun. However, a well-accepted explanation of how the corona is heated is still lacking. Different coronal features might also be heated by different processes. A great variety of mechanisms for coronal heating have been proposed over the last 70 years. Most theories can be grouped into two categories, one hydrodynamic and the other magnetic. In the first one, purely hydrodynamic effects are important, for example, heating by

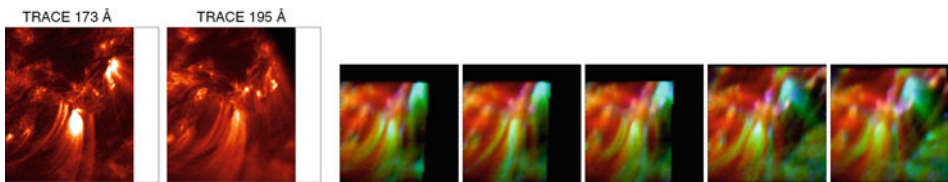


■ Fig. 3-58 DEMs for an active region (left), quiet Sun (centre) and coronal hole (right), obtained from SoHO/ GIS observations (Del Zanna 1999)



■ Fig. 3-59

EM loci curves from SoHO/CDS observations of a warm active region loop, showing nearly isothermal plasma (Del Zanna 2003) and photospheric Mg/Ne abundances

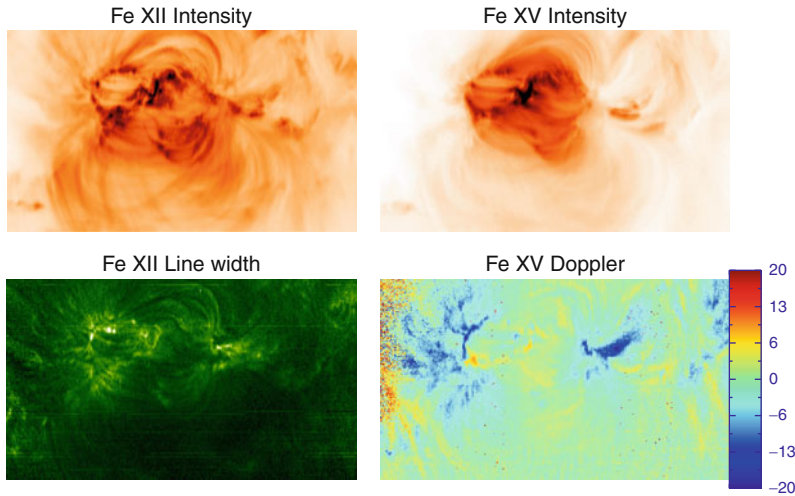


■ Fig. 3-60

From the left: TRACE 173 Å and 195 Å EUV images of the legs of warm (1 MK) loops; false-color images obtained from monochromatic CDS images (Ne VII, 0.7 MK, in blue; Ca X, 1 MK, in green; and Si XII, 3 MK, in red over a long time period, 12 h (Figures adapted from Del Zanna et al. 2006b)). The warm loops (green) are clearly seen in TRACE; however there are cooler (blue) and hotter (red) loops as well. Cooler and hotter loops are intermingled and fill the entire AR volume. They are also nearly isothermal at each location

the acoustic waves which are observed in the photosphere and chromosphere. In the second one, energy is channeled via the magnetic fields, for example via microflares, current dissipation, or magnetic wave dissipation. Within the above categories, theories can be further grouped into DC and AC processes. With the AC processes, waves are generated and then dissipated to heat the plasma. With the DC mechanism, stresses in the magnetic structures are slowly built up, until a point is reached when instability occurs and a relaxation process releases the energy. For recent reviews on the subject, see Narain and Ulmschneider (1996), Klimchuk (2006), Erdélyi and Ballai (2007).

Current efforts are both on the observational side, to measure plasma properties, and on the theoretical side. Modeling entire active regions is computationally very intensive and complex. Three-dimensional MHD codes have begun to produce interesting results, however they still



■ Fig. 3-61

Hinode EIS observations of an active region. *Left*: monochromatic (*negative*) image in Fe XII (*top*) and (*below*) line width. *Right*: monochromatic (*negative*) image in Fe XV (*top*) and (*below*) a Dopplergram (± 20 km/s), showing strong blueshifts in regions of low emission outside the hot loops in the core of the active region (Adapted from Del Zanna 2008). The field of view is $400'' \times 230''$

have inadequate spatial resolution, in particular to resolve the transition region, where steep gradients in density and temperature occur.

8.3.1 Coronal Heating in Loops

Active region loops are the brightest and geometrically simplest structures observed in the solar corona. They have been studied extensively, in an attempt to better define the coronal heating mechanism. It is well established that loops are arch-like structures of nearly constant cross section which are connected to the photosphere where strong magnetic fragments of opposite polarity are located. The pressure exerted by the magnetic field present in the corona is much stronger than the dynamic pressure of the plasma, so loops can be considered as magnetic flux tubes. In these conditions, the magnetic field is known to be *frozen in* with the plasma, i.e., magnetic fields always move with the plasma. Vice versa, plasma elements can freely move along field lines but not across. It is also known that thermal conduction across magnetic field lines is many orders of magnitude lower than conduction along field lines, so effectively coronal loops can be modeled to a first approximation as one-dimensional flux tubes.

8.3.2 Hydrostatic Models and the RTV Scaling Laws

Historically, the first attempts to model coronal loops was with hydrostatic models. Rosner et al. (1978) [RTV] studied observations recorded by the X-Ray Telescope aboard Skylab and developed a model of the solar corona, based on coronal loops. Rosner et al. (1978) extended the

coronal loop model of Landini and Monsignori Fossi (1975) to study the relation of the physical quantities in the case of static equilibrium of a symmetric loop having constant cross section. The equation for energy conservation then becomes

$$\frac{d}{ds} \left(\kappa_s T^{5/2} \frac{dT}{ds} \right) = E_R - E_H(s) \quad (3.31)$$

where s is the spatial coordinate along the loop; $E_R = N_e^2 \Lambda(T)$ are the radiative losses; E_H is the volumetric heating rate; T is the temperature; and κ_s is the coefficient for thermal conductivity.

The assumption of symmetry means that the heat flux should vanish at the loop top ($s = L$): $\left. \frac{dT}{ds} \right|_{s=L} = 0$, and the equation can be integrated by prescribing boundary conditions at the foot-points and the form of the heating function $E_H(s)$. With the assumption that $E_H(s)$ and the pressure are constant along the loop, and using an approximation for the radiative losses, RTV showed that the maximum temperature T_{\max} (at the apex) is related to the pressure and the semi-length L by the scaling law:

$$T_{\max} \simeq 1.4 \times 10^3 (PL)^{1/3} \quad (3.32)$$

and showed that, within a factor of 2, it appeared to fit the Skylab observations of the X-ray loops well. RTV also derived a second scaling law:

$$E_H \simeq 9.8 \times 10^3 P^{7/6} L^{-5/6}. \quad (3.33)$$

Loops having the same pressures but longer lengths require less energy input. These scaling laws have been applied for a long time in solar and stellar physics, however solar observations have clearly shown that loops are very dynamic structures and detailed hydrodynamic modeling is needed.

8.3.3 Hydrodynamic Models of Active Region Loops

It is common to neglect the details of the effect of the magnetic field on the heating by defining a general heating function E_H (the volumetric heating rate) and to solve the 1D hydrodynamic equations of mass, momentum, and energy conservation for a single-fluid loop, which in their Eulerian form are:

$$\frac{\partial \rho}{\partial t} + \frac{\partial}{\partial s} (\rho v) = 0, \quad (3.34)$$

$$\frac{\partial}{\partial t} (\rho v) + \frac{\partial}{\partial s} (\rho v^2) = \rho g_{\parallel} - \frac{\partial P}{\partial s}, \quad (3.35)$$

$$\frac{\partial E}{\partial t} + \frac{\partial}{\partial s} ((E + P)v) = \rho v g_{\parallel} + \frac{\partial}{\partial s} (\kappa_s T^{5/2} \frac{\partial T}{\partial s}) - N_e^2 \Lambda(T) + E_H, \quad (3.36)$$

where $E = 1/2 \rho v^2 + 3/2 N_e k T$ is the total energy, kinetic and internal of the fluid element; s is the spatial coordinate along the loop; ρ is the mass density; g_{\parallel} is the component of gravity along the loop axis; T is the temperature.

The use of a single-fluid approach is only valid if all particles are thermalised. For the low solar corona in quiet conditions, the thermal assumption (i.e., that particles follow a Maxwellian

distribution function) is not very stringent, since the relaxation time for e-e collisions is $\tau_{ee} \simeq 0.01 T^{3/2} N_e^{-1} s = 0.01s$ for $T = 10^6$ and $N_e = 10^9$. After a time longer $(m_i/m_e)^{1/2} \simeq 43$, the ions also become thermal, and after the same time factor, both species are thermalized, and only one temperature can be used: $T \equiv T_e = T_i$.

Given its high temperature and low density, the coronal plasma follows the *perfect gas law*, which can be written, once a single temperature is defined, as $P = (R/\mu)\rho T = k(N_e T_e + N_i T_i) \simeq 2NkT$.

Coronal plasma is mostly composed of protons, helium nuclei and electrons, hence the temperature can be thought of an average value. $P = 2N_e kT$ is the total pressure, where N_e is the electron number density. k is Boltzmann's constant. v is the bulk velocity along the loop; $\kappa_s = 9.7 \times 10^{-7}$ (cgs units) is the coefficient of thermal conduction, assuming classical conductivity, see Spitzer (1965).

$\Lambda(T)$ is the optically thin radiative loss function, i.e., is the sum of all the emissivities of the lines and continuum (total power per unit emission measure). It is a function strongly dependent on the temperature and the chemical abundances. \blacktriangleright Figure 3-62 shows that the main contributions are from oxygen, silicon, iron. The radiative losses also depend on the ion abundances within each element.

The heating function E_H is an often prescribed function of space and time, and the hydrodynamic response of the plasma is studied in detail and compared to observations. Priest et al. (1998) attempted to match models with a specific set of X-ray observations. They showed that

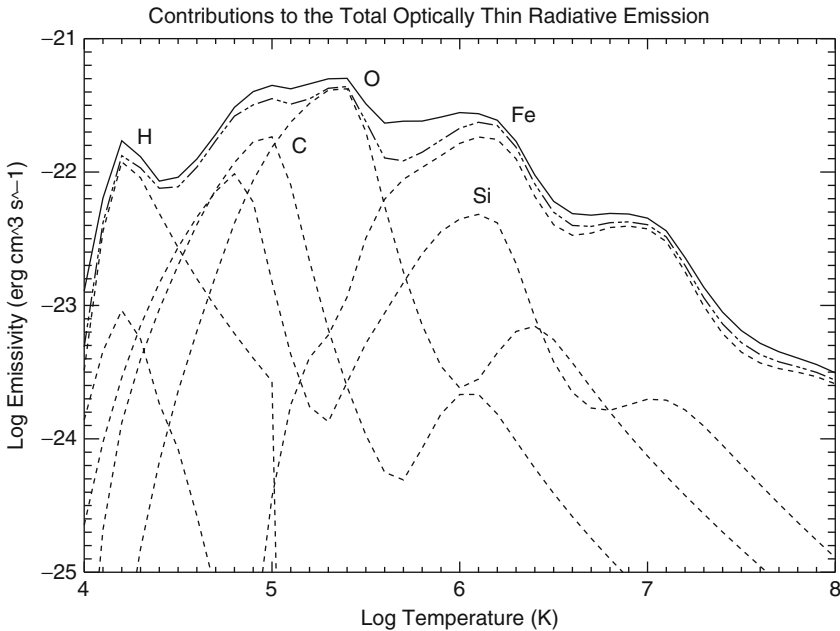
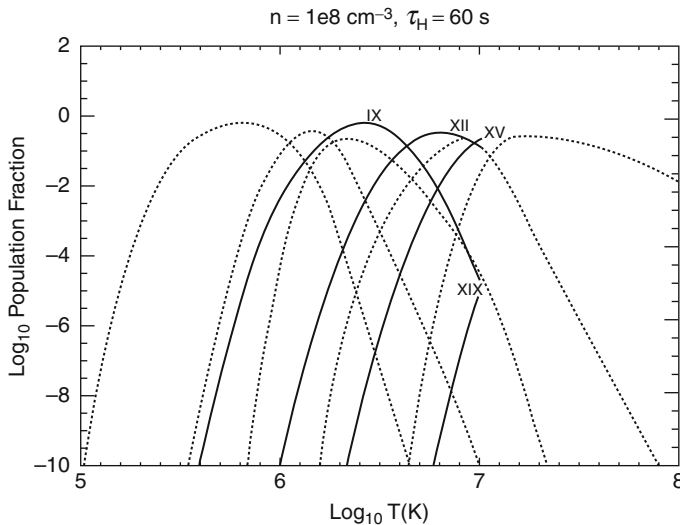


Fig. 3-62

The total optically thin radiative loss function. The plot was calculated using coronal abundances. The solid line is the total radiative loss function for the plasma; the dashed lines show the contributions from the individual elements

the footpoint to apex temperature profile, calculated under the assumption of static equilibrium within the loop, is highly sensitive to the spatial distribution of heat deposition along the loop. They compared predicted intensities from various theoretical models with specific Yohkoh observations and found that a uniform heating model was most appropriate. Even though their analysis was later shown to have some severe limitations, it did start a long and fruitful debate on the heating mechanism for coronal loops, with further attempts to match theory and observations.

To this purpose, several hydrodynamic codes have been developed to model the response of coronal loops to different heating functions. For example, the HYD(rodynamic) and RAD(iation) code (HYDRAD) (Bradshaw and Mason 2003) is a hydrodynamics code which incorporates time-dependent ionization and forward modeling of emission from the solar atmosphere. The predicted intensities for the spectral lines are critically dependent upon the population of emitting ions and in traditional hydrodynamic models, these have been assumed to remain in equilibrium throughout the evolution of the plasma. However, the timescale for ionization in the solar atmosphere can be on the order of minutes. Thus, given activity timescales on the order of seconds in solar loops, it is easy to see that the assumption of equilibrium ion populations may not be valid (see, e.g., [Fig. 3-63](#)). This has extremely important consequences for the correct interpretation of observations, the accurate treatment of optically-thin radiation in numerical models and forward-modeling studies derived from model results. HYDRAD handles non-equilibrium ion populations in the solar atmosphere and the consequences for optically-thin radiation, in a self-consistent way. The equations of hydrodynamics and ionization balance are coupled together at each time step during the evolution of the plasma.



■ Fig. 3-63

The *solid curves* show the relative abundances of a selection of Fe ions out of equilibrium, while the *dotted curves* show the equilibrium ion population, as a function of the electron temperature (Adapted from Bradshaw 2009)

8.3.4 Microflares and Nanoflares


Small flares with an energy content of 10^{-6} to 10^{-9} of a typical large flare are classified into *microflares* and *nanoflares*. Microflares are observed not only in ARs but also in the QS regions. Small-scale coronal activity is believed to be of importance for solving the coronal heating problem. Parker (1988) was the first one to suggest that frequent small-scale magnetic reconnections producing nanoflares could be responsible for heating the solar corona. The idea was further developed by Cargill (1994) and others. Basically these small-scale magnetic reconnections prevent indefinite tangling of coronal field lines and help dissipate the magnetic energy stored in the magnetic field lines due to photospheric motions. Magnetic reconnection would lead to particle acceleration. When the particles hit the loop footpoints, this would lead to the evaporation of material. Searching for evidence of upflows (blueshifts in spectral lines) could confirm such models. We do have some observational evidence for magnetic reconnections in the corona and dissipation of magnetic energy into thermal energy in form of micro-flares, flares, and CMEs. However, detection of nanoflares has so far been elusive. Although TRACE, with its $1''$ spatial resolution, seems to resolve loops, it is possible that these loop structures could be made up of many bundles of magnetic flux tubes (strands), each of which could be heated separately.

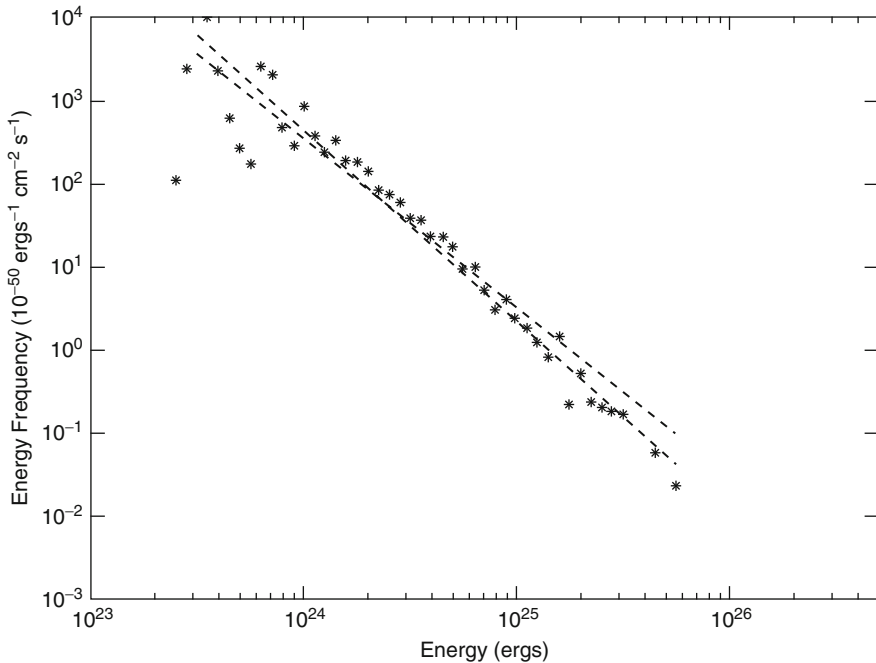
One prediction from nanoflare heating models is the presence of plasma in the corona with temperatures in excess of 5 MK. Various studies based on broadband imaging have suggested the possibility that this hot plasma is present. However, spectroscopic measurements have so far not shown conclusive evidence, and further studies are needed. With Hinode/EIS one can study high-temperature coronal emission from Fe xvii and Ca xvii ions formed at peak temperatures of $\log T = 6.6$ and 6.7 , respectively. Maps made in Fe xvii and Ca xvii emission indicate that the hottest portions of the active region are localized at low heights in the active region core, while further out the emission from hot material is much weaker (O' Dwyer et al. 2010).

The solar corona exhibits a plethora of transient energy releases over many scales, from large solar flares down to microflares. Active region microflares (or active region transient brightenings) were first identified in X-rays with YOHKOH/SXT, possibly associated with the emergence of new magnetic flux. About 1–40 of these events per active region per hour have been observed, lasting a few minutes and reaching high temperatures (up to 10 MK) and electron densities (10^{10} cm^{-3}). Microflares have about a million times less energy than a large flare. Microflares have also been observed in EUV, however, five times as frequent as X-ray microflares. Microflares originating from active regions seem from RHESSI observations to have a non-thermal electron spectrum with a low energy cutoff.

Drake (1971) first noted that the distribution of flare energies W can be fit by a power law function:

$$dN = AW^{-\alpha} dW \quad (3.37)$$

with a slope of $\alpha = 1.7$ – 1.8 . Similar power laws were found in the radio and soft X-ray regions by Lin et al. (1984), with α about 2. These authors pointed out that one may integrate this power law distribution to determine the total power emitted in transient brightening or micro-flare events. If the slope is steep enough ($\alpha > 2$), these transient events would be sufficient to explain the *quiescent heating* of the solar corona. Many authors have found power law indexes lower or higher than two, depending on which instrument was used. One example is given in  Fig. 3-64. One major problem in these types of studies is the fact that what is often observed is a by-product of the primary energy release, not the actual energy, as shown for example with a simulation by Parenti et al. (2006).



■ Fig. 3-64

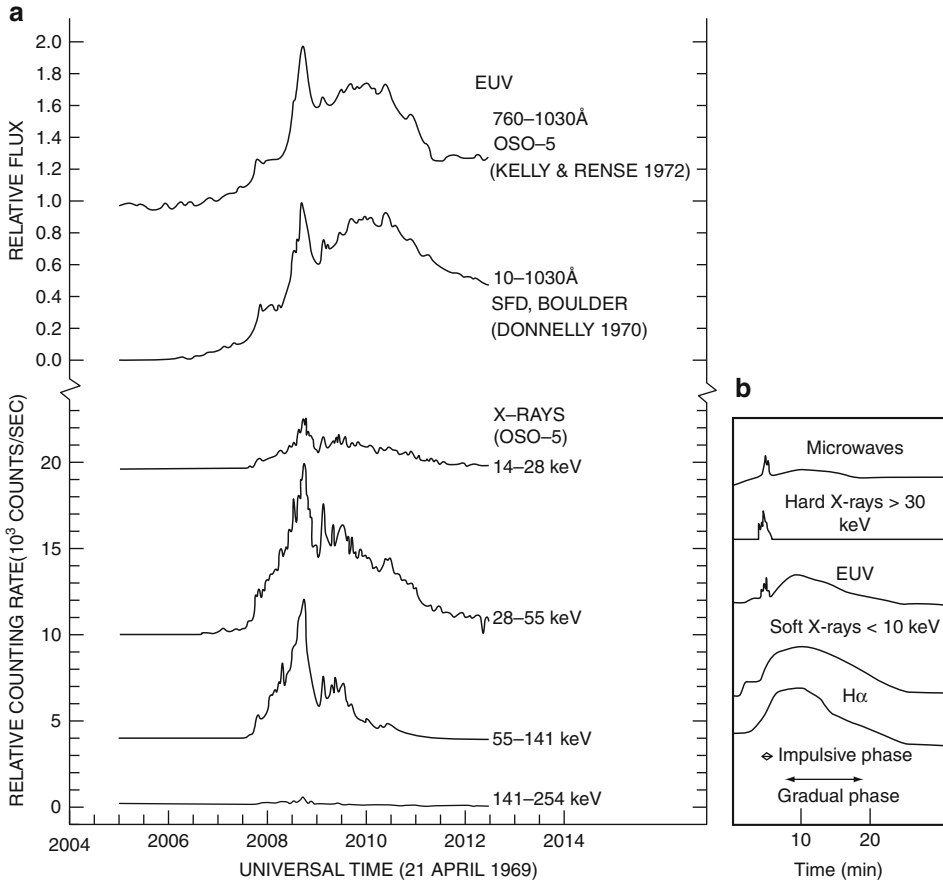
Frequency of occurrence of events vs. event energy obtained from TRACE EUV images (Parnell and Jupp 2000)

9 Solar Flares and Coronal Mass Ejections

9.1 Solar Flares

Solar flares are violent explosions in the solar atmosphere involving the sudden release of energy: bursts of particle acceleration, plasma heating, and bulk mass motion (for reviews, cf. Aschwanden 2006; Culhane and Jordan 1991; Phillips 1992; Sturrock 1980; and the *living review* by Benz 2008). Over periods of less than an hour, a flare can release energy of up to 10^{32} ergs, emitting high levels of radiation in wavelengths ranging from radio to short wavelength X-rays and even gamma rays during large events. The energy range of flares extends over many orders of magnitude. The currently accepted classification of flare size is based on the power irradiated in the 1–8 Å channel of the *Geostationary Orbital Environmental Satellite (GOES)* family. The events are classified as belonging to class A, B, C, M, or X, if their peak emission increases over 10^{-8} , 10^{-7} , 10^{-6} , 10^{-5} , 10^{-4} W m⁻², respectively.

The first observations of solar flares were taken independently by R. C. Carrington and R. Hodgson in 1859 (Carrington 1859). Carrington said “While engaged in the forenoon of Thursday, Sept 1, in taking my customary observation of the forms and positions of the solar spots, an appearance was witnessed which I believe to be exceedingly rare.” He goes on to describe the appearance of “two patches of intensely bright and white light”, which we now associate with the flare ribbons (footpoints of post-flare loops).

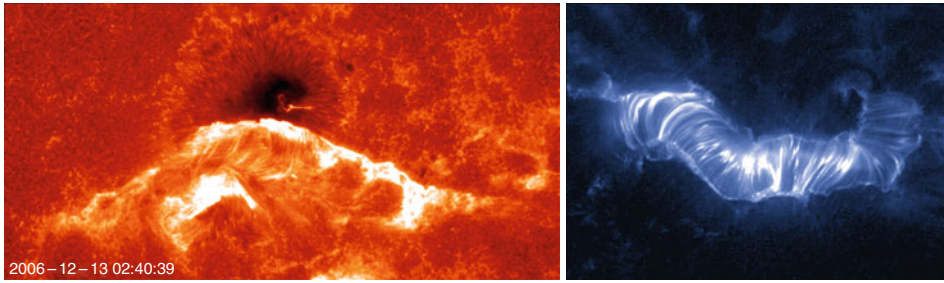


■ Fig. 3-65

Observed *lightcurves* in the EUV, X-rays, and hard X-rays of a solar flare (a (left), after Kane et al. 1979, and b (right) sketch of the typical behavior at different wavelengths as a function of time)

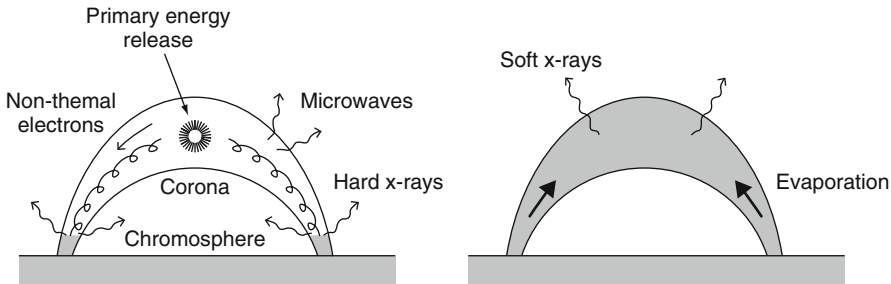
When observed at different wavelengths, flares have a very different temporal evolution. ▶ [Figure 3-65](#) (left) shows a typical example. Hard X-rays normally show an *impulsive* behavior, the same observed in microwave radio emission, and thought to be related to nonthermal processes. The EUV emission also shows some impulsive behavior, due to low-temperature line emission, however the bulk of the emission is thermal and occurs during the *gradual* decaying phase (see ▶ [Fig. 3-65](#), right). Soft X-ray emission normally shows peak emission after the hard X-ray peak, and is followed by the gradual phase.

During a solar flare, the temperature can rise in excess of 10 MK, so that the plasma emits strongly in the EUV and X-rays. A typical *two-ribbon* flare is characterized by morphological features which include separating ribbons of chromospheric H α emission (▶ [Fig. 3-66, lhs](#)) joined by a rising arcade of hot but rapidly cooling EUV loops (▶ [Fig. 3-66, rhs](#)), with hard X-ray emission at their summits and at their feet (as seen by RHESSI). Many events are normally associated with large flares, for example, filament eruption, acceleration of large number of particles, triggering of vast ejecta (Coronal Mass Ejections, see below).



■ Fig. 3-66

Left: Image in the Ca II H spectral line of a large flare on December 13, 2006 observed with the Hinode/Solar Optical Telescope (SOT). The image shows the separating flare ribbons in the chromosphere. **Right:** Post-flare loop arcades during the 'Bastille day flare' on July 14, 2000 observed in EUV with the TRACE satellite



■ Fig. 3-67

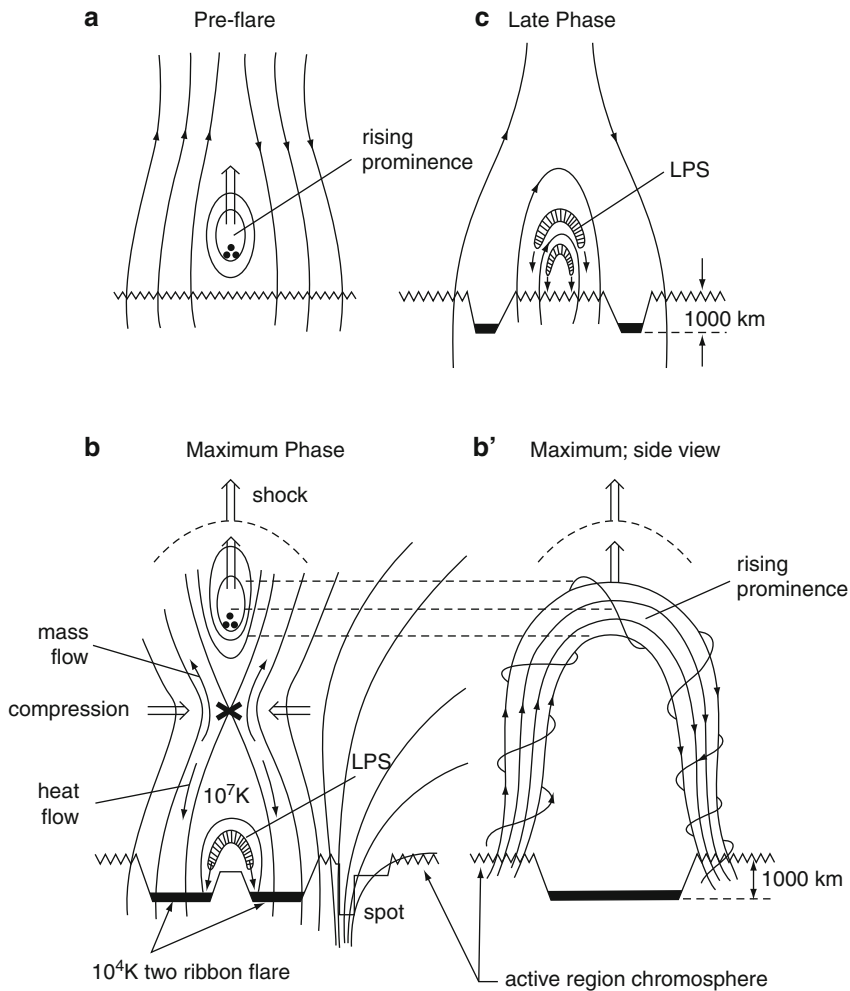
Illustration of the production of microwaves, soft X-rays, and hard X-rays in solar flares after Priest and Forbes (2002)

Flares are believed to be driven by stored non-potential magnetic energy and triggered by an instability in the magnetic configuration. This sudden release of energy and the transport of this energy are still not well understood. There is evidence (for example from the hard and soft X-rays) that both thermal and nonthermal processes occur in flares.

As described in ● Fig. 3-67, a general interpretation of the observed flare features is that particles are somehow accelerated by the magnetic energy released higher up in the corona and are transported down to the footpoints of the loop structures. The energetic electrons then lose all their energy in Coulomb collisions with the dense ambient cold plasma (thick-target nonthermal bremsstrahlung, see, e.g., Brown 1971), giving rise to strong radio, hard X-ray, UV, and even white light. The thick-target nonthermal bremsstrahlung is however very inefficient, and far too many electrons (compared to those available in the corona) need to be accelerated to high energies. Other theories still accept the presence of coronal reconnection in the corona, but advocate the presence of Alfvén waves to transport the energy down (see, e.g., Fletcher and Hudson 2008 and references therein).

Although not all flares can be explained by a single model, it is generally accepted that a standard model for the gradual phase that fits most observations and that is theoretically well understood exists. The most widely accepted flare model is known as the *CSHKP standard model*

(based on the original work of Carmichael, Sturrock, Hirayama, Kopp and Pneuman). In this scenario, an instability causes a filament to rise, which, in turn, causes the magnetic field to be opened up (🔗 Fig. 3-68). The rapid temperature increase during the impulsive phase produces an enhanced pressure in the heated region. This overpressure drives downward-moving cool plasma and evaporation from the lower solar atmosphere (chromosphere) during the flare *gradual* (or *decay*) phase. This results in a hot (over 10 MK) plasma filling the magnetic loop structures in the corona which have several thousand kilometers altitude. This plasma then cools by conduction and radiation forming post-flare loop structures.



■ Fig. 3-68

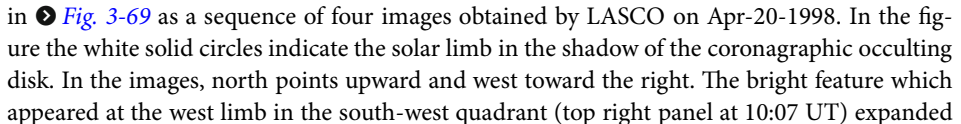
Temporal evolution of a flare after Hirayama (1974), starting from (a) a rising prominence, (b) which triggers X-point reconnection beneath an erupting prominence, shown in side-view (b'), and (c) ending with the draining of the chromospheric, evaporated, hot plasma from the flare loops

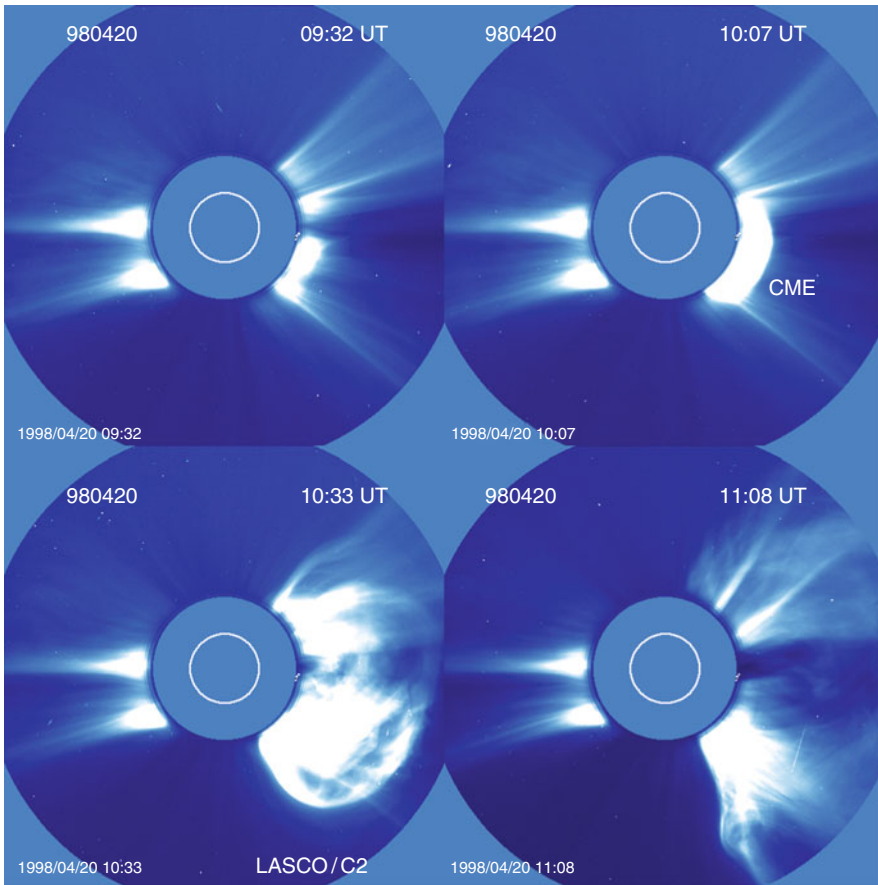
One of the limitations in testing theoretical predictions of chromospheric evaporation and cooling has been a lack of spectroscopic measurements that cover a broad range of temperatures during the lifetime of a flare with sufficient spatial resolution. Earlier observations have been performed with various instruments, but there were limitations mainly in their spatial capability. Blue-shifted components of a few hundred km s^{-1} have been reported in H- and He-like lines observed in the X-rays, for example, with the SMM X-ray polychromator (XRP) Bent Crystal Spectrometer (BCS) (see, e.g., Antonucci et al. 1982) which did not have spatial resolution. The blueshifted components were thought to be located at the footpoints of the X-ray loops. Some spatial resolution was obtained with the SMM Ultraviolet Spectrometer and Polarimeter (UVSP, see Mason et al. 1986) and XRP Flat Crystal Spectrometer (FCS) observations, however it was only with SoHO CDS observations that more information was obtained. Czaykowska et al. (1999) confirmed that strong blueshifts in hot Fe XVI (3×10^6 K) and Fe XIX (9×10^6 K) lines were located at the outer edges of the flare ribbons, as expected with the CSHKP model. Del Zanna et al. (2002a) presented the first spatially resolved spectral observations of the entire evolution of a small flare, where long-lasting (over an hour) blueshifts of 30 km s^{-1} at the footpoints of a small flare ($T = 9 \text{ MK}$) loop were present. Del Zanna et al. (2006a) confirmed expectation from theory that at the flare kernels, during the impulsive phase of an M1 class flare, strong upflows, progressively larger at higher temperatures (reaching 140 km/s for $T = 9 \text{ MK}$) are seen together with small downflows in the cooler lines. Important contributions in this field are expected from Hinode EIS observations.

9.2 Coronal Mass Ejections (CMEs)

Coronal Mass Ejections (CMEs), often associated with solar flares, are also spectacular and violent phenomena in the solar atmosphere which propagate through the heliosphere and can impinge on the near-Earth environment. The flare which was observed by Lord Carrington in 1859 led to a gigantic CME, large enough to have serious consequences had it happened in the modern-day technology-based era. Remote sensing and in situ measurements from various spacecraft over the past decade or more have revealed that CMEs are the prime agents for interplanetary shock waves, solar energetic particle events, and geomagnetic storms.

A CME is defined as an observable change in the coronal structure which occurs on a timescale between a few minutes and several hours, and also involves the appearance and outward motion of a new, discrete, bright, white-light feature in the coronagraph field of view (Hundhausen et al. 1984). CMEs consist of clouds of hot plasma expelled from the Sun with propagation speeds of up to $3,000 \text{ km s}^{-1}$, and with a mass of 10^{12} kg or more. Both flares and CMEs can accelerate electrons and ions which travel through interplanetary space as far as the Earth's orbit and beyond. The CME is often preceded as a shock front which, when it reaches the Earth, may result into a magnetic storm. Therefore, flares and CMEs can influence the space weather and human activities both in space and on the ground.

CMEs were systematically observed with coronagraphs aboard *Skylab* (1973–1974), *SOLWIND* on board *P78-1* and the Corona/Polarimeter on board *Solar Maximum Mission* (SMM, 1984–1989). Since 1996, the *Large Angle Spectrometric Coronagraph* (LASCO) aboard SoHO has provided unique observations of CMEs. An example of a spectacular CME is shown in  as a sequence of four images obtained by LASCO on Apr-20-1998. In the figure the white solid circles indicate the solar limb in the shadow of the coronagraphic occulting disk. In the images, north points upward and west toward the right. The bright feature which appeared at the west limb in the south-west quadrant (top right panel at 10:07 UT) expanded



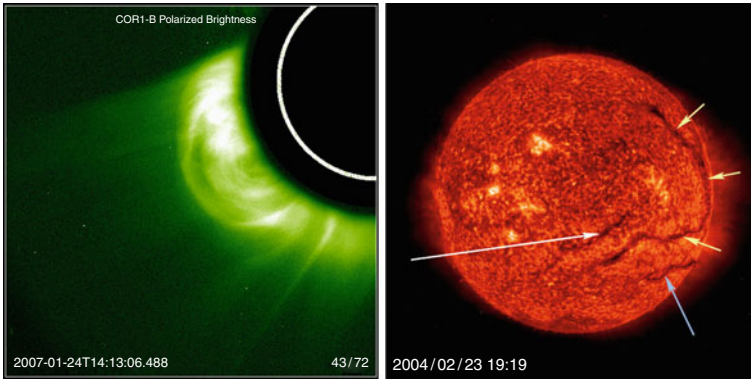
■ Fig. 3-69

Series of LASCO images showing a coronal mass ejection at the west limb. The appearance of the CME was first detected by LASCO at 10:07 UT (*Top right panel*). The white circles in the images mark the solar limb. In the images north points upward and west toward the right. Courtesy: SoHO/LASCO consortium

outward in the following images. This feature moved outward through the corona with a speed of about $1,863 \text{ km s}^{-1}$. A recent collection of reviews and papers can be found in ‘Coronal mass ejections’ (Kunow et al. 2006). The recent launch of the STEREO spacecraft has provided more CME observations.

The identification of the source regions, the triggering and acceleration mechanisms of CMEs have been the subject of intensive research in solar physics since their detection in the 1970s. Many features have a close but not unique association with CMEs and are still not well understood. For example, solar flares are often observed in close association with CMEs. It is generally believed that both flares and CMEs are triggered by a common magnetic instability, the details of which remain unknown.

Filaments (also referred to as *prominences* if observed as bright features over the solar limb) consist of cool material at chromospheric temperatures of about 60,000 K (☉ Fig. 3-70 - right).



■ Fig. 3-70

Left: A CME blasting out from the Sun on January 24, 2007. The observation was taken by the COR1 coronagraph on the *STEREO* mission. The Sun is represented by the white circle superimposed on the occulting disk (*the larger black circle*). The field of view of this coronagraph shows details of events closer to the Sun than either of the two coronagraphs currently operating on *SoHO*. **Right:** EIT image showing He II plasma (304 \AA). The darker, cooler filaments of around $60,000 \text{ K}$ (indicated by arrows) are observed in absorption (Courtesy: NASA/ESA)

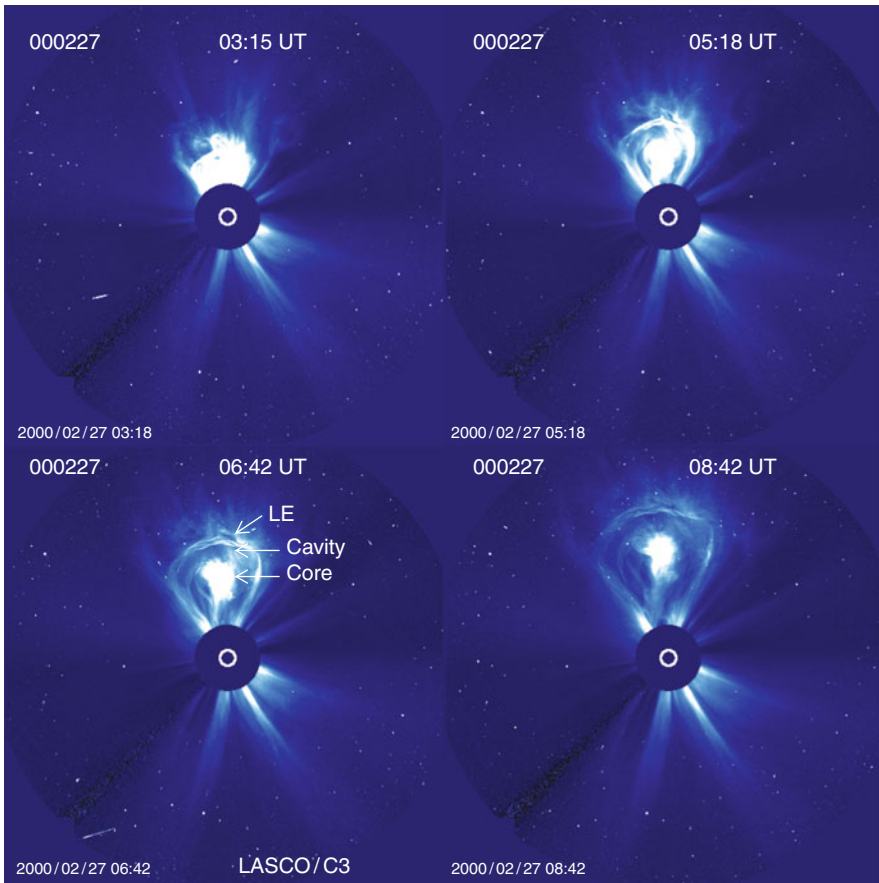
Filaments are often observed to erupt during a flare or CME process. Very often, filaments during the pre-eruption phase slowly rise into the corona. During the eruption, the height normally grows exponentially, and both the filament and the filament-carrying field move together (e.g., Rust 1976). When erupting filaments are associated with a CME, they are sometimes recognized as a bright core in white light images, following a leading edge and a dark cavity, as shown in ● Fig. 3-71. However, many CMEs do not show this structure.

Other features associated with CMEs are coronal dimmings (temporary darkenings in the corona) and apparent “waves” (EUV brightenings that are seen propagating outward). The brightening in X-rays of S-shaped ($\sim 2 \times 10^6 \text{ K}$) coronal loop structures, called sigmoids (see ● Fig. 3-72), has been found to frequently precede CMEs. The sigmoid structures are probably the result of twisted magnetic fields. Shearing and stressing of magnetic field lines above the magnetic neutral line may lead to the helical structure which are S-shaped in projection. When the helical twist exceeds a critical value, the structure might become unstable, producing a disruption of the magnetic field leading to the expulsion of a filament or CME. The S-shaped structure may flare and transform itself into a set of bright loops during the launch of a CME. The active region itself evolves from a sheared sigmoid seen in X-rays to a potential-like post-eruption arcade, as shown in ● Fig. 3-72.

Several studies have found preflare activity such as small X-ray and EUV brightenings at the onset of the filament’s slow rise, which could trigger the eruption. These brightenings are often associated with emerging magnetic flux.

9.3 Theoretical Concepts of CME Initiation

The driver in the CSHKP model is a rising filament, but the magnetic pre-evolution that leads up to the flare and CME instability is not quantified in the various concepts of the CSHKP models.

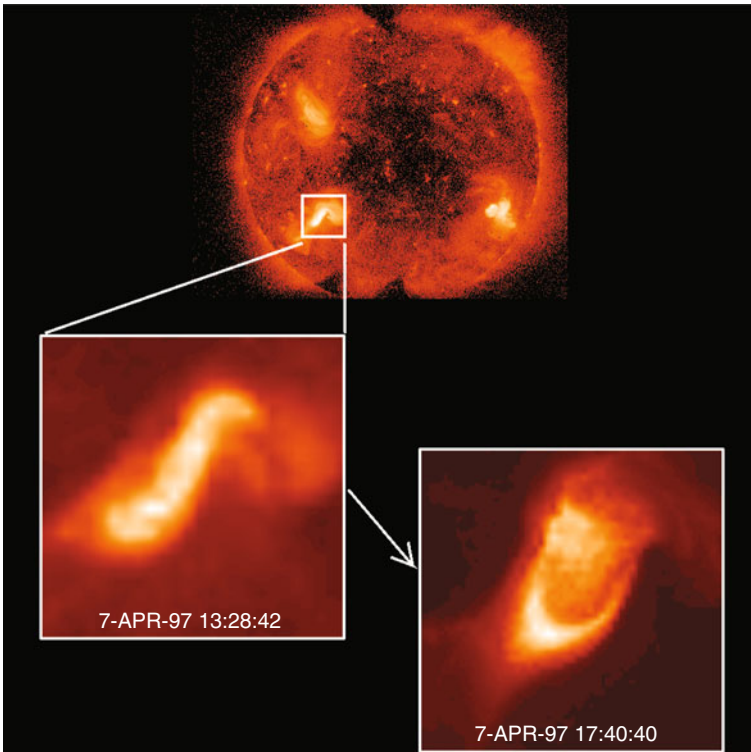


■ Fig. 3-71

A CME observed with the LASCO/C3 coronagraph, showing the typical three-part structure (Figure courtesy of SoHO/LASCO and D.Tripathi)

Several eruption models proposed in the literature involve emerging flux. A review of the ideas to date for the initiation of solar eruptions may be found in Moore and Sterling (2006). They described each of the three basic triggers models (internal tether-cutting (☉ Fig. 3-73), external tether-cutting, and an ideal MHD [e.g., kink] instability) for the case when the erupting filament sustained by a sheared core field is situated in the central lobe of a quadrupolar magnetic field configuration.

Breakout models (e.g., Antiochos 1998) predict that reconnection occurs high above the prominence before the eruption, while tether-cutting mechanisms imply that reconnection *beneath* the prominence unleashes the explosion. Prior to the explosion, the core magnetic field suspending the filament is in force-free equilibrium (Moore and Sterling 2006), the magnetic pressure being balanced by the field's own magnetic tension as well as tension and pressure from surrounding fields. An evolutionary model that starts with a stable (force-free) magnetic field configuration, then applies converging flows as a continuous driver, and demonstrates how



■ Fig. 3-72

Collage showing the sequence from pre-eruption sigmoid to post-eruption cusp/arcade imaged by Yohkoh/SXT on Apr-07-1997 (Courtesy: Yohkoh/SXT team)

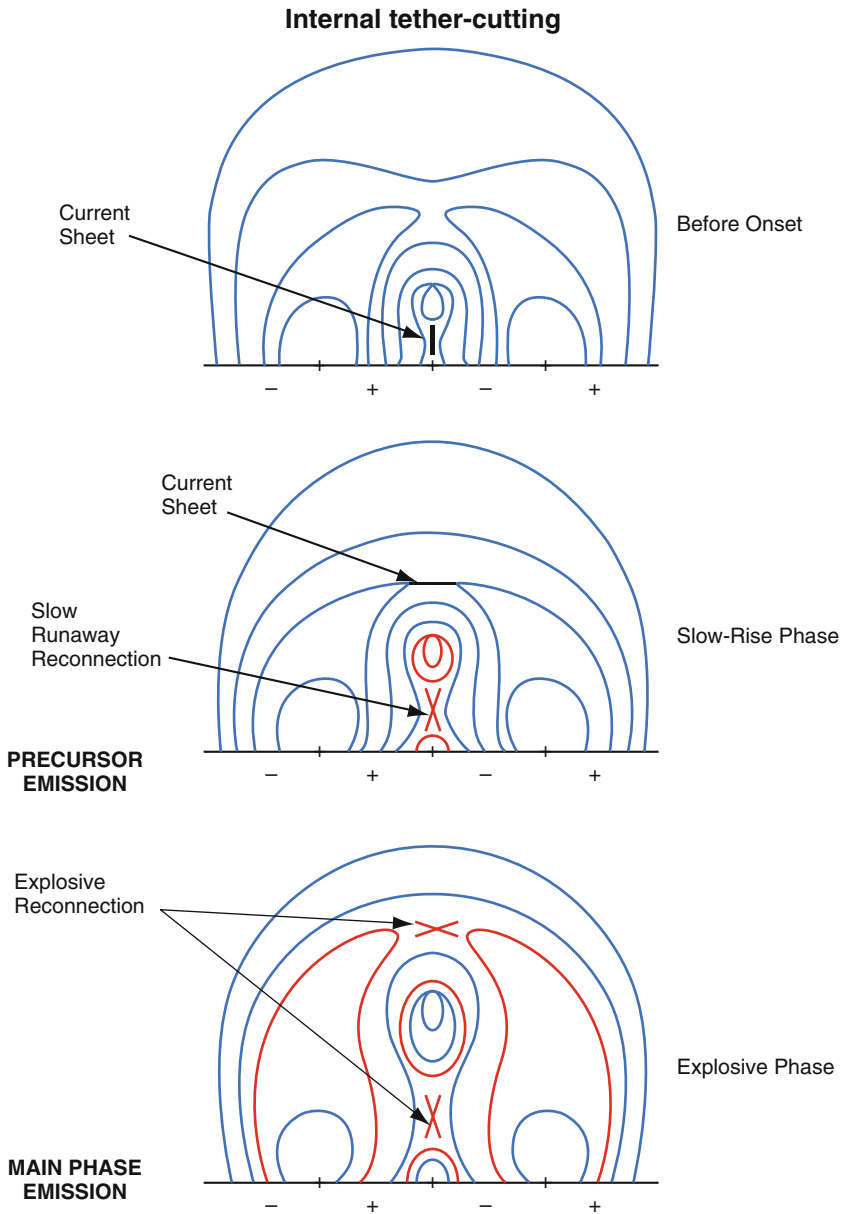
(force-free) evolution passes a critical point where the system becomes unstable and triggers the rise of a filament has been developed by Forbes and Priest (1995) in 2D.

The exponential growth in the early phases of filament eruptions associated with CMEs naturally invokes the presence of some MHD instability. Various successful models of filament eruptions include the helical kink instability of the filament/flux rope (Kliem et al. 2004) and the torus instability (Kliem and Török 2006).

9.4 Flares on Other Stars

Stellar flares have been observed in the visible since the late 1930s in active M-type stars. There is a strong nonthermal continuum in the UV which contributes significantly to the ultraviolet broadbands used in ground-based observations. The dMe stars are the most active and flare-productive stars in our neighborhood. Stellar flares were later observed at all wavelengths, in the radio and with satellites from the UV to the X-rays. As we have seen, one key feature of flares is the sudden heating to temperatures greater than 10 MK, giving rise to strong emission in the EUV and X-rays.

The EXOSAT carried Transmission Grating Spectrometers (TGS) which recorded XUV (50–400 Å) spectra for a few stars. EINSTEIN carried three spectrometers with different



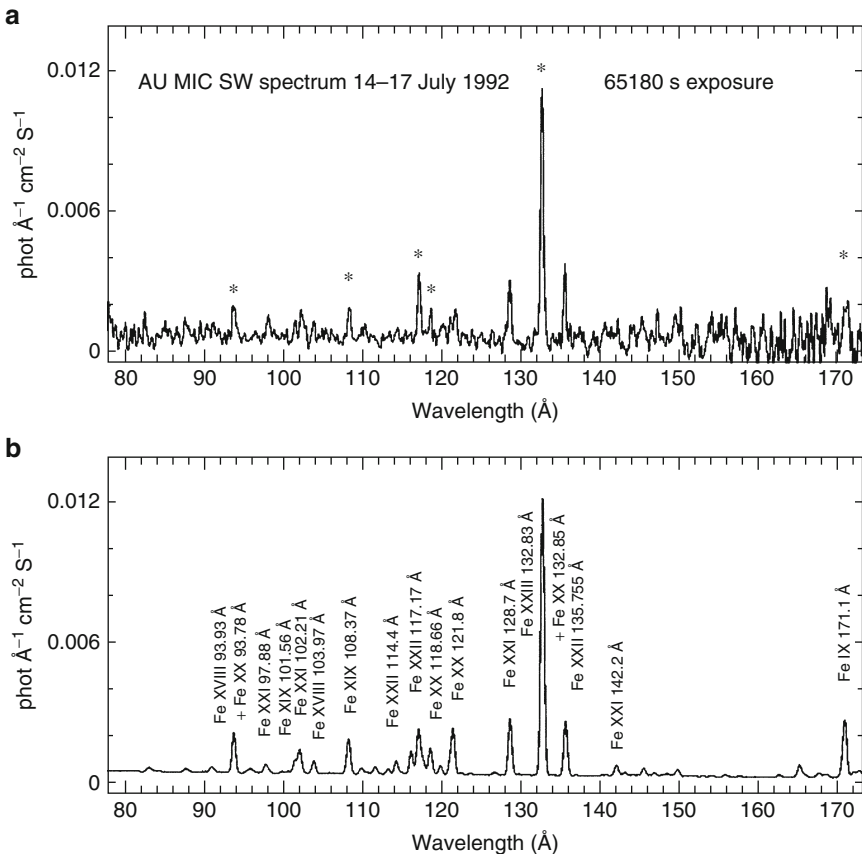
■ Fig. 3-73

Schematic representation of one trigger mechanism for CME eruption, the internal tether-cutting. The magnetic field is shown prior to eruption (*top*), just after eruption onset (*middle*), and when the eruption is well under-way (*bottom*). The sites of the precursor and main phase emissions (observed respectively as preflare brightenings and flare brightenings during the impulsive phase of the eruption) are indicated. Modified figures courtesy of Chifor, Moore and Sterling, after Moore and Sterling (2006)

resolutions which also obtained X-ray spectra of a few sources. ROSAT carried broadband X-ray instruments, which was of limited use for diagnostics. All these early X-ray satellites showed the presence of hot plasma up to a few times 10^7 K in many stellar sources.

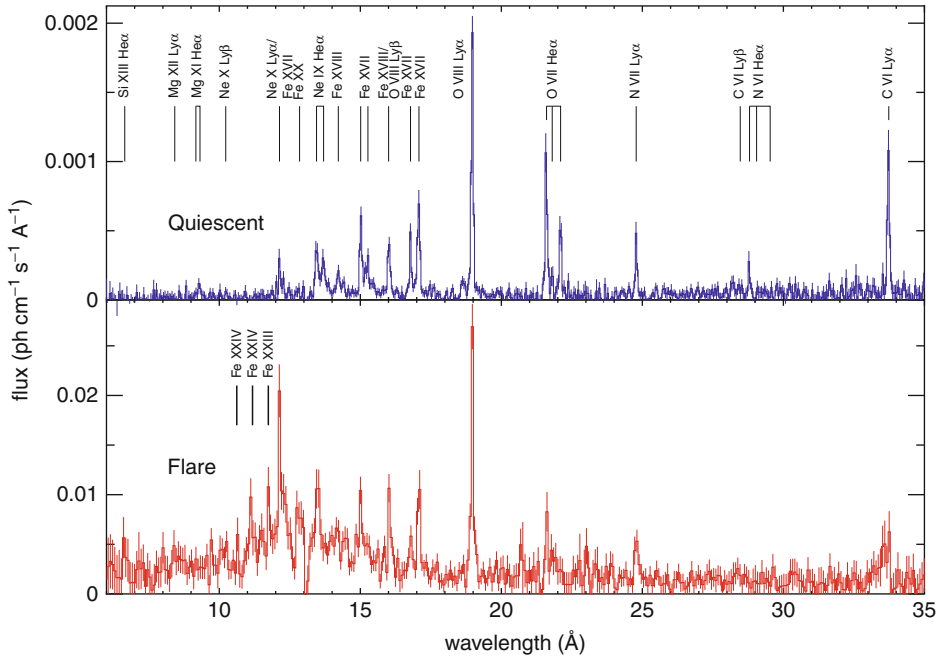
The International Ultraviolet Explorer (IUE), the Hubble Space Telescope (HST), and later FUSE have provided the capability of observing UV emission with spectroscopic instrumentation. With the exception of a few weak forbidden lines formed at flare temperatures, the UV is dominated by emission lines formed in the stellar chromospheres and transition regions.

The Extreme Ultraviolet Explorer (EUVE) satellite carried three grazing incidence spectrometers which observed (in three bands) the 70–760 Å wavelength region. These observations are very rich in diagnostics for flares, in particular with regard to the measurement of electron densities. Temperature sensitivity is also provided, but only by observations of lines from different ions, e.g., Fe XVIII, Fe XX, Fe XXI, Fe XXIII. The sensitivity of EUVE allowed the first time-resolved spectroscopy of a flare in the EUV (Del Zanna 1995, later published in ApJ, see [Fig. 3-74](#)), indicating, as in the solar case, that high temperatures and densities were reached during the peak phase.



■ Fig. 3-74

EUVE spectrum of AU Mic, observed (a) and simulated (b) (Del Zanna 1995)



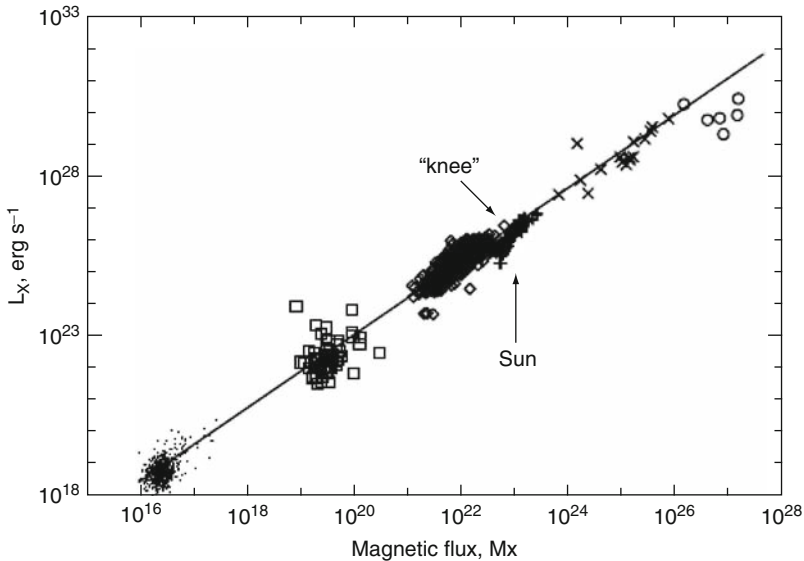
■ Fig. 3-75

XMM-Newton RGS spectra during quiescence and a flare in Proxima Centauri (Adapted from Güdel et al. 2004, courtesy of M. Güdel)

The *XMM-Newton* and *Chandra* satellites, launched in 1999, carried X-ray spectroscopic instruments and have been used to observe many flares in a few nearby stars. The X-rays are rich in strong lines emitted at high temperatures (cf. [Fig. 3-75](#)), but are comparatively poor in diagnostic capabilities, except for the He-like ions. The spectral resolution of the *XMM-Newton* and *Chandra* instruments is much lower than that attained with solar instruments, so diagnostic capabilities are more limited. The next generation of X-ray instrumentation (IXO) should allow more detailed studies of stellar flares, having much higher spectral resolution and sensitivity.

Time-resolved spectroscopy of flares is still largely beyond the current instrumental capabilities, although some diagnostics based on a few of the strongest lines have been obtained. For example, a large flare in Proxima Centauri allowed the measurement of flare lines (see [Fig. 3-75](#), Fe xxiv, Fe xxiii) and of changes in He-like lines (Güdel et al. 2004).

In the large majority of cases, stellar flares have similar characteristics to the solar ones, with the main difference being that luminosities and temperatures are often much larger. For some large stellar flares, temperatures of 100 MK or more have been reported (see the review of Güdel and Nazé 2009), however direct measurements were not obtained and did not take into account the large nonthermal effects which occur in large flares. In the Sun, larger flares have the tendency to have larger emission measures and temperatures, however direct measurements (from line ratios) of temperatures from high-resolution X-rays rarely indicated temperatures above 15 MK (see the review of Doschek 1990).



■ Fig. 3-76

X-ray luminosity L_X as a function of total unsigned magnetic flux for solar features and stars (From Pevtsov et al. 2003)

Young stars have very hot and dense coronae (typical of large solar flares) even in quiescence. The strong magnetic fields measured in these stars suggests that the quiescent state is actually due to continuous flaring, an issue which has not yet been confirmed unambiguously. It has been known for a long time that there is a correlation between estimates of magnetic flux and X-ray luminosity, and that this extends from solar active region core loops to the largest stellar flares, as [Fig. 3-76](#) shows.

A large number of open questions about the X-ray quiescent and flaring emission are still present. It is not clear yet what dynamo mechanism is active in different stars. It is not known if stars have active regions as is the case of the Sun, and if flares are really similar and can be explained with the same models as the solar ones.

10 Solar Wind

By the late nineteenth century, there was substantial evidence of terrestrial effects (magnetic storms and aurorae) being correlated with solar activity (e.g., flares), so it was clear that the Sun had a direct influence on a variety of terrestrial phenomena. An obvious candidate was the direct irradiance from the Sun, but other suggestions soon emerged. As early as 1900, Birkerland proposed that aurorae were due to particles (electrons) emanating from the Sun. The idea was superseded in the 1930s with Chapman and Ferraro's explanation in terms of solar plasma clouds, which is close to our present understanding.

Observations of the tails of comets (Biermann 1951) also suggested the presence of a *solar wind* (SW) emanating from the Sun in all directions, with velocities of 500–1,000 km/s. From 1939, it was also known that the solar corona had a temperature of 1 MK. S. Chapman in 1957

suggested that the solar corona was made up of ionized gas in a stationary condition. At that time the heat flux for thermal conduction by a cloud of electrons and protons was known, the main conductors being the electrons. By assuming spherical symmetry and a static corona, as well as a constant conductive flux, it was straightforward to show that Chapman's model was unrealistic because it predicted finite pressures and divergent densities toward infinity. E.N. Parker knew that the energy in a gas naturally goes into an ordered flow (kinetic energy) and a disordered one (pressure), so it was sufficient to introduce an ordered flow (a coronal expansion) to fix the problem. Parker (1958) brilliantly explained that Biermann's suggestion was perfectly consistent with the natural thermal expansion of the solar corona, a plasma at 1 MK.

To understand Parker's solution it is necessary to simplify the hydrodynamic equations, by considering spherical symmetry, with a stationary ($\partial/\partial t = 0$) and adiabatic ($dS/dt = 0$, where S is the entropy of the gas) flow for a perfect gas (single fluid). The equations for conservation of mass, momentum, and energy can then be written in radial coordinates:

$$\frac{1}{r^2} \frac{d}{dr} (r^2 \rho v) = 0 \quad (3.38)$$

$$\rho v \frac{dv}{dr} = -\frac{dP}{dr} - \frac{GM\rho}{r^2} \quad (3.39)$$

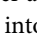
$$v \frac{dS}{dr} = 0 \quad (3.40)$$

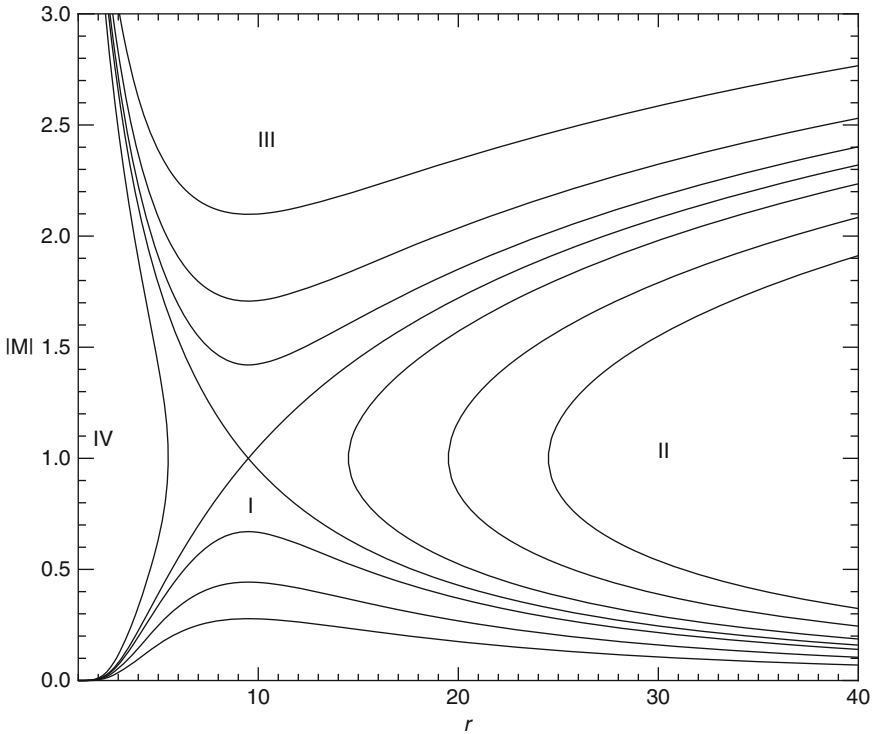
where r is the radial distance from the Sun, P the pressure, and M the solar mass. A relation between the velocity v and r is found by eliminating dP/dr from the conservation of mass and momentum equations. It is straightforward to obtain

$$\left(1 - \frac{c_s^2}{v^2}\right) \frac{dv^2}{dr} = -\frac{2GM}{r^2} \left(1 - \frac{r}{r_c}\right) \quad (3.41)$$

where

$$r_c = \frac{GM}{2c_s^2} = \frac{GM\rho}{2\gamma P} = \frac{GM}{2\gamma RT/\mu} \quad (3.42)$$

is the critical radius, i.e., the distance where the velocity is equal to the sound speed $c_s^2 = \gamma P/\rho$. γ is the ratio of specific heats, and $P = R/\mu T/\rho$ is the perfect gas law, with R the Avogadro number and μ the mean molecular weight. The solutions of the equation (mass loss) can be grouped into four types, and are shown in the  Fig. 3-77. The profile of the velocity as a function of radial distance is shown in terms of the Mach number, the ratio of the velocity v to the sound speed c_s . There are subsonic solutions (the *breezes*, region I in the figure), where the velocity is always below the sound speed. These lie below the two transonic solutions, which are the curves that intersect at Mach number = 1. The transonic solution that has a very large velocity close to the Sun is not physical, and is not supported by observations. The accelerating transonic solution is of particular interest not only because the velocity starts from zero at the Sun, but also because the density and pressure tend to zero at infinity. This behavior close to and very far from the Sun represents not only a physical solution for the solar case, but also the only one which is stable. This solution also implies that the velocity of the solar wind has to be supersonic near Earth.



■ Fig. 3-77

The solution for mass loss from a star in spherical symmetry and stationary conditions (Courtesy of M.Velli). The plot shows the plasma Mach number (The ratio of the velocity v to the sound speed c_s) as a function of the distance from the Sun, in solar radii

Parker's initial simple model assumed an isothermal gas. This means that c_s^2 is constant and (3.41) can be integrated to find

$$v^2 - c_s^2 \ln v^2 = \frac{2GM}{r} + 4c_s^2 \ln r + \text{const.} \quad (3.43)$$

for large values of r , the velocity $v \sim 2c_s(\ln r)^{1/2}$. To obtain an estimate of the density, one considers that $4\pi r^2 \rho v = \text{const.}$ from which $\rho \sim c_s^{-1} r^{-2} (\ln r)^{-1/2}$, i.e., the density tends to zero for large values of r . The same is true for the pressure, since $P \sim \rho T$. For an isothermal temperature of 10^6 K, the simple model predicts a velocity of 100 km/s at 1 AU, a value which is of the same order as the measured one.

The idea that a supersonic solar wind could exist was not initially accepted by the majority of researchers; however very soon Parker's predictions were confirmed. The Soviet *Lunik* 1 and 2 missions were launched in 1959, and made the first measurements of the solar wind. The definitive proof of a supersonic solar wind was made public after the measurements of the NASA *Mariner* 2 satellite which flew to Venus in 1962. Velocities of 300–700 km/s were measured. It has been clear from the first solar wind measurements that Parker's idea was correct. Indeed, Parker's model explains quite well the mainstream slow component of the solar wind, which has a velocity of about 400 km/s and is predominant within the ecliptic.

10.1 The Heliosphere

Parker also suggested that a radial flow of the SW, combined with the solar rotation, would produce a spiral heliospheric magnetic field in the solar equatorial plane, which is what is observed. A good review of the heliosphere near solar minimum (1996) with significant Ulysses contributions is the book by Balogh et al. (2001). A more recent review of the heliosphere through the last activity cycle is the book edited by Balogh et al. (2008). A recent review on the structure of the global heliospheric field and its connection, both observationally (Ulysses, SoHO) and theoretically, is given by Zurbuchen (2007).

The heliospheric magnetic field is weak (about 5 nT) but omnipresent and has the important effect of shielding the solar system from cosmogenic cosmic rays (GCR). The charged energetic particles are deflected when strong magnetic fields are present. Indeed, there is a clear relation between solar activity (hence heliospheric magnetic field density) and the flux of GCRs observed within the solar system. This was already suggested by Davis (1955) even before the presence of the solar wind was proposed.

It is well known now that a vast number of stellar classes have a hot corona similar to the Sun, so it is natural to expect that stellar winds are a common feature. P Cygni line profiles have been observed in hot stars, and are thought to be caused by radiation-pressure-driven winds. Also red giants and supergiants produce massive winds. Winds in solar-like stars are difficult to observe, and it is only since HST observations of H I absorption in the Ly α line that indirect evidence was provided for stellar winds similar to those of the Sun (see the review by Wood 2004).

One subtle issue is that the external pressure of the interstellar medium is not zero. It would not require a strong pressure to actually inhibit the solar wind and to have a static corona. For example, a pressure of $1.24 \cdot 10^{-12}$ dyne cm $^{-2}$ would be enough to confine a $4 \cdot 10^5$ K static corona with a density of 10^9 cm $^{-3}$. The dependence of the solar wind on the external conditions has been studied in detail by Velli (1994).

Several satellites have orbited nearby planets, but others have gone further afield, to the edge of the solar system, for example *Pioneers* 10 (launched in 1972) and 11 and the *Voyager* 1 and 2, launched in 1977. By 1997, the *Pioneer* missions were terminated, while the *Voyager* missions are still operating.

At the edge of the Heliosphere, the solar wind must encounter and interact with the local interstellar medium (LISM). (see Zank (1999) for a good theoretical review). It was once thought that the boundary was very distant, about 100 AU or more. It was expected that there should be a termination shock followed by a region, called the heliosheath, where the solar wind is slowed down by the pressure of interstellar gas. Indeed *Voyager* 1 and *Voyager* 2 crossed the termination shock in 2004 and 2007 and are currently inside the heliosheath, continuing their amazing journey. The data from these crossings suggest the presence of an unexpectedly strong interstellar magnetic field of about 5 μ G.

10.2 Physical Characteristics of the Solar Wind and Models

A great deal is known about the solar wind from a range of satellites, in particular from the two German Helios satellites, which were launched in 1976 and which observed the inner Heliosphere between 0.29 and 1 AU for many years, providing a wealth of data. For a summary of early results from these two missions, see the two books by Schwenn and Marsch (1990) and Schwenn and Marsch (1991). Peculiar aspects of these satellites were their closeness to the

Sun, and the ability to measure the particle distribution functions. Anisotropic (i.e., far from Maxwellian) distributions have been found, in particular in the fast SW. More recently, a large number of satellites with in situ instruments have been operating, for example, the Advanced Composition Explorer (ACE), Wind, SoHO, and STEREO.

The properties of the solar wind close to the Sun are also obtained by indirect measurements, by the scintillation of the radio signals from distant objects such as quasars when their line of sight is close to the Sun. The signal is modulated by the density and flow velocity fluctuations, and with many line-of-sight measurements it is possible to construct a map of the solar wind speed, which appears to increase very close to the Sun (within 20–30 R_{\odot}). The first array of detectors were built by A. Hewish at Cambridge University, and nowadays many such arrays exist over the world.

The particle velocity is radial, with values in the range 300–800 km s^{-1} . Note that the wind needs about 4–5 days to reach Earth, and a few months to reach the outermost planets. The main plasma constituents (95%) are protons and electrons, with the rest mainly α particles. The Coulomb drag is caused by the interactions between ions and protons, and results in all minor ions (i.e., ions form all elements except H, He) to move at equal speeds with the protons, a fact which is observed in the SW. The velocity distribution is mainly bimodal, with a highly variable, slow component around 400 km s^{-1} , and a fast one, more steady around 750 km s^{-1} .

Close to Earth, at 1 AU, the characteristics of the slow SW are: the mean temperatures: $T_e \simeq 1.5 \times 10^5$; $T_p \simeq 4 \times 10^4$; $T_{\alpha} \simeq 2 \times 10^5$ K; the intensity of the magnetic field is in the range $2 - 10 \times 10^{-5}$ G; the plasma β is typically around 1–2, though becomes larger than 3 in the fast SW; the sound speed is about 40 km/s, of the same order of the Alfvén speed. So the solar wind is not only supersonic, but also super-Alfvénic. The number density is very low, of the order of 15 particles cm^{-3} .

The fast SW has lower densities by about one third, similar electron temperatures but much higher proton and α -particle temperatures, by a factor of 4.

Close to the Sun, the atmosphere can be approximated quite well to first order with a hydrostatic solution, which predicts that the density falls off exponentially with an hydrostatic scale height $H = RT/\mu g$. The approximate exponential drop off in density has been confirmed by observations. The very low density close to the Sun means that at just two solar radii the plasma is not collisionally dominated, i.e., the electrons and protons do not exchange sufficient energy to thermalise. As a consequence, electrons and protons can have very different temperatures. Considering a 2-fluid plasma composed of electrons and protons, it is expected that the proton temperature would decrease much faster than the electron temperature, given that the thermal conduction for the electrons is about $(m_p/m_e)^{1/2} \simeq 50$ times larger. The first two-fluid model of the solar wind, by Sturrock and Hartle (1966), produced T_e quite close to the observed values at 1 AU, but T_p was about an order of magnitude lower than observed. The predicted plasma velocity was about 250 km/s at 1 AU.

Clearly, the simple thermal expansion idea from Parker was able to explain the gross properties of the solar wind, but in reality there must be some acceleration processes that increase the velocity of the particles and heat them (in particular the protons). The situation is even more complex in the case of the high-speed component which cannot be explained by Parker's model.


The presence of a high-speed solar wind creates compression regions corotating with the Sun, as slow and fast wind streams originating from the same solar latitude, but from different longitudes interact dynamically.

The discovery of Alfvén waves appeared to provide a way to solve the problem of the heating and acceleration of the solar wind. Belcher and Davis (1971) used data from Mariner 5 to

show that for a large fraction of the time Alfvén waves are present and dominate the microscale structure of the wind, in particular of the high-speed one. The waves are of large amplitude and propagate outwards from the Sun, with long periods (hours). They have energy densities comparable both to the unperturbed magnetic field energy density and to the thermal energy density. Wave-driven wind models started to be constructed, by including a wave pressure and dissipation/plasma heating. These models were successful in explaining the fast solar wind, but only far from the Sun. Subsequent models assumed that close to the Sun Alfvén waves of high frequencies are created, which in turn would preferentially heat the protons via the cyclotron resonance (when the wave frequency matches the cyclotron frequency). According to these models, the solar wind would mainly be driven by the hot protons. Details and references can be found in a recent review by Hollweg (2008).

The solar wind is a highly turbulent medium. For a review of the observational and theoretical aspects, see the *living review* by Bruno & Carbone (2005). One major new findings from the SoHO UVCS spectrometer was the very large widths in the H I and O VI lines above coronal holes. By assuming that nonthermal broadening due to waves or turbulence is negligible, very large ion temperatures were found. For example, 3×10^8 K at $3.5 R_{\odot}$ from O VI. Many authors now regard these measurements as proof that preferential heating due to ion-cyclotron resonance is occurring, however more measurements of different ions would be needed to confirm this, and a theory of how high-frequency Alfvén waves can be generated close to the Sun needs to be developed. For observational aspects, see the review by Kohl et al. (2006), while for theoretical considerations see the *living review* by Marsch (2006).

10.3 The Sources of the Solar Wind

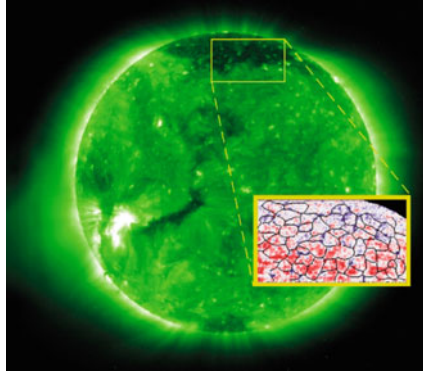
Coronal holes as the source of the fast solar wind was first established from Skylab X-ray observations and in-situ measurements by Krieger et al. (1973). This is now well-accepted. Doppler measurements by SoHO/SUMER clearly show blueshifted emission in coronal holes at the network boundaries (see, e.g., Hassler et al. 1999, and  Fig. 3-78), confirming the source of the fast solar wind.

Whether or not coronal hole plumes and jets contribute to the fast solar wind is still a matter of hot debate. Opposite arguments, mainly based on SoHO and Hinode observations, have been put forward. The difficulty lies in mapping back the in situ measurements, mainly velocities and magnetic fields, onto the Sun's surface.

It is still not entirely clear where the slow SW originates from. Many believe that comes from the boundaries between coronal holes and large streamers that undergo strong super-radial expansion in the corona, while others believe that it comes from narrow plasma sheets that extend out from the tops of streamer cusps.

One major contribution from the SoHO LASCO coronagraph has been the finding of the continuous large number of *bubbles* leaving the lower corona all the time. The plasmoids are observed to accelerate to an average velocity of about 300 km/s between 5 and $25 R_{\odot}$. The average velocity profile is consistent with an isothermal solar wind at 1.1 MK and a sonic point near $5 R_{\odot}$, in good agreement with the simple original Parker's model.

LASCO has also shown that CMEs provide an important contribution to the solar wind (in terms of mass and magnetic field), in particular during high solar activity, when many CMEs occur per day. During minimum conditions, the rate of CME production is about one order of magnitude lower.



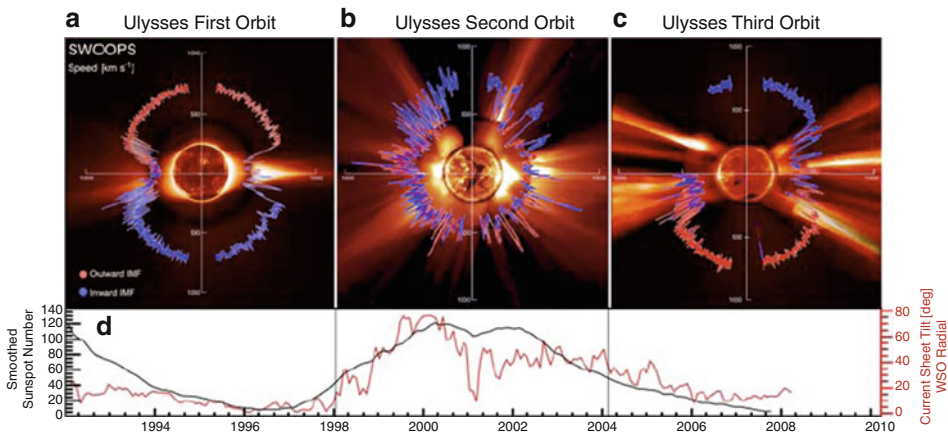
■ Fig. 3-78

The polar coronal hole regions show blueshifted emission in Ne VIII (formed around 0.6 MK) as observed by SoHO SUMER (Hassler et al. 1999). The image is from the SoHO EIT broadband at 195 Å, while the inset shows a Doppler velocity map from SoHO SUMER with superimposed the boundaries of the supergranular network (Image courtesy of D. Hassler)

10.4 Ulysses

Ulysses encountered the fast SW streaming out from the polar holes in 1992–1993. It crossed the south pole in June–November 1994 and the north pole in June–September 1995. During this time, the Sun was in solar minimum conditions for cycle 22. Extended polar coronal holes were present and symmetric, well-defined, streamers were present. Ulysses showed that the solid angle occupied by the fast SW is much larger than the solid angle occupied by the coronal hole at the solar surface, an indication of super-radial expansion. It also showed that the heliospheric magnetic field was mainly symmetric and dipolar. Pressure-balance (a decrease of magnetic pressure balanced by an increase of plasma pressure) structures were observed in the fast SW and were interpreted as the interplanetary manifestations of polar plumes.

Contrary to expectations, and Parker's model, the radial magnetic field strength was found to be nearly constant with latitude. Indeed the magnetic flux density $r^2 B_r$ was found to be constant with latitude by Ulysses. Ulysses clearly showed that the magnetic field embedded in the fast solar wind originates in coronal holes and fills over 60% of the heliosphere near solar minimum. Ulysses performed its second polar pass during the rise and peak phase of the solar maximum for cycle 23. It showed a complex, highly variable structure at all heliolatitudes, composed of flows arising from different sources (streamers, coronal mass ejections, coronal holes, and active regions). Ulysses has also provided important chemical abundance measurements, discussed in the abundance section, and empirical constraints on the temperatures at the freezing-in radius. The freezing-in radius is the distance from the Sun center where the expansion time of the solar wind equals the exchange time between the ions. Various assumptions have to be made, in order to deduce these kinds of temperatures, e.g., the expansion model, the charge state distribution, the elemental abundance, the distribution function of the electrons, the relative flow speeds of the different charge states. Different values are present in the literature. For many years, it seemed that a large discrepancy between results from the in situ and the remote-sensing observations was present, with the freezing-in temperatures being 2–3 times larger. Gloeckler and Geiss (2007) have recently re-evaluated Ulysses SWICS measurements to



■ Fig. 3-79

Polar plot of the solar wind speed as a function of heliographic latitude observed by Ulysses during the two/three polar passes during minimum and maximum (From McComas et al. 2008)

find a freezing-in temperature in fast SW from coronal holes of only 1.1 MK, in relatively good agreement with recent remote-sensing measurements at the base of the corona (cf. Del Zanna et al. 2008). The plasma freezing-in temperature, calculated from the observed O^{7+}/O^{6+} ratio by Ulysses, correlates well with the solar wind speed, confirming that the fast SW originates in low-temperature regions of the corona.

Another important result from Ulysses is that, unexpectedly, the number of GCRs measured did not increase at higher latitudes. A North-South asymmetry in the radial field component, with the field being stronger in the South was another key discovery. These types of asymmetries have recently received a great deal of attention, because they might be related to the overall change in the heliosphere which started around 2004, just after the last peak of activity (2001–2002). The polar fields also appear to be significantly lower than expected.

Ulysses completed a third polar pass during its third orbit in 2007. Preliminary results are presented in McComas et al. (2008) (see Fig. 3-79). The last pass showed that the fast solar wind occupied a much reduced solid angle, compared to the previous minimum conditions, where the heliospheric magnetic field was closer to dipolar. The third orbit also showed that the fast wind was slightly slower and significantly less dense and cooler, when compared to the 1996 solar minimum. This resulted in much lower dynamic (by 22%) and thermal (by 25%) pressures. The significant, long-term trend toward lower dynamic pressures means that the heliosphere has been shrinking. This could possibly be the cause of the early crossings of the termination shock by Voyager 1 in 2004 and Voyager 2 in 2007. After more than 18 years of operation, the Ulysses mission terminated on June 30, 2009.

11 Solar Irradiance

11.1 Introduction

No one can deny the crucial influence that the Sun has on the Earth's climate. The total amount of solar radiation reaching unit area of the Earth's atmosphere is called the total solar

irradiance (TSI). The TSI is the main heating input to our climate, and directly affects the surface temperatures, given that the bulk of the photons are emitted at visible wavelengths, hence are not significantly absorbed by the atmosphere.

The solar irradiance is of particular importance for the study of the Sun as a star, since it is the only case where detailed information about the distribution of the sources on its surface is available. Hence, it is the only case where predictions of the irradiance can be tested in detail. The only drawback is the fact that all the measurements to date have been done within the ecliptic.

The variations in the solar influence on our planet are not simply due to inherent variations in solar energy. Actually, significant variations in solar forcing on our planet are due to the Milankovitch cycles, i.e., changes in the eccentricity ($\sim 100,000$ years), the obliquity (angle between the equator and the orbital plane) ($\sim 40,000$ years) and the precession of the Earth's axis ($\sim 20,000$ years).

Aside from the total solar irradiance, there are three other key mechanisms which might impact the Earth's climate: (1) Solar UV and X-ray irradiance, which directly affects the temperature and composition of the upper and middle atmosphere (e.g., the amount of Ozone). Changes in UV, X-ray, and total solar irradiance vary in phase with the 11-year solar cycle. When the Sun is active, there is higher solar irradiance, with large increases in UV and X-ray emission. (2) Solar energetic particles, which ionize constituents of the middle and upper atmosphere, affecting atmospheric chemistry and temperature. (3) Galactic cosmic rays, which ionize constituents of the lower atmosphere and may thereby seed the formation of clouds.

The linkages between total solar irradiance (the dominant mechanism) and climate are included in climate models, but the other three mechanisms are generally not included. Some models do include changes in UV, but not the associated effects on atmospheric chemistry. It is important that sophisticated, integrated models are developed, in order to fully understand and predict the complex interaction between the Sun and the Earth.

11.2 Total Solar Irradiance, TSI, and Surface Temperature

The TSI was once known as the solar constant. It has been measured on the ground for a long time. An extensive set of measurements were obtained by Langley and others (Smithsonian Institution of Washington) from 1902 until the 1960s, with an averaged value of $1,353 \text{ W m}^{-2}$. Large (50% or so) corrections due to atmospheric absorption are required, and therefore some uncertainties are present.

More accurate measurements have been carried out with instruments in space. The Earth Radiation Budget (ERB) cavity instrument on board the NASA Nimbus satellite, launched in 1978, started to obtain irradiance measurements from space. The Active Cavity Radiometer Irradiance Monitor (ACRIM) instrument aboard SMM provided data between 1980 and 1989. These instruments were very precise and detected variations on all timescales, from daily ones of 0.01% or so, to weekly ones of up to 0.25%, and long-term ones of about 0.15% along the solar cycle [see Fröhlich and Lean (2004) for a review of measurements of the solar irradiance]. It soon became clear that the dips in the total irradiance which lasted a few days were related to the meridian passage of large Sunspot groups. On the other hand, general variations are due to a fine balance between the decrease in irradiance due to cooler (darker) emission in Sunspots and the bright UV emission in plage/faculae areas. One interesting fact is that the areas covered by

faculae vs. sunspots grows with activity relative to sunspots. It is still unclear how this relation applies to active stars.

Many other instruments have measured the TSI, including the Earth Radiation Budget Experiment (ERBE), the Upper Atmosphere Research Satellite (UARS), the European Retrievable Carrier (EURECA), the SoHO VIRGO (with two instruments), ACRIMSAT, and most recently the Solar Radiation and Climate Experiment (SORCE), with the Total Irradiance Monitor (TIM).

☛ *Figure 3-80* (left) shows a composite of some of the measurements. The Nimbus, SMM, and UARS data were obtained from the US National Geophysical Data Center at NOAA. The SoHO VIRGO data are the version 2, which includes various corrections for instrument degradation. They were obtained from PMOD/WRC, Davos, Switzerland. The SORCE/TIM data were obtained from the instrument database. Large uncertainties in the absolute value of the solar constant exist, given that over the last 30 years there has been a large scatter of values. The latest measurements from SORCE are not consistent with previous ones but are thought to be the most accurate, providing a value of about 1361 W m^{-2} during the period of low solar activity in 2007–2009. The long-term trends due to the solar cycle are evident. ☛ *Figure 3-80* (right) shows a composite of the TSI values. It seems that the latest minimum was significantly lower than previous ones (Fröhlich 2009).

Further measurements will be obtained in the future. For example, PICARD is a new space mission dedicated to simultaneous measurements of the solar diameter, and of the spectral and total solar irradiance.

The issue as to whether the characteristics of the regions of the Sun with small magnetic field density are changing with the cycle is a complex one. Radiance measurements from space in the EUV and UV suffer from instrument calibration issues. Ground-based measurements of equivalent widths (EW) are independent from radiometric calibration issues, hence are very reliable. The EW of photospheric and chromospheric lines (e.g., Ca II) over the “quiet Sun” (often Sun center) have not changed over the last three solar cycles (Livingston et al. 2007), thus providing evidence that the basal photospheric–chromospheric emission has been relatively constant over this period.

In the last decade, some effort has gone into modeling the solar irradiance. The reasons are twofold. One goal is to provide reliable input to climate models. Currently, most climate models use various proxies for the solar activity and some use averaged spectral irradiances. Another goal is to model the effects of the magnetic activity in young stars (including the young Sun) on planets. Recently, there has been particular interest in predicting the environment in which young planets were formed. The strong UV and EUV irradiance in young stars is an important factor for the development of life. The same is true for the Sun.

Models of solar irradiance are inherently semiempirical and have large uncertainties, given that are based upon a large number of assumptions and indirect measurements (i.e., on proxies of solar activity). One proxy widely used is the *sunspot number*. In fact, records of sunspots exist from the early seventeenth century, for example, from Galileo Galilei. This sunspot proxy is rather crude, given that various visibility effects are present (see, e.g., Dalla et al. 2008; Maunder 1907). ☛ *Figure 3-81* (top) shows the Group Sunspot Number, obtained by Hoyt and Schatten (1998) from a vast collection of archival data.

For a recent example of irradiance reconstruction see, e.g., Krivova et al. (2007), who estimated, based on the ideas developed by Solanki et al. (2002), the total irradiance since 1611 using the Group Sunspot Number. The data are displayed in ☛ *Fig. 3-81* (middle). Many such reconstructions exist in the literature, each differing in some respect. Large uncertainties are

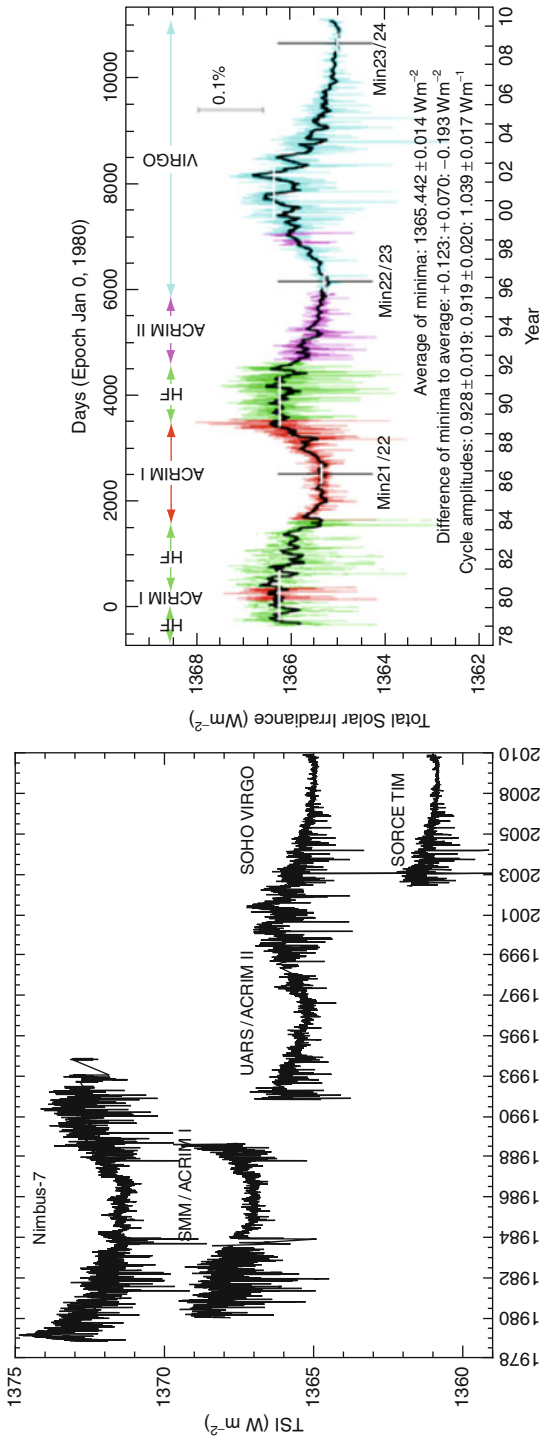
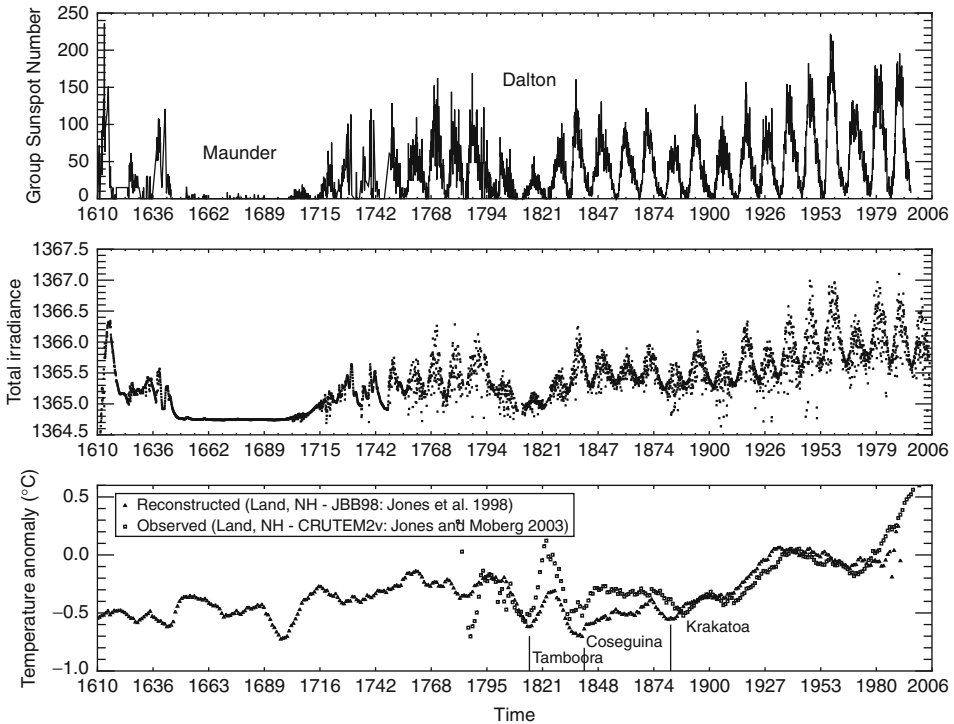


Fig. 3-80 Absolute measurements of the total solar irradiance (TSI) from various satellites (left). A composite normalized TSI, courtesy of PMOD/WRC, Davos, Switzerland (right)



■ Fig. 3-81

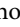
Top: the Group Sunspot Number, indicating the level of solar activity since 1611. The long-term Maunder minimum is evident, as well as the shorter Dalton minimum. **Middle:** reconstructed total solar irradiance, from Krivova et al. (2007) (data have been smoothed). **Bottom:** temperature anomaly (data have been smoothed), observed (land, northern hemisphere), and reconstructed (land, northern hemisphere). The timings of large-scale volcanic eruptions (Tambora, Coseguina and Krakatoa) are also shown

present, in particular for the early years. However, all reconstructions predict a modest variation in TSI in the last 400 years.

It has been suggested (cf. Eddy 1976) that a relation exists between total solar irradiance and surface temperatures in the northern hemisphere. The most famous example is the Maunder Minimum in sunspot numbers, which occurred during the second half of the seventeenth century, and coincided with a period, known as the *Little Ice Age*, during which temperatures in the Northern Hemisphere (Europe in particular) were exceptionally low.

Direct surface temperature measurements are available only from the late nineteenth century. However, various proxies are used to estimate surface temperature variations, all with a significant degree of uncertainty, given that temperature variations are not the sole driving factor. Among the various methods, one uses tree rings. Another method is to look at isotopic concentrations in ice cores, obtained from Greenland and Antarctica. Another method uses sedimentary deposits.

🔍 **Figure 3-81** (bottom) shows the variation in a set of observed and reconstructed temperatures. The observed ones are land-only summer temperatures for the northern hemisphere

(latitudes between 20° and 90°) from Jones and Moberg (2003). The reconstructed ones are land temperatures for the northern hemisphere obtained by Jones et al. (1998). The temperatures are displayed as “anomaly”, i.e., as the variation with respect to the average temperatures recorded during the 1961–90 period. The data were obtained from the Fourth Assessment Report (AR4) of the Working Group 1 on paleoclimate, for the Intergovernmental Panel on Climate Change (IPCC). The timings of large-scale volcanic eruptions (Tamboora, Coseguina and Krakatoa), known to cause short-term global decreases in temperature, are also shown in  Fig. 3-81.

As is the case of TSI reconstructions, a number of temperature reconstructions exist, all differing quite significantly. However, some correlation between solar activity and surface temperatures appears to exist. However the recent global warming, the sharp rise in the Earth's surface temperature over the past 50 years, cannot be explained by the Sun's influence. The solar irradiance, although varying with the solar cycle over the past 50 years, has increased but not dramatically. The vast majority of scientists are convinced that global warming is man-made and is due to the increase in the amount of “greenhouse gases” in the Earth's atmosphere.

One major problem in accepting a link between total solar irradiance and surface temperatures has been the fact that global temperatures show little correlation, and that the forcing due to the small irradiance variations is too small to have a direct effect. However, there is ample evidence for solar forcing on global circulation patterns and pressures (e.g., the North Atlantic Oscillation (NAO) which has a strong influence on the climate of Northern Europe), and there is growing consensus that even a small variation of the solar energy output could produce significant effects on some local climate patterns. For a review of some of these issues, see, e.g., Haigh (2007).

One interesting question is whether the Sun's variability on long timescales is peculiar or not. This issue is not yet resolved. Baliunas and Jastrow (1990) used the Mount Wilson Ca II H&K survey on what was believed to be a good sample of solar analogs, to find that a significant number of K,G stars had activity levels significantly below that of the Sun at solar minimum. Some of the findings have been subsequently questioned; however, it is quite evident that cycle variations are present in many stars. One puzzling issue is that a large number of stars have not shown cyclic variations so far. Stars that have cyclic variations are generally more active. One problem with the use of Ca II H&K observations is that the excess flux in the cores of these absorption lines only varies by small (10% or so) amounts during the solar cycle, and it decreases with stellar age, hence it is not a very sensitive proxy. Much better proxies would be fluxes in the EUV and X-rays, however most observations (e.g., ROSAT) have been carried out in broadbands, which, even in the X-rays, can be contaminated by emission formed in very different atmospheric layers.

A significant amount of data are now available since 1999 from the XMM-Newton and Chandra X-ray missions, and a more complete picture of stellar variability in the X-rays will become available. Missions such as Kepler, Corot, GAIA are going to give a substantial contribution with more accurate measurements of stellar characteristics (e.g., age, size, mass, rotation), so more detailed comparative studies with the Sun as a star will be possible.

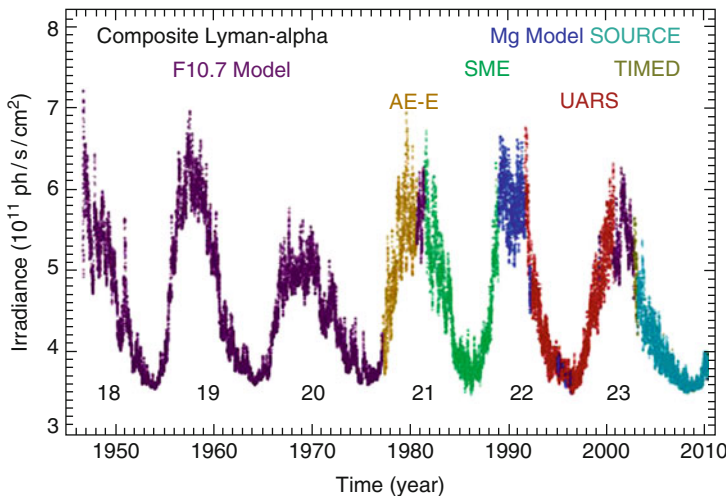
It is also possible to look back in time and see if the past few centuries were typical or not. This is done by using cosmogenic isotopes as proxy indicators of past variations in solar irradiance on long timescales. These isotopes are spallation products of galactic cosmic rays (GCRs) impacting Earth's atmosphere, and then absorbed and deposited into e.g., ice sheets, tree rings etc. The number of GCRs is strongly reduced during periods of solar activity, given that the heliospheric magnetic fields act as a shield. Therefore, GCRs are actually a proxy of heliospheric magnetic fields and not directly of the photospheric ones which modulate the solar irradiance.

The cosmogenic isotopes ^{10}Be (polar ices) and ^{14}C are mostly used. Their variations follow to some degree the long-term variations in solar activity (e.g., Sunspot numbers), and the Maunder minimum is clearly visible. The records show that Maunder-like minima have occurred quite frequently. See, e.g., Beer et al. (2006) for a recent review based on ^{10}Be measurements. The ^{10}Be records also show that the Sun has been unusually active in the last 50 years or so, although this is not uncommon within the last 10,000 years (see, e.g., Abreu et al. 2008). The increased solar activity in the last 50 years has led to suggestions that global warming could also be related to the Sun's activity. However, anthropogenic forcing remains the dominant effect.

11.3 Irradiance in the UV

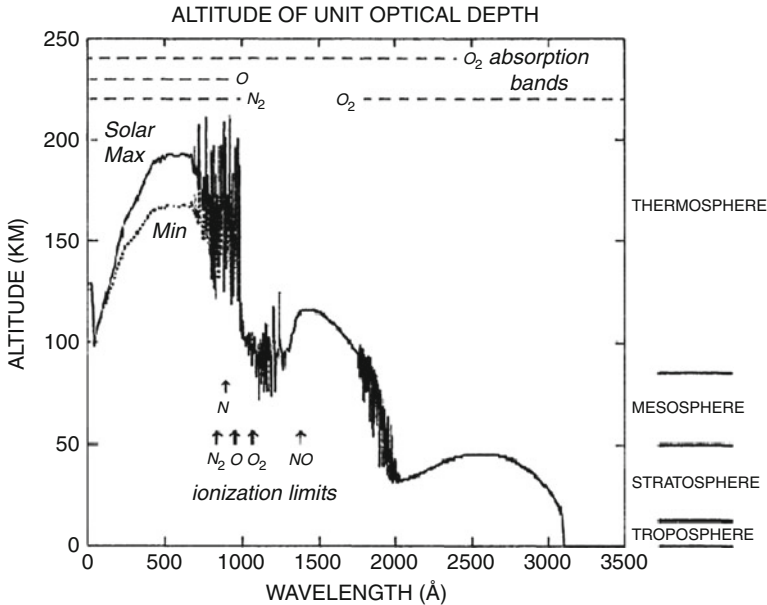
Variations with the solar cycle occur at all wavelengths and are up to 20%, depending on which UV wavelength is considered. The neutral hydrogen Ly- α is by far the strongest transition in the UV. It is mainly absorbed in the upper mesosphere. The neutral hydrogen Ly- α varies significantly (see Woods et al. 2000), as [Fig. 3-82](#) shows.

UV light controls the amount of stratospheric ozone through a series of reactions. The most important one is the photodissociation of O_2 , which occurs at wavelengths less than 2420 Å in the stratosphere (cf. [Fig. 3-83](#)). The oxygen atoms then react with oxygen molecules to produce ozone molecules. Various other processes are at work, at different heights in the atmosphere, the net effect being a peak in ozone around 25 km in equatorial regions. Stratospheric ozone abundance increases during periods of higher solar activity, although other effects such as global circulation and energetic particles change its abundance. Energetic particles from cosmic rays or from solar events such as flares or CME tend to reduce on short timescales the ozone abundance. The ozone concentration, among other parameters, is predicted to have important



■ Fig. 3-82

A composite of the irradiance in the neutral hydrogen Ly- α , courtesy of the Laboratory for Atmospheric and Space Physics, University of Colorado in Boulder



■ Fig. 3-83

Unity optical depth of the atmosphere for absorption of the incoming solar radiation, as a function of altitude (Meier 1991)

effects on global climate, as simulations show (see Haigh 1996, 2007). The processes are highly nonlinear and are complex to model.

The Solar Stellar Irradiance Comparison Experiment (SOLSTICE) and the Solar Ultraviolet Spectral Irradiance Monitor (SUSIM) on UARS have been providing UV measurements of the UV spectral irradiance since 1991. Solar Mesosphere Explorer (SME) also monitored the UV irradiance from 1981 until 1989. The Solar EUV Experiment (SEE) aboard the Thermosphere, Ionosphere, Mesosphere, Dynamics, and Energetic (TIMED) satellite, have made measurements since 2002.

Broad-band measurements have also been done, recently by Lyra aboard Proba2, which measures the UV irradiance in 4 UV passbands. Variations on all timescales have been observed, from short ones due to flares to those lasting a few days and related to the meridian passage of solar features. Plage areas are much brighter than sunspots in the UV, compared to the difference in the visible, which explains why larger variations are observed. How such variations produce some effect – however small – on Earth's climate is still unclear. The same applies to the EUV radiation.

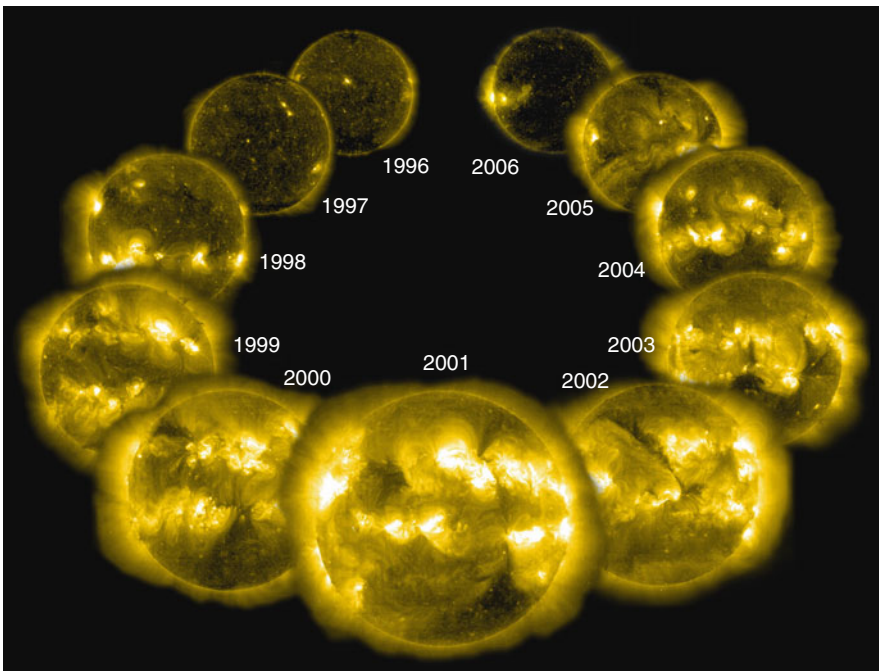
11.3.1 Irradiance in the EUV and X-rays

Some effects of the EUV radiation on Earth's atmosphere – particularly on the Thermosphere – are well known. The solar EUV radiation is the dominant factor in the formation of our ionosphere via photoionization and molecular photo-dissociation. EUV photons with wavelengths shorter than the neutral hydrogen Ly- α are absorbed in the Thermosphere and are

those which ionize neutral oxygen and N_2 , as well as O_2 and other molecules. Variations in the EUV irradiance directly affect the density of the ionosphere and have a significant impact on satellite drag.

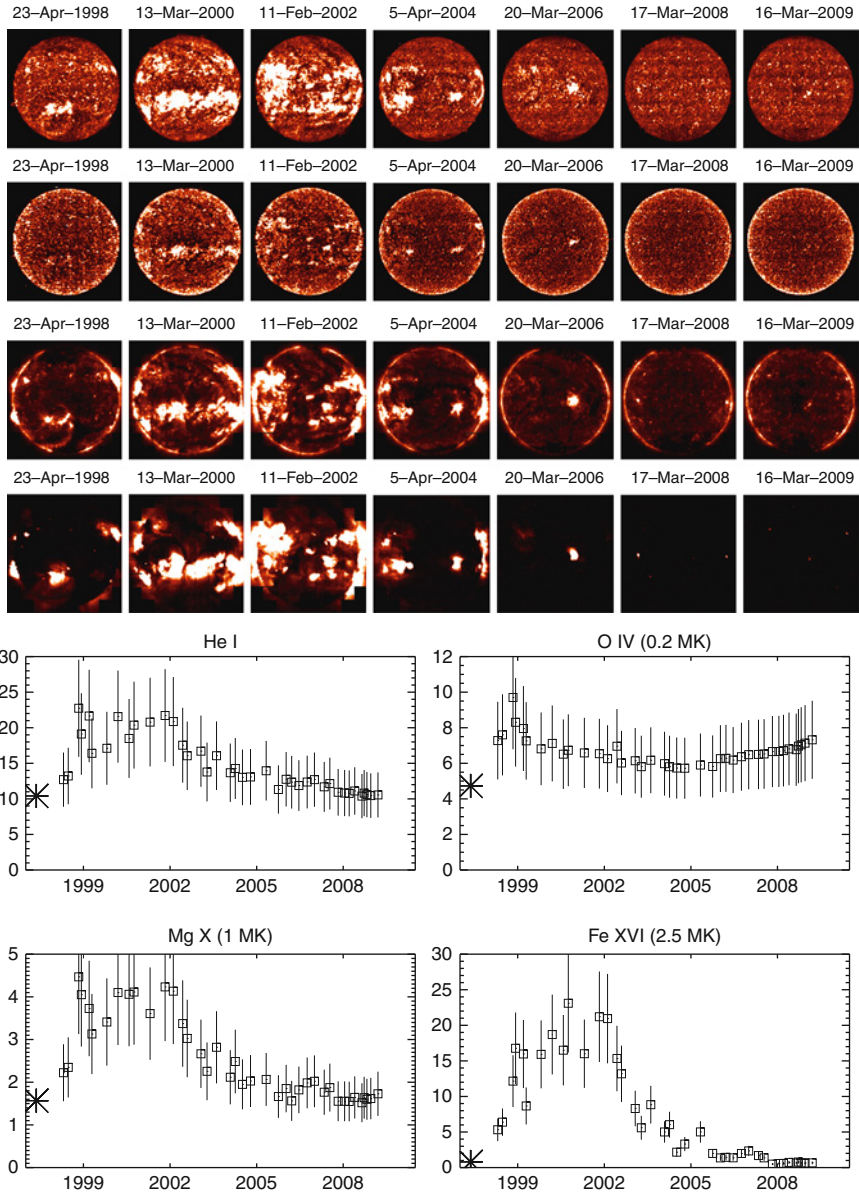
Only a few measurements are available, from occasional sounding rockets, which give only a snapshot of the solar irradiance, or cover less than one solar cycle or partial spectral ranges. Continuous measurements have only been carried out since 2002 with the NASA TIMED SEE experiment, that has provided EUV spectra with a coarse spectral resolution.

SoHO has been observing the Sun since 1996. Apart from the broadband measurements of EIT (see ● Fig. 3-84) and the CELIAS/*Solar Extreme Ultraviolet Monitor* (SEM), the Coronal Diagnostics Spectrometer (CDS) has been routinely observing the full solar disc in the ranges 31–38 and 51.5–63 nm with its *Normal Incidence Spectrograph* (NIS). The CDS instrument has been radiometrically calibrated using sounding rockets and by studying the long-term trends in the quiet Sun radiances. The calibrated radiances have been converted to irradiances (Del Zanna and Andretta 2010). Lines formed in the low transition region show relatively modest changes (by 50% at most). Lines forming around 1 MK change during the cycle by a factor ~ 5 ; for hotter lines (2.5 MK) the variability reaches factors of the order of 40 (see ● Fig. 3-85). The presence of active regions during the solar cycle has a strong influence even in regions of the more “quiet corona” which change considerably with the cycle, in particular for lines formed above 1 MK.



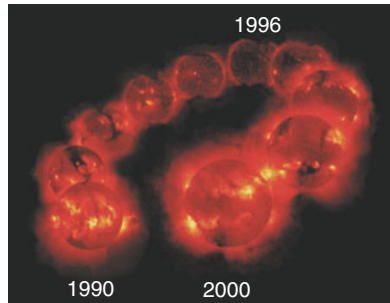
■ Fig. 3-84

SoHO EIT images in the 284 Å band, which is dominated by active region emission at 3 MK during periods of high solar activity (Courtesy of the SoHO/EIT consortium and Steele Hill (NASA GSFC))



■ Fig. 3-85

SoHO CDS radiances and irradiances in a selection of emission lines (Adapted from Del Zanna and Andretta 2010) from 1998 until 2009. The *top* images correspond to He I, O IV, Mg X, Fe XVI emission and each row has the same intensity scale. The *bottom* plots show the SoHO CDS irradiances in the same lines



■ Fig. 3-86

Yohkoh SXT X-ray images during one solar cycle, from maximum (1990) to minimum (1996) and last maximum (2000)

The extreme ultraviolet variability experiment (EVE) on board the NASA Solar Dynamics Observatory (SDO), the first mission of the NASA Living With a Star (LWS) programme, is measuring the solar EUV irradiance from 1 to 1050 Å with medium spectral resolution (1 Å) and high temporal cadence (10 s).

Many observations in the XUV have been done with photometers or broadband instruments; hence no calibrated irradiance measurements are available, in contrast with the stellar case where spectroscopic observations from Chandra and XMM-Newton are available since 1999. The solar observations include X-ray Sensors (XRS) aboard the NOAA GOES spacecrafts, the SoHO solar EUV monitor (SEM), the solar XUV photometers (SXP) on the Student Nitric Oxide Explorer (SNOE). X-ray broad-band images from Yohkoh SXT obtained in the 1990s (see ● Fig. 3-86) showed variability by two orders of magnitude.

12 Future Prospects

The future couple of decades offer an exciting prospect for solar physics. Various new satellites are being proposed and built. A follow-up of the successful Solar-A (Yohkoh) and Solar-B (Hinode) is being proposed. New missions to probe the inner heliosphere are being designed: the Russian InterHelios and the ESA-NASA Solar Orbiter satellites will go close to the Sun and above the ecliptic. The NASA solar Probe+ will go even closer to the Sun.

Besides the new observatories, many smaller rockets and SMEX (small explorer missions) are planned. The level of detail we shall be able to measure and see in the solar atmosphere continues to increase dramatically. The challenge is for the theory and models to keep up with these observations. Increases in the size and capacity of computers helps in this regard, but the modeling codes (MHD, kinetic, hydrodynamic etc.) require faster and larger processors. To date many codes have been developed independently, but the theoretical challenge is to bring all these codes (MHD + kinetic theory + hydrodynamic processes) together. This is likely to need the modeling of nonequilibrium processes (non-Maxwellian velocity distributions, two fluid models, time-dependent ionization and recombination, radiative transfer in the lower atmosphere).

The great challenge as always in solar physics is to keep pace with the complexity of the observations, to develop new theoretical techniques to accurately model the phenomena which

the Sun exhibits. The Sun, our nearest star, does not make this challenge easy. However, unless we can understand the physics of the Sun we have little chance of understanding the complex processes in other stellar atmospheres. Observations of other stars do however also provide a spectrum of stellar conditions in which we can place the Sun. In this regard, studies of the Sun and other stars go hand-in-hand.

12.1 Solar Orbiter

Solar Orbiter is one of ESA's candidates for a medium-class mission part of the Cosmic Vision programme to be launched no earlier than 2017. The orbit of the Solar Orbiter is unique in that it is highly elliptical with perihelion as low as 0.23 AU and with increasing inclination up to more than 30° with respect to the solar equator over the years, obtained with Venus flybys. This is technically very challenging, in particular with the temperature extremes which will be experienced.

The main goal of Solar Orbiter is to address the following questions:

- What are the origins of the solar wind streams and the heliospheric magnetic field?
- What are the sources, acceleration mechanisms, and transport processes of solar energetic particles?
- How do coronal mass ejections evolve in the inner heliosphere?
- Explore, at all latitudes, the energetics, dynamics, and fine-scale structure of the Sun's magnetized atmosphere.

This will be achieved with a suite of instruments, built in collaboration with NASA. The primary ones will be the in situ ones, which will measure the solar wind close to the Sun, a fundamental requirement. The main advantages over previous missions are: close-up view point; out-of-ecliptic view point; near corotating orbital phases; multi-point in situ observations by Solar Orbiter and Solar Probe Plus. The close-up view point will provide unprecedented spatial resolution, although it should be noted that the same could be achieved by Earth-orbiting satellites. The key advantage is the near corotating orbital phases, i.e., it should be possible to relate the in situ measurements with the sources, as observed with remote sensing (EUV imaging and spectroscopy). A coronagraph will provide unprecedented details about the inner corona.

12.2 Solar Probe+

The Solar Probe+, now scheduled for launch in 2015, is a modification of a previous NASA mission. It is designed to approach the Sun as close as 8.5 radii from its surface with a number of flybys over a period extending over both solar minimum and solar maximum. The mission will be highly complementary to Solar Orbiter and will make measurements of the solar wind plasma within its birthplace. Its baseline payload is an integrated package of in situ instruments and a white-light Hemispheric Imager (HI) for imaging coronal structures. Its scientific goals are similar to the Solar Orbiter ones:

- To determine the structure and dynamics of the magnetic fields at the sources of the solar wind.
- To trace the flow of energy that heats the corona and accelerates the solar wind.

- To determine what mechanisms accelerate and transport energetic particles.
- To explore dusty plasma near the sun and its influence on solar wind and energetic particle formation.

A quote from E.N.Parker, the father of the solar wind:

- ▶ *"It is ironic that voyaging spacecraft have roughed out the general picture of the solar wind region—the heliosphere—with its spiral magnetic field and the fast and slow stream interaction regions all the way out to the termination shock at 100 AU, while the heat sources that create the wind are still poorly understood. We expect that the coronal heating is a complex phenomenon, different over the quiet and active regions of the Sun. The ideal space mission to explore this problem would involve detailed in-situ investigation of plasma temperature, composition, and bulk motion; fast particle populations; magnetic field; and wave motions from the base of the corona out to 1 AU at many locations around the Sun at times of both high and low activity. Such a space mission is impossible, of course, because the Sun, being a star, is not readily approachable, but we would like to approach it as closely as money and technology permit."*

References

- Abreu, J. A., Beer, J., Steinhilber, F., Tobias, S. M., & Weiss, N. O. 2008, *Geophys Res Lett*, 35, 20109
- Anders, E., & Grevesse, N. 1989, *Geochim. Cosmochim. Acta*, 53, 197
- Andretta, V., Del Zanna, G., & Jordan, S. D. 2003, *A&A*, 400, 737
- Andretta, V., Mauas, P. J. D., Falchi, A., & Teriaca, L. 2008, *ApJ*, 681, 650
- Antiochos, S. K. 1998, *ApJ*, 502, L181
- Antonucci, E., et al. 1982, *Sol Phys*, 78, 107
- Aschwanden, M. 2006, *Physics of the solar corona*. (Chichester, UK: Praxis Publishing Ltd)
- Asplund, M., Grevesse, N., Sauval, A. J., & Scott, P. 2009, *ARA&A*, 47, 481
- Athay, R. G., eds. 1976, *The Solar Chromosphere and Corona: Quiet Sun, Astrophysics and Space Science Library*, Vol. 53 (Dordrecht: Reidel Publishing Co.)
- Athay, R. G., & Thomas, R. N. 1961, *Physics of the Solar Chromosphere* (New York: Interscience Publishers)
- Babcock, H. W. 1961, *ApJ*, 133, 572
- Badnell, N. R., Bautista, M. A., Butler, K., Delahaye, F., Mendoza, C., Palmeri, P., Zeippen, C. J., & Seaton, M. J. 2005, *MNRAS*, 360, 458
- Baliunas, S., & Jastrow, R. 1990, *Nature*, 348, 520
- Balogh, A., Lanzertotti, L. J., & Suess, S. T. 2008, *The Heliosphere Through the Solar Activity Cycle* (New York, NY: Springer-Praxis Books and Springer Science+Business Media)
- Balogh, A., Marsden, R. G., & Smith, E. J. 2001, *The Heliosphere Near Solar Minimum. The Ulysses Perspective* (Springer-Praxis books in Astrophysics and Astronomy)
- Basu, S., & Antia, H. M. 2004, *ApJ*, 606, L85
- Basu, S., & Antia, H. M. 2008, *Phys. Rep.*, 457, 217
- Beer, J., Vonmoos, M., & Muscheler, R. 2006, *Space Sci Rev*, 125, 67
- Belcher, J. W., & Davis, L., Jr. 1971, *J Geophys Res*, 76, 3534
- Benz, A. O. 2008, *Living Reviews in Solar Physics*, 5, 1
- Biermann, L. 1951, *Zeitschrift für Astrophysik*, 29, 274
- Bochsler, P. 2007, *A&A Rev.*, 14, 1
- Bradshaw, S. J. 2008, *A&A*, 486, L5
- Bradshaw, S. J. 2009, *A&A*, 502, 409
- Bradshaw, S. J., & Mason, H. E. 2003, *A&A*, 401, 699
- Braun, D. C., & Birch, A. C. 2008, *Sol Phys*, 251, 267
- Brown, J. C. 1971, *Sol Phys*, 18, 489
- Bruno, R., & Carbone, V. 2005, *Living Reviews in Solar Physics*, 2
- Burgess, A. 1964, *ApJ*, 139, 776
- Burgess, A. 1965, *ApJ*, 141, 1588
- Burgess, A., & Summers, H. P. 1969, *ApJ*, 157, 1007
- Burton, W. M., Jordan, C., Ridgeley, A., & Wilson, R. 1971, *Philos Trans R Soc Lond A*, 270, 81
- Butler, R. P., Vogt, S. S., Marcy, G. W., Fischer, D. A., Henry, G. W., & Apps, K. 2000, *ApJ*, 545, 504
- Cargill, P. J. 1994, *ApJ*, 422, 381
- Carlsson, M., & Stein, R. F. 1997, *ApJ*, 481, 500
- Carrington, R. C. 1859, *MNRAS*, 20, 13
- Chamberlin, P. C., Woods, T. N., Crotser, D. A., Eparvier, F. G., Hock, R. A., & Woodraska, D. L. 2009, *Geophys Res Lett*, 36, 5102
- Charbonneau, P. 2005, *Living Reviews in Solar Physics*, 2

- Chifor, C. 2008, PhD thesis. Univ. of Cambridge, UK
- Chifor, C., Del Zanna, G., Mason, H. E., Sylwester, J., Sylwester, B., & Phillips, K. J. H. 2007, *A&A*, 462, 323
- Christensen-Dalsgaard, J. 2002, *Rev Mod Phys*, 74, 1073
- Claverie, A., Isaak, G. R., McLeod, C. P., van der Raay, H. B., & Cortes, T. R. 1979, *Nature*, 282, 591
- Cowling, T. G. 1941, *MNRAS*, 101, 367
- Craig, I. J. D., & Brown, J. C. 1976, *A&A*, 49, 239
- Culhane, J. L., & Jordan, C. 1991, *The Physics of Solar Flares*. Proceedings of the Royal Society, UK
- Czaykowska, A., de Pontieu, B., Alexander, D., & Rank, G. 1999, *ApJ*, 521, L75
- Dalla, S., Fletcher, L., & Walton, N. A. 2008, *A&A*, 479, L1
- Davis, L. 1955, *Phys Rev*, 100, 1440
- De Pontieu, B., Erdélyi, R., & James, S. P. 2004, *Nature*, 430, 536
- Del Zanna, G. 1995, Master thesis, Univ. of Florence, Italy
- Del Zanna, G. 1999, PhD thesis, Univ. of Central Lancashire, UK
- Del Zanna, G. 2002, in *High Resolution X-ray Spectroscopy with XMM-Newton and Chandra*, ed. Branduardi-Raymont, G. (London: University College London, UK)
- Del Zanna, G. 2003, *A&A*, 406, L5
- Del Zanna, G. 2007, *ASPC*, Vol. 397, *First Science Results from Hinode*, 87
- Del Zanna, G. 2008, *A&A*, 481, L49
- Del Zanna, G., & Andretta, V. 2010, in *IAU Symposium*, Vol. 264, eds. A. G. Kosovichev, A. H. Andrei, & J.-P. Roelot, 78–80
- Del Zanna, G., Berlicki, A., Schmieder, B., & Mason, H. E. 2006a, in *10 Years of SOHO and Beyond*, *Sol Phys*, Vol. 617
- Del Zanna, G., Berrington, K. A., & Mason, H. E. 2004, *A&A*, 422, 731
- Del Zanna, G., & Bromage, B. J. I. 1999, *J Geophys Res*, 104, 9753
- Del Zanna, G., Bromage, B. J. I., & Mason, H. E. 2001, in *Solar and Galactic Composition*, *AIP Conf Proc* 598, 59
- Del Zanna, G., Bromage, B. J. I., & Mason, H. E. 2003, *A&A*, 398, 743
- Del Zanna, G., Gibson, S. E., Mason, H. E., Pike, C. D., & Mandrini, C. H. 2002a, *Adv Space Res*, 30, 551
- Del Zanna, G., Landini, M., & Mason, H. E. 2002b, *A&A*, 385, 968
- Del Zanna, G., & Mason, H. E. 2003, *A&A*, 406, 1089
- Del Zanna, G., Mason, H. E., & Cirtain, J. 2006b, in *10 Years of SOHO and Beyond*, *ESA Special Publication*, Vol. 617
- Del Zanna, G., Rozum, I., & Badnell, N. 2008, *A&A*, 487, 1203
- Dere, K. P., Bartoe, J., Brueckner, G. E., Cook, J. W., & Socker, D. G. 1987, *Sol Phys*, 114, 223
- Dere, K. P., Landi, E., Mason, H. E., Monsignori Fossi, B. C., & Young, P. R. 1997, *A&AS*, 125, 149
- Dere, K. P., & Mason, H. E. 1981, in *Solar Active Regions: A Monograph from Skylab Solar Workshop III*, eds. F. Q. Orrall, 129–164 (Boulder: Colorado Associated University Press)
- Dere, K. P., & Mason, H. E. 1993, *Sol Phys*, 144, 217
- Deubner, F. 1975, *A&A*, 44, 371
- Dore, U., & Orestano, D. 2008, *Rep Prog Phys*, 71, 106201
- Doschek, G. A. 1990, *ApJS*, 73, 117
- Doschek, G. A., et al. 2007, *ApJ*, 667, L109
- Dowdy, J. F., Jr., Rabin, D., & Moore, R. L. 1986, *Sol Phys*, 105, 35
- Drake, J. F. 1971, *Sol Phys*, 16, 152
- Drake, J. J., Laming, J. M., & Widing, K. G. 1997, *ApJ*, 478, 403
- Dzifčáková, E., Kulinová, A., Chifor, C., Mason, H. E., Del Zanna, G., Sylwester, J., & Sylwester, B. 2008, *A&A*, 488, 311
- Eddy, J. A. 1976, *Science*, 192, 1189
- Edlén, B. 1942, *Zeitschrift für Astrophysics*, 22, 30
- Erdélyi, R., & Ballai, I. 2007, *Astronomische Nachrichten*, 328, 726
- Feldman, U. 1983, *ApJ*, 275, 367
- Feldman, U., Schühle, U., Widing, K. G., & Laming, J. M. 1998, *ApJ*, 505, 999
- Fisk, L. A., & Schwadron, N. A. 2001, *ApJ*, 560, 425
- Fletcher, L., & Hudson, H. S. 2008, *ApJ*, 675, 1645
- Fludra, A., & Schmelz, J. T. 1995, *ApJ*, 447, 936
- Fludra, A., & Schmelz, J. T. 1999, *A&A*, 348, 286
- Forbes, T. G., & Priest, E. R. 1995, *ApJ*, 446, 377
- Foukal, P. V. 2004, *Solar Astrophysics*, 2nd, Revised Edition (Wiley-VCH Verlag GmbH)
- Fröhlich, C. 2009, *A&A*, 501, L27
- Fröhlich, C., & Lean, J. 2004, *A&A Rev.*, 12, 273
- Fuhrmann, K. 2008, *MNRAS*, 384, 173
- Gabriel, A. H. 1976, *Philos Trans R Soc Lond A*, 281, 339
- Gabriel, A. H., Culhane, J. L., Patchett, B. E., Breeveld, E. R., Lang, J., Parkinson, J. H., Payne, J., & Norman, K. 1995, *Adv Space Res*, 15, 63
- Gabriel, A. H., & Jordan, C. 1969, *MNRAS*, 145, 241
- Gabriel, A. H., & Mason, H. E. 1982, in *Applied Atomic Collision Physics, Atmospheric Physics and Chemistry*, Vol. 1, eds. H. S. W. Massey, & D. R. Bates (New York: Academic Press), 45–397
- Geiss, J. 1982, *Space Sci Rev*, 33, 201
- Geiss, J., & Buergi, A. 1986, *A&A*, 159, 1
- Gizon, L., & Birch, A. C. 2005, *Living Reviews in Solar Physics*, 2, 6
- Gloeckler, G., & Geiss, J. 2007, *Space Sci Rev*, 130, 139
- Goldschmidt, V. 1938, *Skrifter Norske Videnskaps-Akad., Oslo I Math.-Naturv. Klasse*, 4, 148

- Golub, L., & Pasachoff, J. M. 2010, *The Solar Corona* (Cambridge: Cambridge University Press)
- Gough, D., & Toomre, J. 1991, *ARA&A*, 29, 627
- Güdel, M., Audard, M., Reale, F., Skinner, S. L., & Linsky, J. L. 2004, *A&A*, 416, 713
- Güdel, M., & Nazé, Y. 2009, *A&A Rev.*, 17, 309
- Haigh, J. D. 1996, *Science*, 272, 981
- Haigh, J. D. 2007, *Living Reviews in Solar Physics*, 4, 2
- Hassler, D. M., Dammasch, I. E., Lemaire, P., Brekke, P., Curdt, W., Mason, H. E., Vial, J., & Wilhelm, K. 1999, *Science*, 283, 810
- Hirayama, T. 1974, *Sol Phys*, 34, 323
- Hollweg, J. V. 2008, *Astron Astrophys*, 29, 217
- Hou, J. L., Prantzos, N., & Boissier, S. 2000, *A&A*, 362, 921
- Hoyt, D. V., & Schatten, K. H. 1998, *Sol Phys*, 179, 189
- Hughes, D. W., Rosner, R., & Weiss, N. O., eds. 2007, *The Solar Tachocline* (Cambridge: Cambridge Univ. Press)
- Hummer, D. G., Berrington, K. A., Eissner, W., Pradhan, A. K., Saraph, H. E., & Tully, J. A. 1993, *A&A*, 279, 298
- Hundhausen, A. J., Sawyer, C. B., House, L., Illing, R. M. E., & Wagner, W. J. 1984, *J Geophys Res*, 89, 2639
- Jain, R., Hindman, B. W., Braun, D. C., & Birch, A. C. 2009, *ApJ*, 695, 325
- Jones, P. D., Briffa, K., Barnett, T., & Tett, S. 1998, *The Holocene*, 8, 455
- Jones, P. D., & Moberg, A. 2003, *J Climate*, 16, 206
- Jordan, C., Smith, G. R., & Houdebine, E. R. 2005, *MNRAS*, 362, 411
- Jordan, S. 1981, in *The Sun as a star*, ed. S. Jordan, Vol. 450 (NASA Special Publication)
- Judge, P. 2006, in *Solar MHD Theory and Observations: A High Spatial Resolution Perspective*, eds. H. Uitenbroek, J. Leibacher, & R. F. Stein, 354, 259 (Astronomical Society of the Pacific Conference Series)
- Judge, P. G. 2000, *ApJ*, 531, 585
- Kane, S. R., Frost, K. J., & Donnelly, R. F. 1979, *ApJ*, 234, 669
- Karzas, W. J., & Latter, R. 1961, *ApJS*, 6, 167
- Kjeldseth Moe, O., & Nicolas, K. R. 1977, *ApJ*, 211, 579
- Kliem, B., Titov, V. S., & Török, T. 2004, *A&A*, 413, L23
- Kliem, B., & Török, T. 2006, *Phys Rev Lett*, 96, 255002
- Klimchuk, J. A. 2006, *Sol Phys*, 234, 41
- Kohl, J. L., Noci, G., Cranmer, S. R., & Raymond, J. C. 2006, *A&A Rev.*, 13, 31
- Krieger, A. S., Timothy, A. F., & Roelof, E. C. 1973, *Sol Phys*, 29, 505
- Krivova, N. A., Balmaceda, L., & Solanki, S. K. 2007, *A&A*, 467, 335
- Kunow, H., Crooker, N. U., Linker, J. A., Schwenn, R., & von Steiger, R. 2006, *Space Sci Rev*, 123, 1
- Laming, J. M. 2004, *ApJ*, 614, 1063
- Landi, E., Mason, H. E., Lemaire, P., & Landini, M. 2000, *A&A*, 357, 743
- Landini, M., & Monsignori Fossi, B. C. 1975, *A&A*, 42, 213
- Leibacher, J. W., & Stein, R. F. 1981, in *The Sun as a star*, ed. Jordan, S., Vol. 450 (NASA Special Publication), 263
- Leighton, R. B. 1964, *ApJ*, 140, 1547
- Leighton, R. B. 1969, *ApJ*, 156, 1
- Leighton, R. B., Noyes, R. W., & Simon, G. W. 1962, *ApJ*, 135, 474
- Lin, R. P., Schwartz, R. A., Kane, S. R., Pelling, R. M., & Hurley, K. C. 1984, *ApJ*, 283, 421
- Livingston, W., Wallace, L., White, O. R., & Giampapa, M. S. 2007, *ApJ*, 657, 1137
- Lodders, K., Palme, H., & Gail, H. 2009, *ArXiv e-prints*
- Low, B. C. 2001, *J Geophys Res*, 106, 25141
- Lytot, B. 1939, *MNRAS*, 99, 580
- Mariska, J. T. 1992, *The Solar Transition Region* (Cambridge: Cambridge University Press)
- Marsch, E. 2006, *Living Reviews in Solar Physics*, 3
- Martens, P. C. H., Kankelborg, C. C., & Berger, T. E. 2000, *ApJ*, 537, 471
- Mason, H. E. 1995, *Adv Space Res*, 15, 53
- Mason, H. E., Landi, E., Pike, C. D., & Young, P. R. 1999, *Sol Phys*, 189, 129
- Mason, H. E., & Monsignori Fossi, B. C. M. 1994, *A&A Rev.*, 6, 123
- Mason, H. E., Shine, R. A., Gurman, J. B., & Harrison, R. A. 1986, *ApJ*, 309, 435
- Maunder, A. S. D. 1907, *MNRAS*, 67, 451
- Maunder, E. W. 1904, *MNRAS*, 64, 747
- McComas, D. J., Ebert, R. W., Elliott, H. A., Goldstein, B. E., Gosling, J. T., Schwadron, N. A., & Skoug, R. M. 2008, *Geophys Res Lett*, 35, 18103
- Meier, R. R. 1991, *Space Sci. Rev.*, 58, 1
- Mestel, L. 1999, *Stellar Magnetism* (Oxford: Oxford University Press)
- Meyer, J. 1985, *ApJS*, 57, 173
- Miesch, M. S. 2005, *Living Reviews in Solar Physics*, 2
- Moore, R. L., & Sterling, A. C. 2006, *Washington DC American Geophysical Union Geophysical Monograph Series*, 165, 43
- Narain, U., & Ulmschneider, P. 1996, *Space Sci Rev*, 75, 453
- Nordlund, Å., Stein, R. F., & Asplund, M. 2009, *Living Reviews in Solar Physics*, 6, 2
- O' Dwyer, B., Del Zanna, G., Mason, H. E., Sterling, A., Tripathi, D., & Young, P. 2010, *A&A*, 525, A137
- Orrall, F. Q., ed. 1981, *Solar Active Regions: A Monograph from SKYLAB Solar Workshop III* (Boulder: Colorado Associated University Press)

- Parenti, S., Buchlin, E., Cargill, P. J., Galtier, S., & Vial, J. 2006, *ApJ*, 651, 1219
- Parker, E. N. 1958, *ApJ*, 128, 664
- Parker, E. N. 1988, *ApJ*, 330, 474
- Parnell, C. E., & Jupp, P. E. 2000, *ApJ*, 529, 554
- Peter, H., & Judge, P. G. 1999, *ApJ*, 522, 1148
- Pevtsov, A. A., Fisher, G. H., Acton, L. W., Longcope, D. W., Johns-Krull, C. M., Kankelborg, C. C., & Metcalf, T. R. 2003, *ApJ*, 598, 1387
- Phillips, K. J. H. 1992, *Guide to the sun* (Cambridge: Cambridge University Press)
- Phillips, K. J. H., Feldman, U., & Landi, E. 2008, *Ultraviolet and X-ray Spectroscopy of the Solar Atmosphere* (Cambridge: Cambridge University Press)
- Phillips, K. J. H., Pike, C. D., Lang, J., Zarro, D. M., Fludra, A., Watanabe, T., & Takahashi, M. 1995, *Adv Space Res*, 15, 33
- Pikel'Ner, S. B. 1969, *Soviet Astronomy*, 13, 259
- Pneuman, G. W., & Kopp, R. A. 1978, *Sol Phys*, 57, 49
- Pottasch, S. R. 1963, *ApJ*, 137, 945
- Pottasch, S. R. 1967, *Bull. Astron. Inst. Netherlands*, 19, 113
- Priest, E., & Forbes, T. 2000, *Magnetic Reconnection: MHD theory and applications* (Cambridge: Cambridge University Press)
- Priest, E. R. 1982, *Solar Magnetohydrodynamics* (Dordrecht: D.Reidel)
- Priest, E. R., Foley, C. R., Heyvaerts, J., Arber, T. D., Culhane, J. L., & Acton, L. W. 1998, *Nature*, 393, 545
- Priest, E. R., & Forbes, T. G. 2002, *A&A Rev.*, 10, 313
- Ramaty, R., & Murphy, R. J. 1987, *Space Sci Rev*, 45, 213
- Raymond, J. C., et al. 1997, *Sol Phys*, 175, 645
- Reames, D. V. 1999, *Space Sci Rev*, 90, 413
- Reeves, E. M. 1976, *Sol Phys*, 46, 53
- Roberts, B. 1979, *Sol Phys*, 61, 23
- Rosner, R., Tucker, W. H., & Vaiana, G. S. 1978, *ApJ*, 220, 643
- Russell, H. N. 1929, *ApJ*, 70, 11
- Rust, D. M. 1976, *Sol Phys*, 47, 21
- Rutten, R. J. 2007, in *Astronomical Society of the Pacific Conference Series*, Vol. 368, *The Physics of Chromospheric Plasmas*, eds. P. Heinzel, I. Dorotović, & R. J. Rutten, 27
- Schwenn, R., & Marsch, E. 1990, *Physics of the Inner Heliosphere I. Large-Scale Phenomena* (Berlin: Springer)
- Schwenn, R., & Marsch, E. 1991, *Physics of the Inner Heliosphere II. Particles, Waves and Turbulence* (Berlin: Springer)
- Seaton, M. J. 1964a, *MNRAS*, 127, 191
- Seaton, M. J. 1964b, *Planet. Space Sci.*, 12, 55
- Serenelli, A. M., Basu, S., Ferguson, J. W., & Asplund, M. 2009, *ApJ*, 705, L123
- Solanki, S. K., Inhester, B., & Schüssler, M. 2006, *Rep Prog Phys*, 69, 563
- Solanki, S. K., Schüssler, M., & Fligge, M. 2002, *A&A*, 383, 706
- Spitzer, L. 1965, *Physics of Fully Ionized Gases* (New York: Interscience Publishers, Inc.)
- Stein, R. F., & Leibacher, J. 1974, *ARA&A*, 12, 407
- Stenflo, J.O., 1989, *A&AR* 1, 3-48
- Stix, M. 2002, *The Sun: An Introduction* (Berlin: Springer)
- Strong, K. 1978, PhD thesis, University College London, UK
- Sturrock, P. A., eds. 1980, *Solar Flares: A Monograph from SKYLAB Solar Workshop II* (Boulder: Colorado Associated University Press)
- Sturrock, P. A., & Hartle, R. E. 1966, *Phys Rev Lett*, 16, 628
- Suematsu, Y. 1990, in *Lecture Notes in Physics, Progress of Seismology of the Sun and Stars*, Vol. 367, eds. Y. Osaki & H. Shibahashi (Berlin: Springer Verlag), 211
- Thomas, J. H., & Weiss, N. O. 2008, *Sunspots and Starspots* (Cambridge: Cambridge University Press)
- Thompson, M. J., Christensen-Dalsgaard, J., Miesch, M. S., & Toomre, J. 2003, *ARA&A*, 41, 599
- Tobias, S. 2004, in *Fluid Dynamics and Dynamos in Astrophysics and Geophysics*, eds. A. Soward, C. Jones, D. Hughes, & N. Weiss (Oxford, UK: Taylor & Francis Group), 193
- Tobias, S., & Weiss, N. 2007, in *The Solar Tachocline*, eds. D. W. Hughes, R. Rosner, & N. O. Weiss (Cambridge: Cambridge Univ. Press), 319
- Tripathi, D., Mason, H. E., Dwivedi, B. N., del Zanna, G., & Young, P. R. 2009, *ApJ*, 694, 1256
- Tziotziou, K., Tsiropoula, G., & Mein, P. 2003, *A&A*, 402, 361
- Ulrich, R. K. 1970, *ApJ*, 162, 993
- Veck, N. J., & Parkinson, J. H. 1981, *MNRAS*, 197, 41
- Veck, N. J., Strong, K. T., Jordan, C., Simnett, G. M., Cargill, P. J., & Priest, E. R. 1984, *MNRAS*, 210, 443
- Velli, M. 1994, *ApJ*, 432, L55
- von Steiger, R., & Geiss, J. 1989, *A&A*, 225, 222
- von Steiger, R., et al. 2000, *J Geophys Res*, 105, 27217
- Walker, A. B. C., Jr., Ruge, H. R., & Weiss, K. 1974, *ApJ*, 188, 423
- Weiss, N. 1994, in *Lectures on Solar and Planetary Dynamos*, eds. M. Proctor & A. Gilbert (Cambridge, UK; New York, USA: Cambridge University Press), 59
- Weiss, N. O., & Thompson, M. J. 2009, *Space Sci Rev*, 144, 53
- Widing, K. G., & Feldman, U. 1989, *ApJ*, 344, 1046
- Widing, K. G., & Feldman, U. 2001, *ApJ*, 555, 426

- Wimmer-Schweingruber, R. F., eds. 2001, in American Institute of Physics Conference Series, Vol. 598, Joint SoHO/ACE Workshop "Solar and Galactic Composition" (New York: American Institute of Physics)
- Withbroe, G. L. 1978, *ApJ*, 225, 641
- Wood, B. E. 2004, *Living Reviews in Solar Physics*, 1, 2
- Woods, T. N., Tobiska, W. K., Rottman, G. J., & Worden, J. R. 2000, *J Geophys Res*, 105, 27195
- Woods, T. N., et al. 2009, *Geophys Res Lett*, 36, 1101
- Young, C. 1870, *J. Franklin Inst*, 60, 232
- Young, P. R., & Mason, H. E. 1997, *Sol Phys*, 175, 523
- Young, P. R., et al. 2007, *PASJ*, 59, 857
- Zank, G. P. 1999, *Space Sci Rev*, 89, 413
- Zhitnik, I. A., et al. 2003, *MNRAS*, 338, 67
- Zirin, H. 1988, *Astrophysics of the Sun* (Cambridge: Cambridge University Press)
- Zirker, J. B., ed. 1977, *Coronal holes and high speed wind streams: a monograph from Skylab solar workshop I* (Boulder: Colorado Associated University Press)
- Zurbuchen, T. H. 2007, *ARA&A*, 45, 297